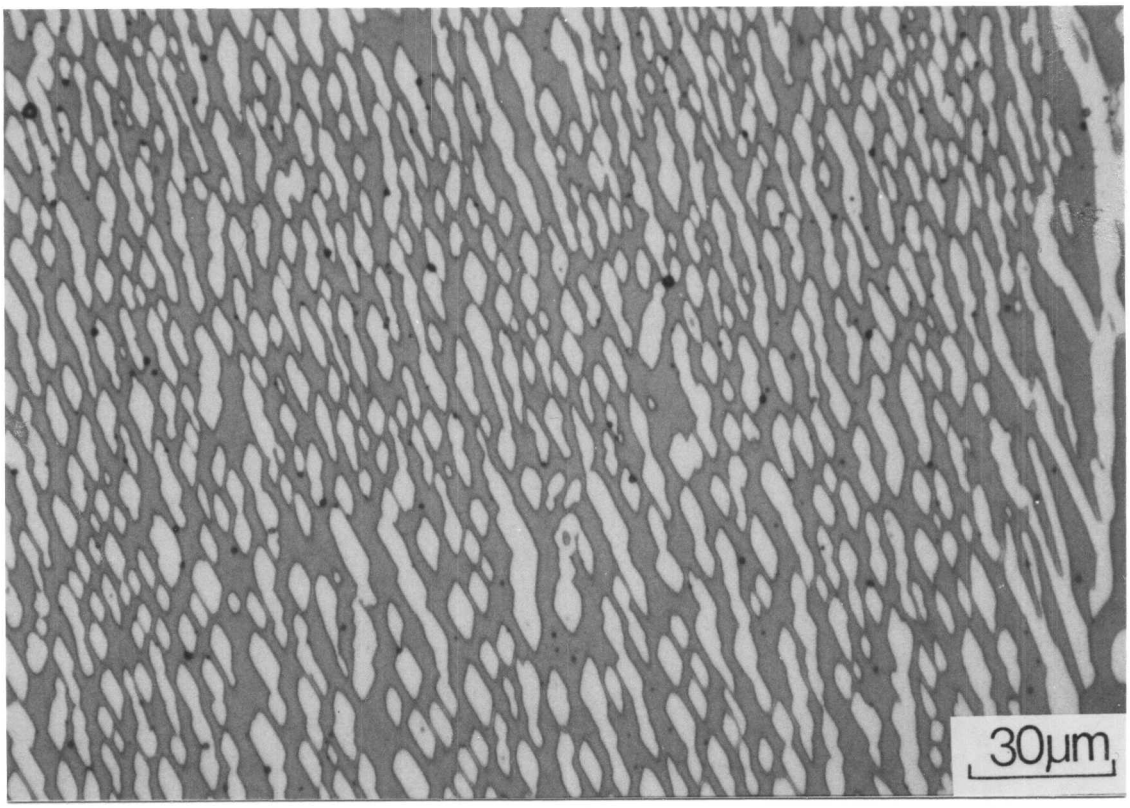

Fig. 6.9: Optical micrograph showing the microstructure of alloy BW after direct isothermal transformation from T_δ at 1100°C. The light etching phase is austenite.

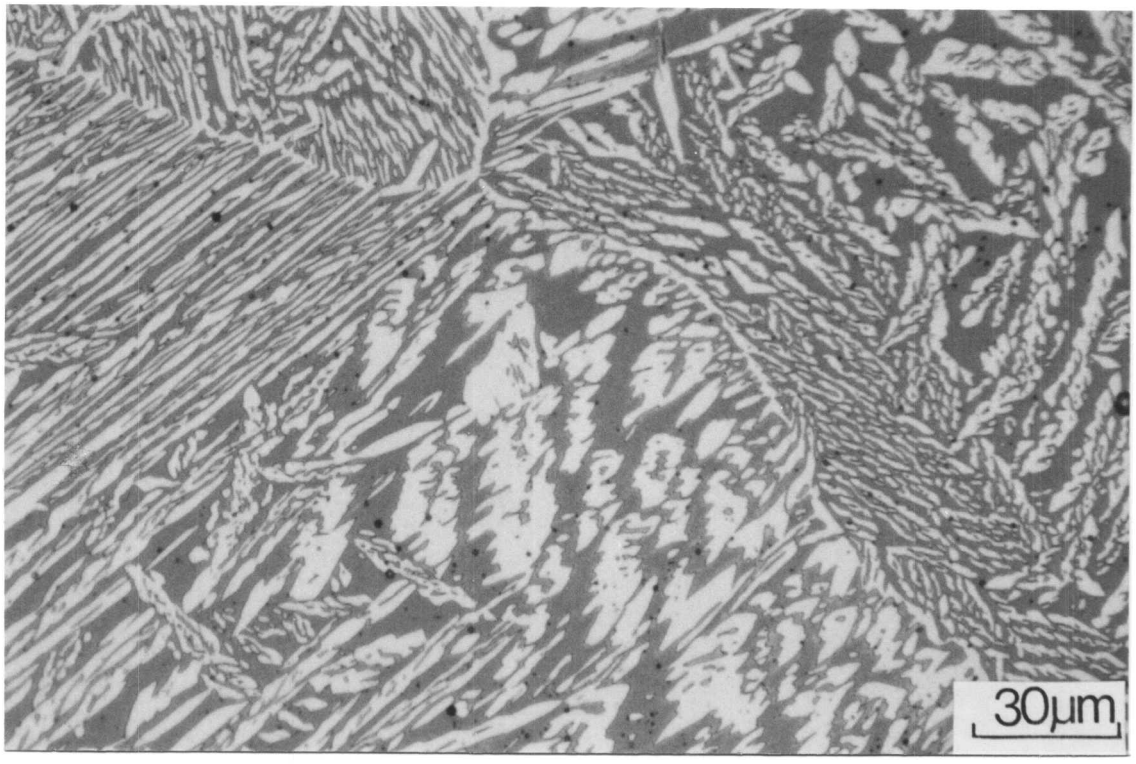

Fig. 6.10: Optical micrograph showing the microstructure of alloy BW after direct isothermal transformation from T_δ at 1000°C. The light etching phase is austenite.

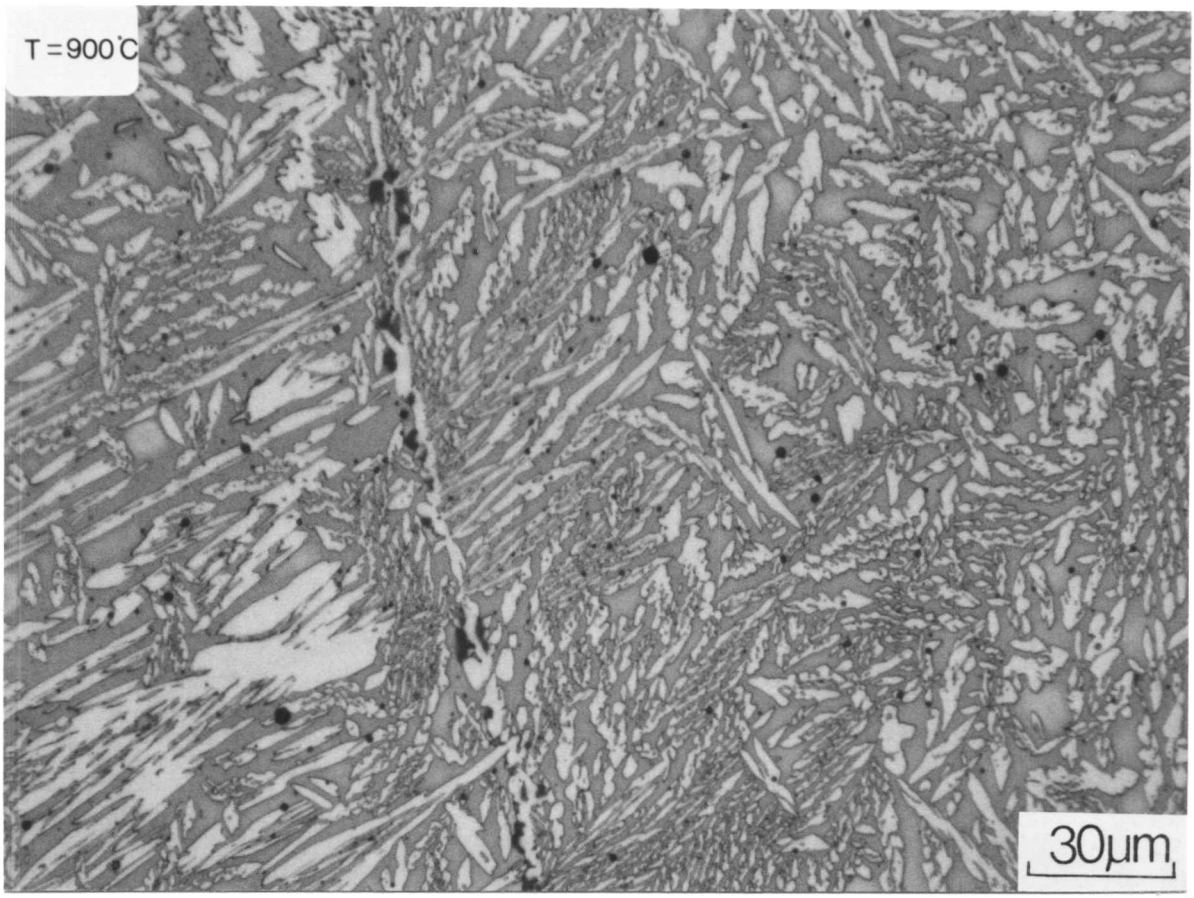

Fig. 6.11: Optical micrograph showing the microstructure of a sample of alloy BW after direct isothermal transformation from the T_δ at 900°C. The light etching phase is austenite. δ-ferrite is brown and the dark etching phase at the original δ/δ boundaries is σ phase.

Fig. 6.12: Optical micrograph showing the microstructure of a sample of welded alloy BW, after direct isothermal transformation at 800°C. The light etching phase is austenite. δ-ferrite is brown and the dark etching phase at the δ/γ boundaries is σ phase.

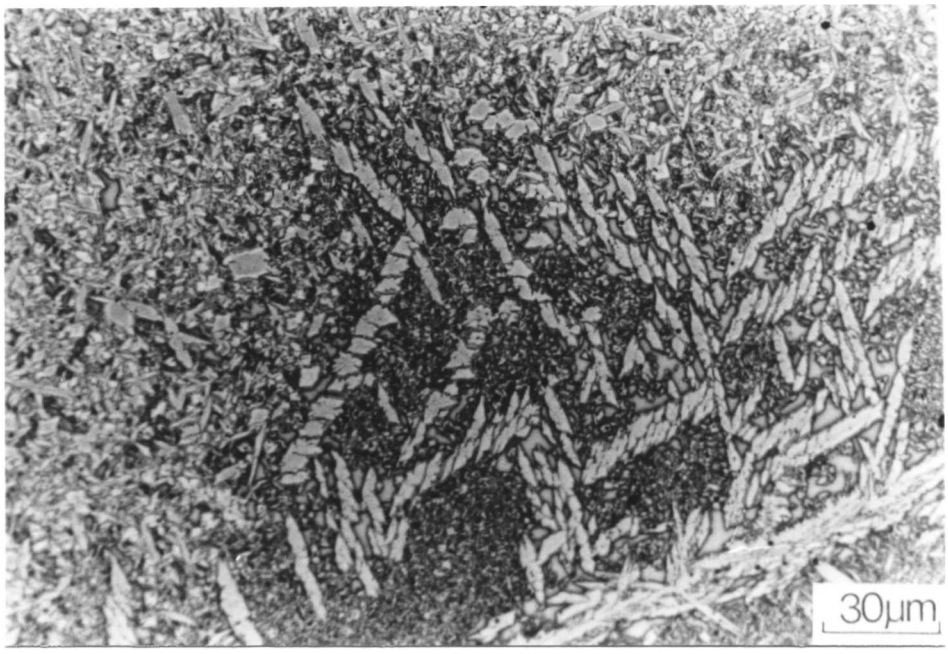

Fig. 6.13: Optical micrograph showing the microstructure of a sample of welded alloy BW, after direct isothermal treatment from T_δ at 700°C. The light etching phase is austenite. Apart from the allotriomorphic austenite, the micrograph clearly display the two distinctive morphologies of austenite; Widmanstätten austenite (and their parallelpiped cross sections, large) and the fine "acicular" austenite.

with the sample treated at 800°C could be a result of $\delta \rightarrow \gamma$ transformation occurring during the quench from T_δ to 700°C.

The essential features of the microstructures obtained for the isothermally transformed BW specimens which were solution annealed prior to the isothermal treatment were the same as those associated with the as-received welded condition. Although there is a general tendency towards slightly lower austenite volume fractions, no significant difference was observed between the volume fraction of austenite obtained after isothermal transformation for 1000 seconds compared with the isothermally transformed as-received BW specimens. This indicates that the solution treatment carried out above the ferritisation temperature prior to the isothermal transformation treatment, eliminated the effect of the solution annealing in the two phase region *i.e.* the homogenisation kinetics above T_δ were fast (<5 minutes).

6.2.3 Isothermal Transformation Diagrams for Alloy WR4

The isothermal transformation curves of volume fraction of austenite versus time for the isothermal transformation temperatures 1100, 1000, 900, and 800°C are shown in Fig. 6.14. The curves are very similar to those of alloy BW with somewhat faster kinetics and higher maximum volume fractions of austenite for 1200 seconds of reaction. This could be attributed to the higher oxygen content in WR4 specimens.

6.2.4 Metallography of Isothermally Transformed alloy WR4

At 1100°C the $\delta \rightarrow \gamma$ transformation products were found to be essentially the same as those obtained for sample BW at the same isothermal transformation temperature Fig.6.15. Consistent with the higher oxygen content of WR4, the volume fraction of austenite was somewhat higher and in addition, the transformation was found to terminate after 90 seconds when compared with 130 seconds for BW.

Isothermal transformation at 1000°C led, as expected, to a higher volume fraction of austenite when compared with that obtained on transformation at 1100°C.

At 900°C the dominant product of the $\delta \rightarrow \gamma$ transformation was the γ_{intra} with a finer morphology when compared with the irregular morphologies observed due to transformation at higher temperatures. σ phase formation was observed at the original δ/δ boundary sites and also at the δ/γ interfaces. The maximum volume fraction of austenite after 1200 seconds was less than that obtained at 1000°C. The dominance of the intragranular morphology could be a consequence of the large grain size of the δ-ferrite or possibly to a shift in the nose of the C-curve to somewhat higher temperatures than 900°C Fig. 6.16. A larger δ grain size provide less nucleation sites for the Widmanstätten austenite, by providing less surface area per unit volume. The two stages of reaction evident from the isothermal transformation curve at 800°C, were well separated in time, and the microstructures revealed were the same as those observed for the BW sample at the same isothermal temperature Fig. 6.17.

The results obtained for the previously solution treated WR4 specimens were similar to those obtained for BW, Fig. 6.18. Due to the coarse δ grains the dominant morphology was the intragranular austenite.

It should also be noted that the isothermally transformed specimens have generally retained some of their common columnar appearance. The columnar grains were observed to be larger when compared to the as-welded condition. This may be due to the coarse initial grain structure and to the geometry and size of the specimen,

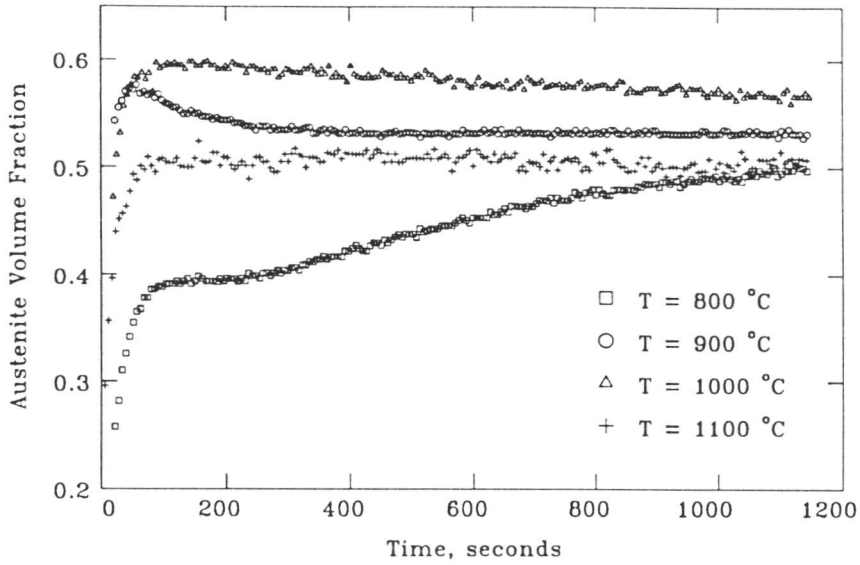

a

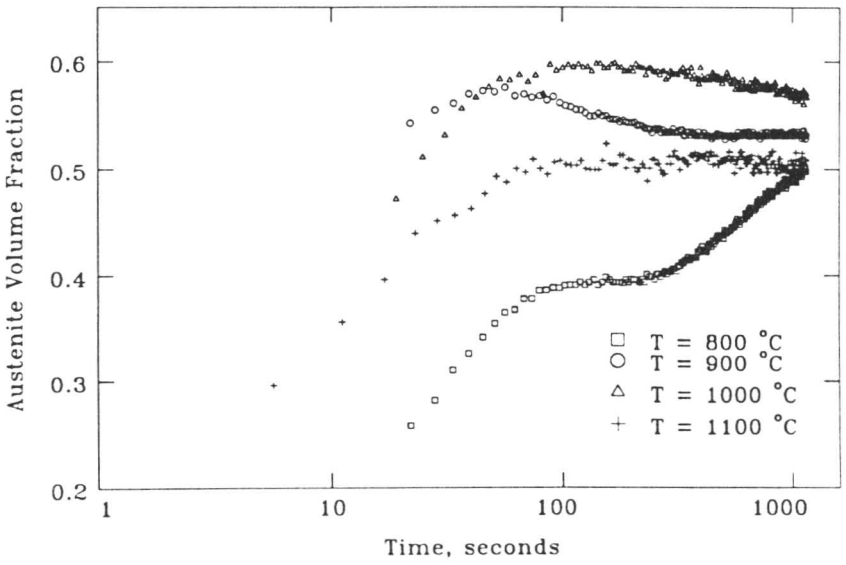

b

Fig. 6.14: Isothermal transformation diagrams of the volume fraction of austenite as calculated from dilatometric data, versus the $\delta \rightarrow \gamma$ reaction time, for samples of welded alloy WR4 which were isothermally transformed directly from the ferritisation temperature:

a) reaction time, linear scale; b) reaction time, log scale.

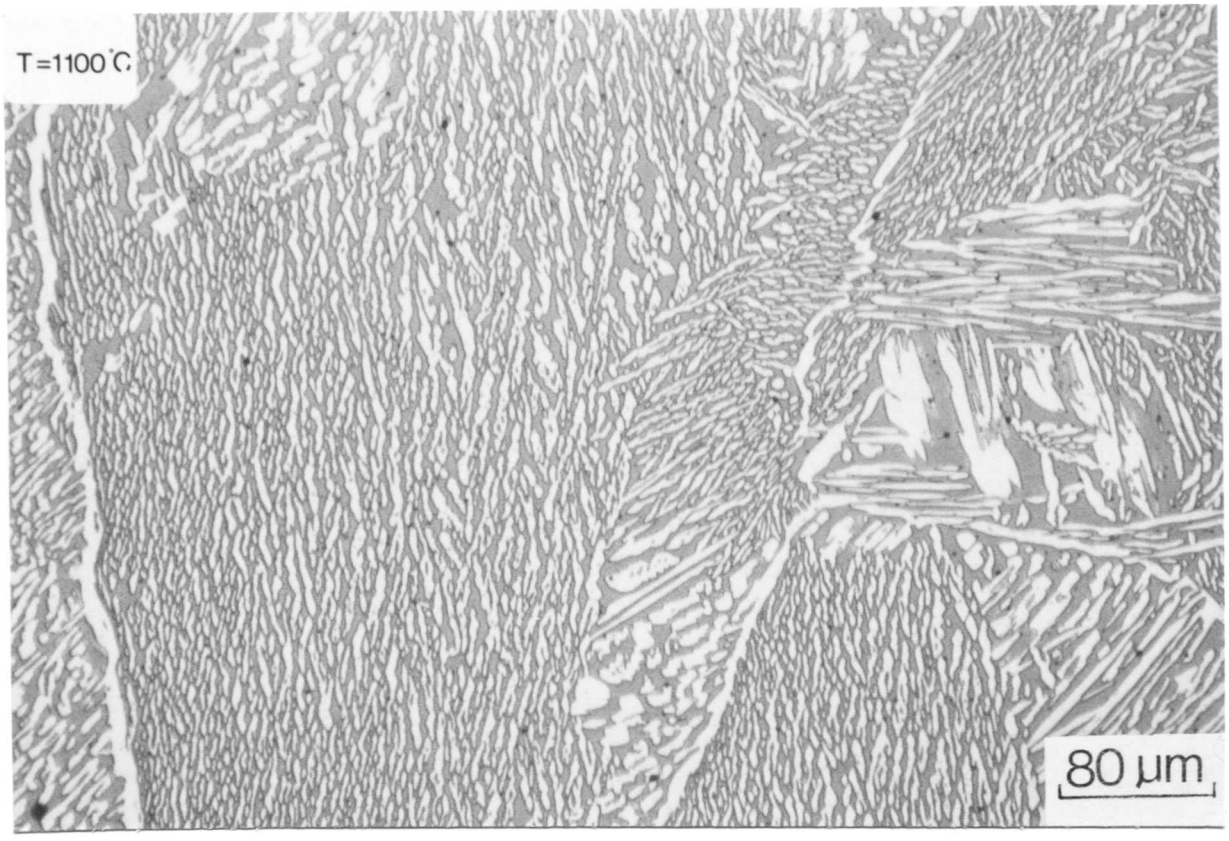

Fig. 6.15: Optical micrograph showing the microstructure of a sample of welded alloy WR4 after isothermal treatment at 1100°C for 1200 seconds. The specimen was ferritised from the as-received weld condition at 1350°C for 5 minutes. The light etching phase is austenite.

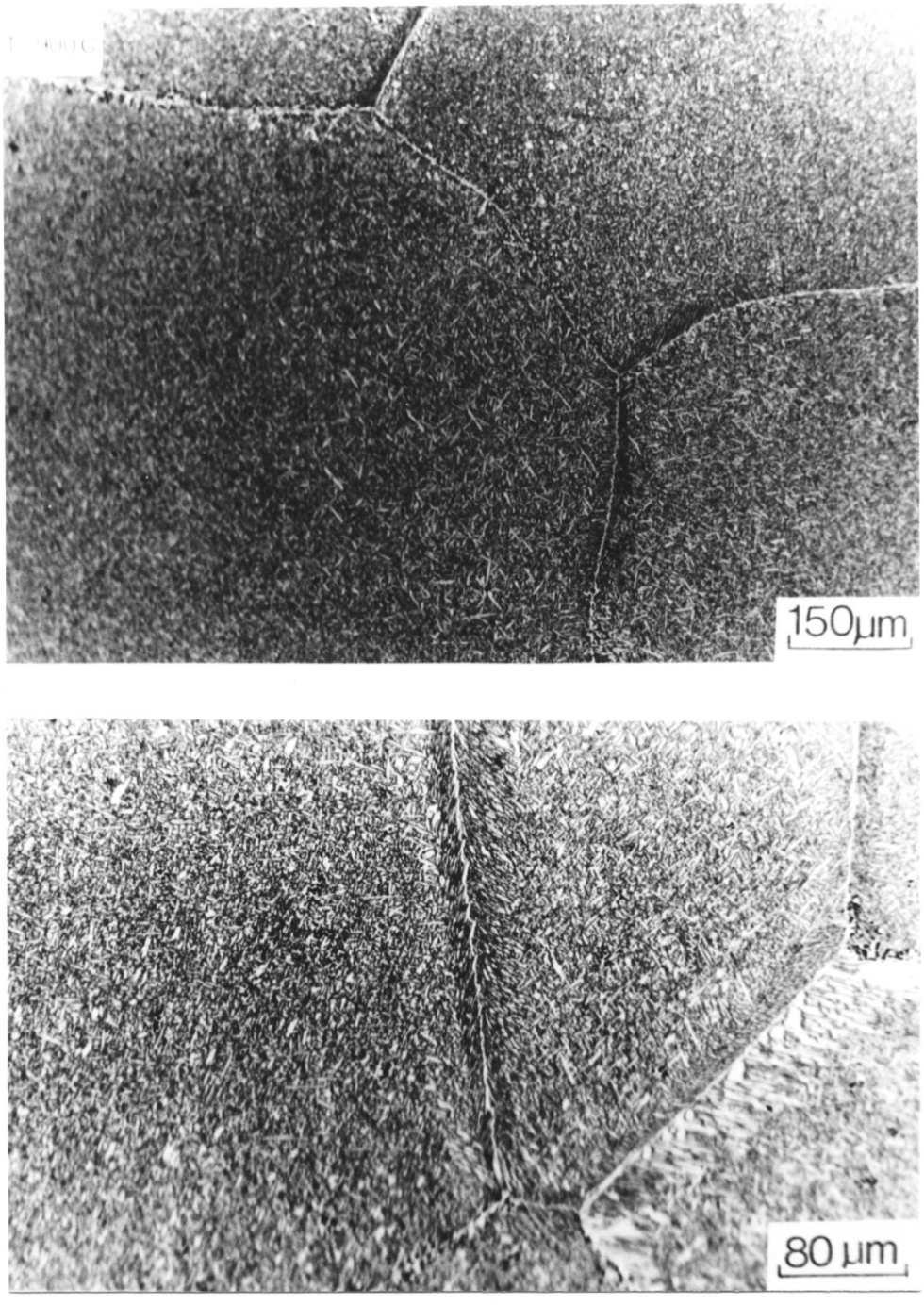

Fig. 6.16: Optical micrograph showing the microstructure of a sample of welded alloy WR4 after isothermal treatment at 900°C for 1200 seconds. The specimen was ferritised from the as-received weld condition at 1350°C for 5 minutes. The light etching phase is austenite. The dark etching phase observed at the original δ-ferrite boundary sites is σ phase.

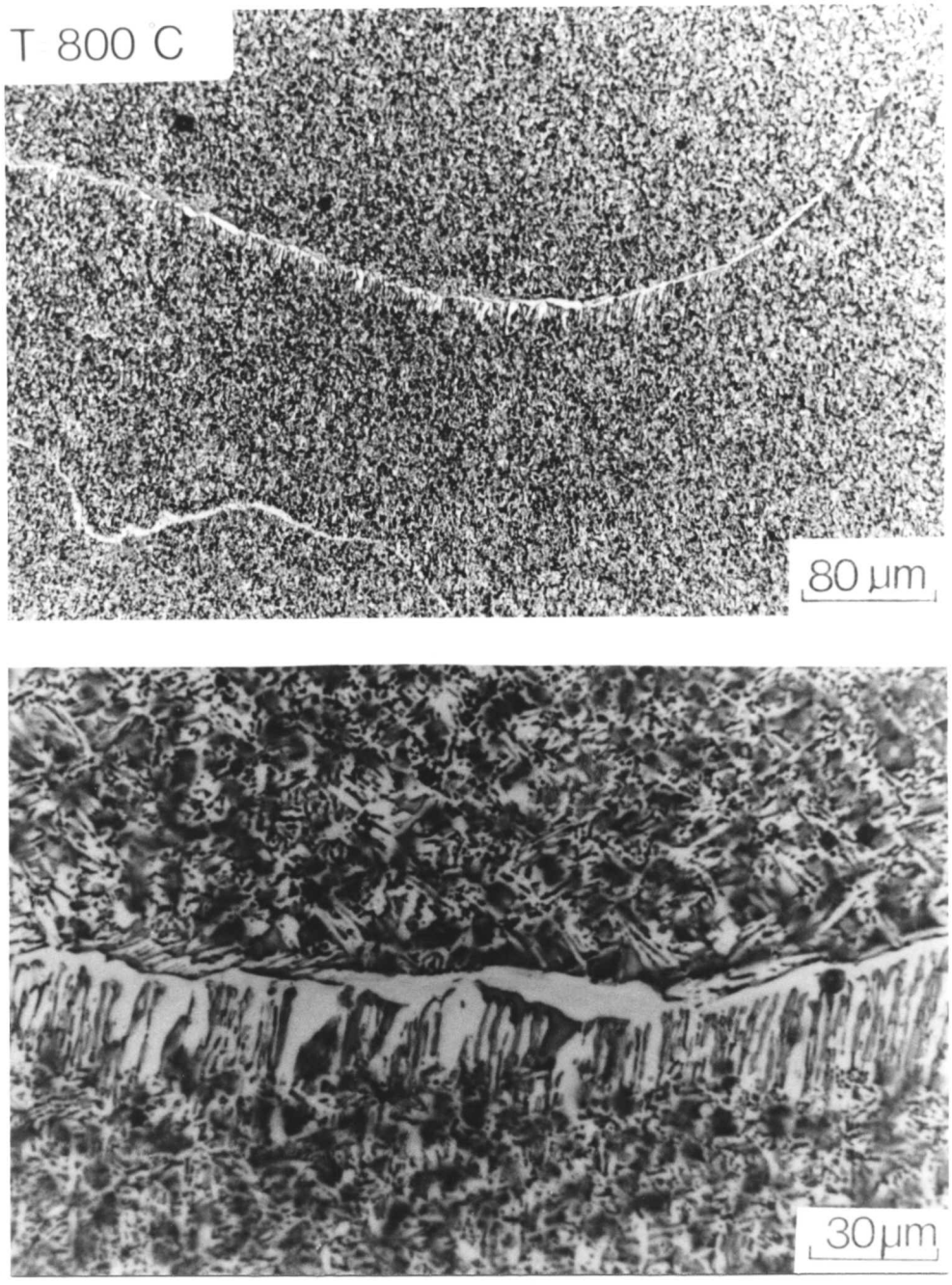

Fig. 6.17: Optical micrograph showing the microstructure of a sample of welded alloy WR4 after isothermal treatment at 800°C for 1200 seconds. The specimen was ferritised from the as-received weld condition, at 1350°C for 5 minutes. The light etching phase is austenite.

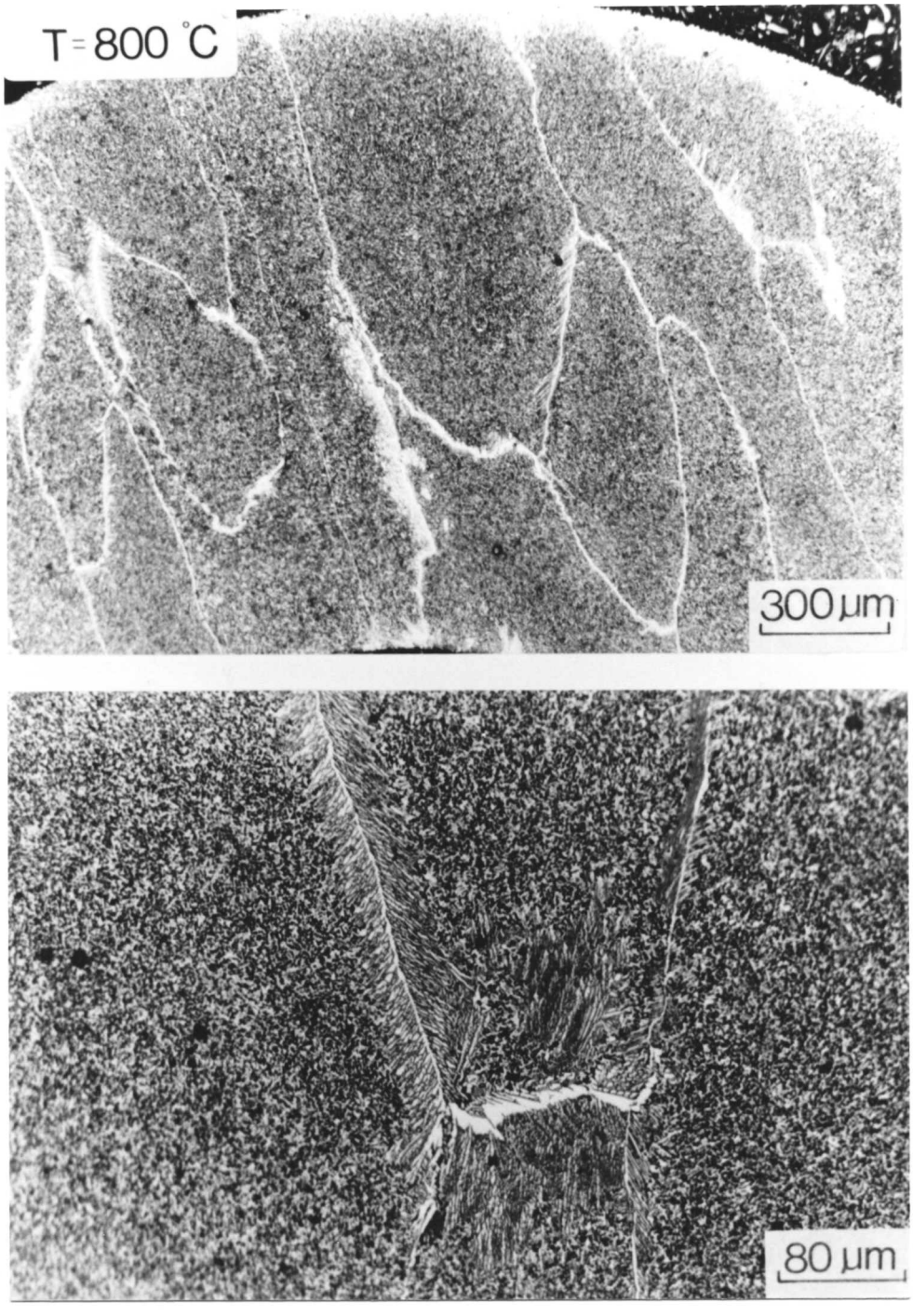

Fig. 6.18: Optical micrograph showing the microstructure of a sample of welded alloy WR4 after isothermal treatment at 800°C for 1200 seconds. Prior to the isothermal treatment, the specimen was solution treated at 1150°C for 48 hours. (T_δ = 1350°C, ferritisation time = 5 mins). The light etching phase is austenite.

exerting a limiting size effect on grain growth of the columnar δ-ferrite grains in the longitudinal direction Fig. 6.18.

6.2.5 Isothermal Transformation of Alloy SH

Specimens were heated for 5 minutes at 1300°C to obtain a fully ferritic microstructure and were brought down to the required transformation temperature using the Theta Industries high-speed dilatometer as described in (chapter 4). Isothermal transformation of δ was studied for coarse and relatively fine grained δ-ferrite structures within the range 1100 to 800°C. The volume fraction of austenite was estimated by a point count method and was double checked using a linear intercept method. The results are shown in Table 6.1.

Transformation at 1100°C

At this temperature the transformation to γ started with the formation of allotriomorphic austenite on the δ/δ grain boundaries followed by the nucleation and growth of Widmanstätten austenite from the austenite allotriomorphs. A few intragranularly nucleated austenite particles with a rod morphology were also observed. The allotriomorphic layers were not continuous along the δ-ferrite grain boundaries. Some of the grain boundaries were entirely free of austenite precipitation, Fig. 6.19.

Transformation at 1000°C and 900°C

At 1000°C isothermal transformation temperature, thin layers of austenite were found to cover most of the δ grain boundaries. Widmanstätten austenite growing from the austenite allotriomorphs was also observed, but the main phase was intragranularly nucleated austenite with a morphology scattered between rod and irregular shapes, as illustrated in Fig. 6.19. The features of the $\delta \rightarrow \gamma$ transformation were the same at 900°C as at 1000°C, with a faster rate of formation and a higher volume fraction of austenite, as illustrated in Fig. 6.19.

Transformation at 800°C

At this transformation temperature the allotriomorphic austenite at the δ grain boundaries was somewhat thicker for the same time period (300 sec) of transformation when compared with the experiments at 900 and 1000°C. The Widmanstätten arrays were not observed although there was heavy precipitation of intragranular austenite but of a finer morphology, Fig. 6.19.

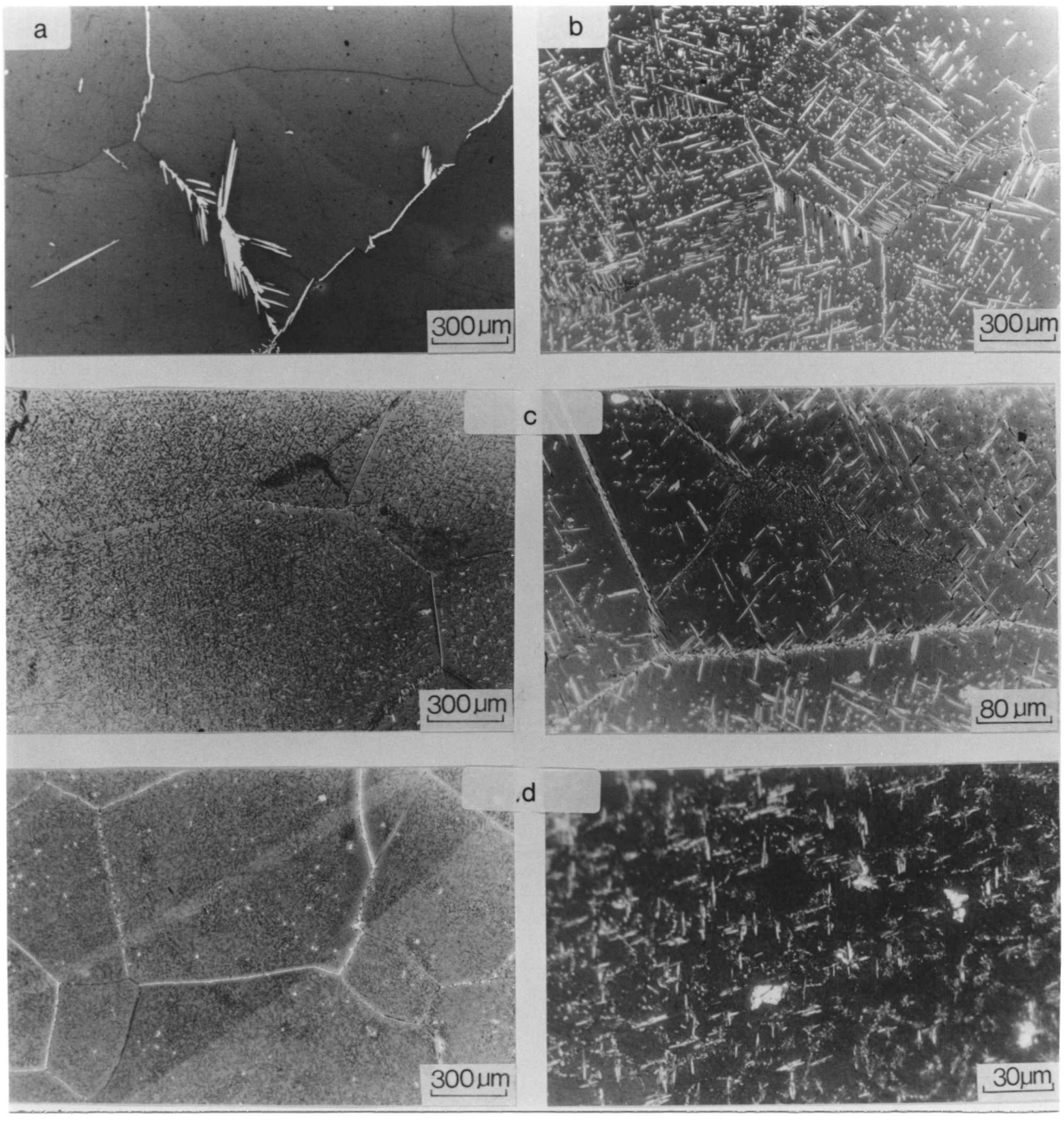

Fig. 6.19 a: A set of optical micrograph showing the microstructure of samples of wrought SH (200 μm D^*_δ) after isothermal treatments for 5 minutes at: (a) 1100, (b) 1000, (c) 900 and (d) 800°C (D^*_δ = primary δ average grain size). T_δ = 1300°C, ferritisation time = 5 mins. The light etching phase is austenite.

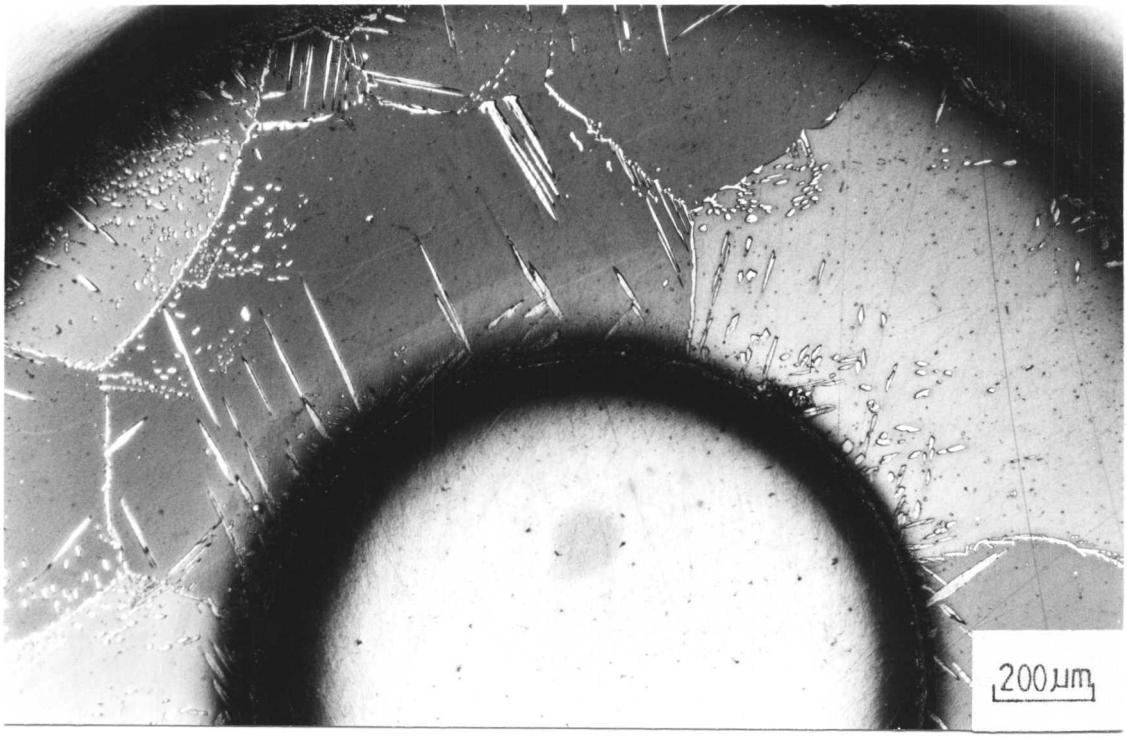

Fig. 6.19 b: Optical micrograph showing the microstructure of a sample of wrought alloy SH (600 μm D^*_δ) after isothermal transformation treatment for 60 mins at 1000°C.

For the coarse ♣ grained primary δ-ferrite specimens, heat treated at the same isothermal temperatures but for even longer times, the measured volume fractions of austenite after cooling to the ambient temperature were smaller (Table 6.1) and the features of transformation were somewhat different.

At 1100°C the $\delta \rightarrow \gamma$ transformation was limited, with very thin discontinuous austenite allotriomorphs observed on some of the δ/δ grain boundaries and a few rod shaped intragranularly nucleated austenite particles in the interior of the δgrains. Widmanstätten austenite was not observed to form at all, probably because the rate of formation of allotriomorphic austenite had not yet been slowed down, as would be expected to occur when the δ boundaries are continuously decorated. At 1000 and 900°C the main phases in the microstructure were the allotriomorphic and Widmanstätten austenite and a few intragranularly nucleated austenite particles were also observed, Fig. 6.19 b. The maximum rate of transformation was at 900°C and generally the volume fraction of austenite was lower compared with the finer δ grain size specimens discussed earlier, which is consistent with the hypothesis that the transformation is nucleation controlled with the particular heat treatments used. It should be noted that the sensitivity of the transformation to the grain size is expected to be lower for weld metals which contain many non-metallic inclusions which can act as nucleation sites. In alloy SH, nucleation on inclusions was observed as shown in Fig. 6.20.

In summary, for wrought alloy SH, high transformation temperatures seem to lead to the formation of more or less continuous layers of allotriomorphic austenite, with secondary plates of Widmanstätten austenite following soon afterwards. As the transformation temperature is lowered, the amount of allotriomorphic austenite increases, as does Widmanstätten austenite. However, the tendency to form the intragranular austenite increases with undercooling, presumably because nucleation on inclusions becomes easier as the driving force for transformation increases. Consequently, the intragranular austenite increases in volume fraction, and becomes more refined since the nucleation density is higher. At the lowest of transformation temperatures, the absence of Widmanstätten austenite is probably because of the rapid intragranular formation of γ which stifles the formation of any Widmanstätten austenite.

♣ $D^*_\delta = 600\mu$m as measured by lineal intercept method.

Fig. 6.20: optical micrograph showing the nucleation of intragranular austenite on inclusions in a sample of wrought alloy SH after being air cooled after solution treatment at 1250°C for 72 hours.

6.2.6 Isothermal Transformation of Alloy SHP

As mentioned earlier, it was possible to obtain in this alloy, a fully ferritic microstructure by quenching from the ferritisation temperature in iced-brine. This is because the alloy contains mainly Fe, Cr, Ni, and Mo, and only traces of interstitial elements, carbon and nitrogen. Samples of retained δ were rapidly heated to 800, 900 and 1000°C for isothermal reaction for 800 seconds, followed by quenching using a jet of helium gas. The results illustrated in Fig. 6.21 show that it was possible to detect an incubation time. Avrami plots (Fig. 6.22), did not show a straight line throughout the course of transformation, three slopes can be detected, the first slope indicates a reaction which is grain boundary controlled at the early stage of transformation. The results obtained demonstrate the importance of the absence of the interstitial solutes in decelerating the $\delta \rightarrow \gamma$ transformation.

The microstructure of the isothermally transformed specimens consisted of continuous allotriomorphic layers of austenite on the δ-ferrite grain boundaries (Fig. 6.23), from which a network of Widmanstätten side plates were observed to grow. Acicular austenite was also observed in the interior of the grains. The length of the Widmanstätten plates formed in this alloy was shorter than that observed in samples of alloy SH. This is believed to be due to the effect of the intragranularly nucleated austenite on stifling the formation of the Widmanstätten austenite, since alloy SHP contains a much higher oxygen content relative to alloy SH. Samples of SHP were also directly transformed from the ferritisation temperature and were observed to have a similar microstructure to that discussed for the "upquenched" ♣ specimens.

♣ rapidly heated from the ambient temperature to the isothermal temperature of interest.

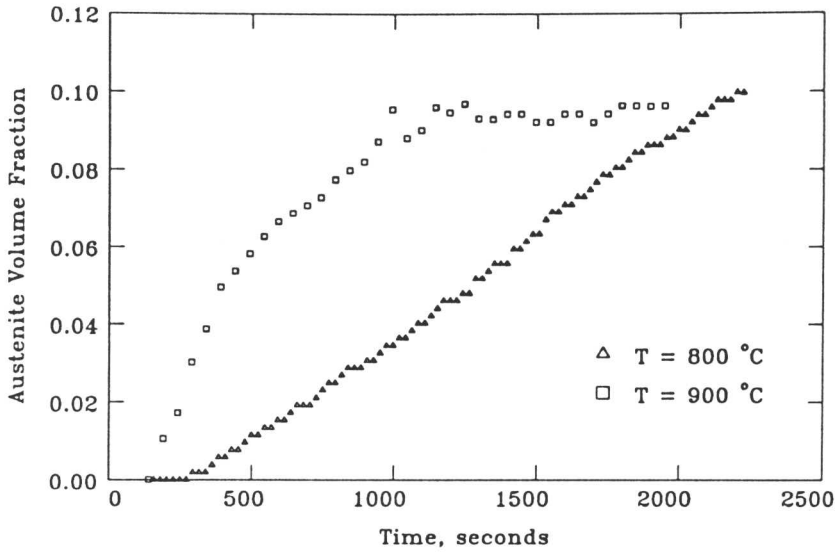

a

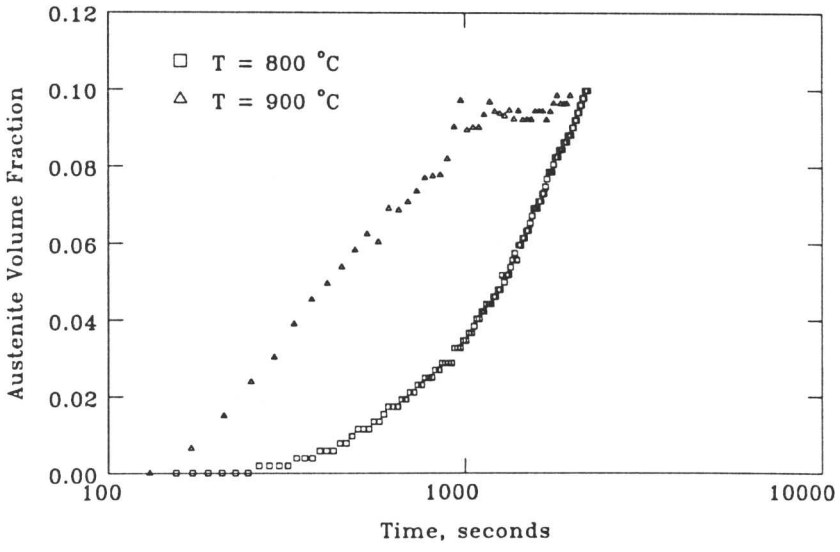

b

Fig. 6.21: Isothermal transformation diagrams showing the austenite volume fraction as a function of time for alloy SHP. Fully ferritic samples were upquenched to the isothermal temperatures.

(a) linear time scale; (b) log time scale.

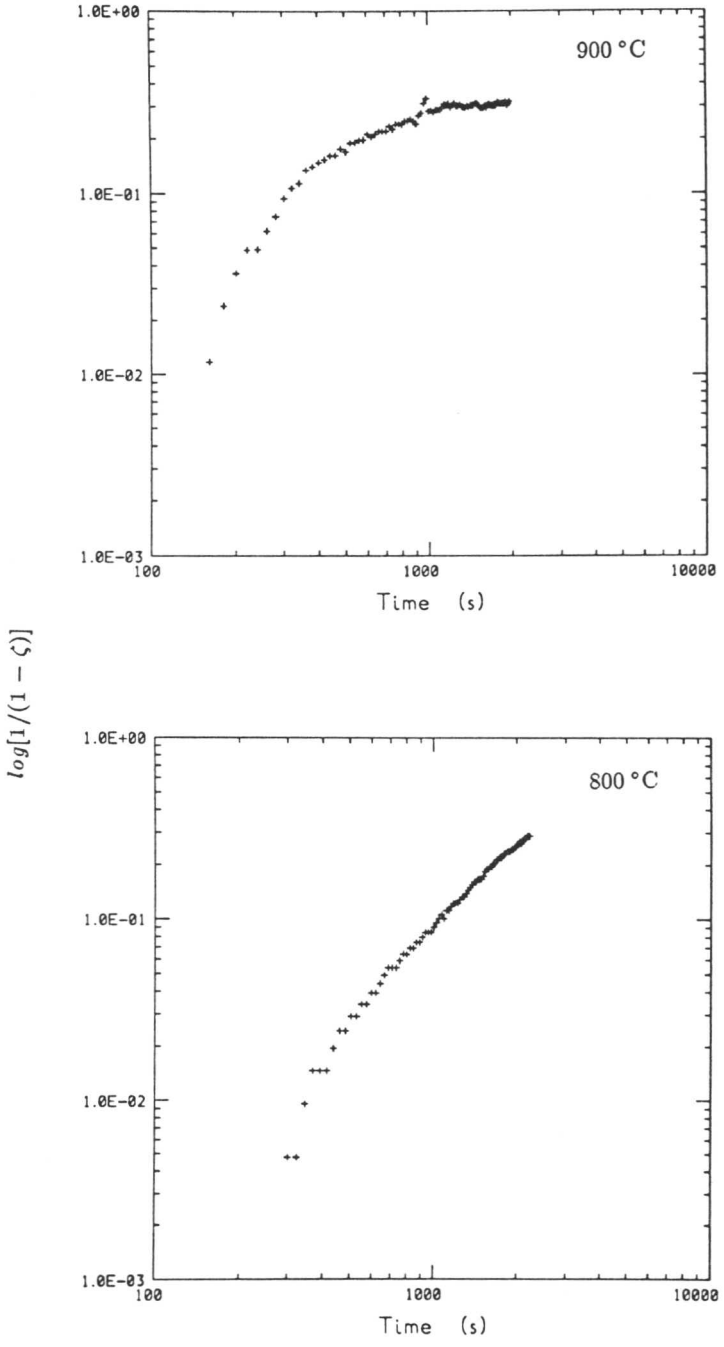

Fig. 6.22: Analysis of isothermal transformation diagrams, wrought alloy SHP.

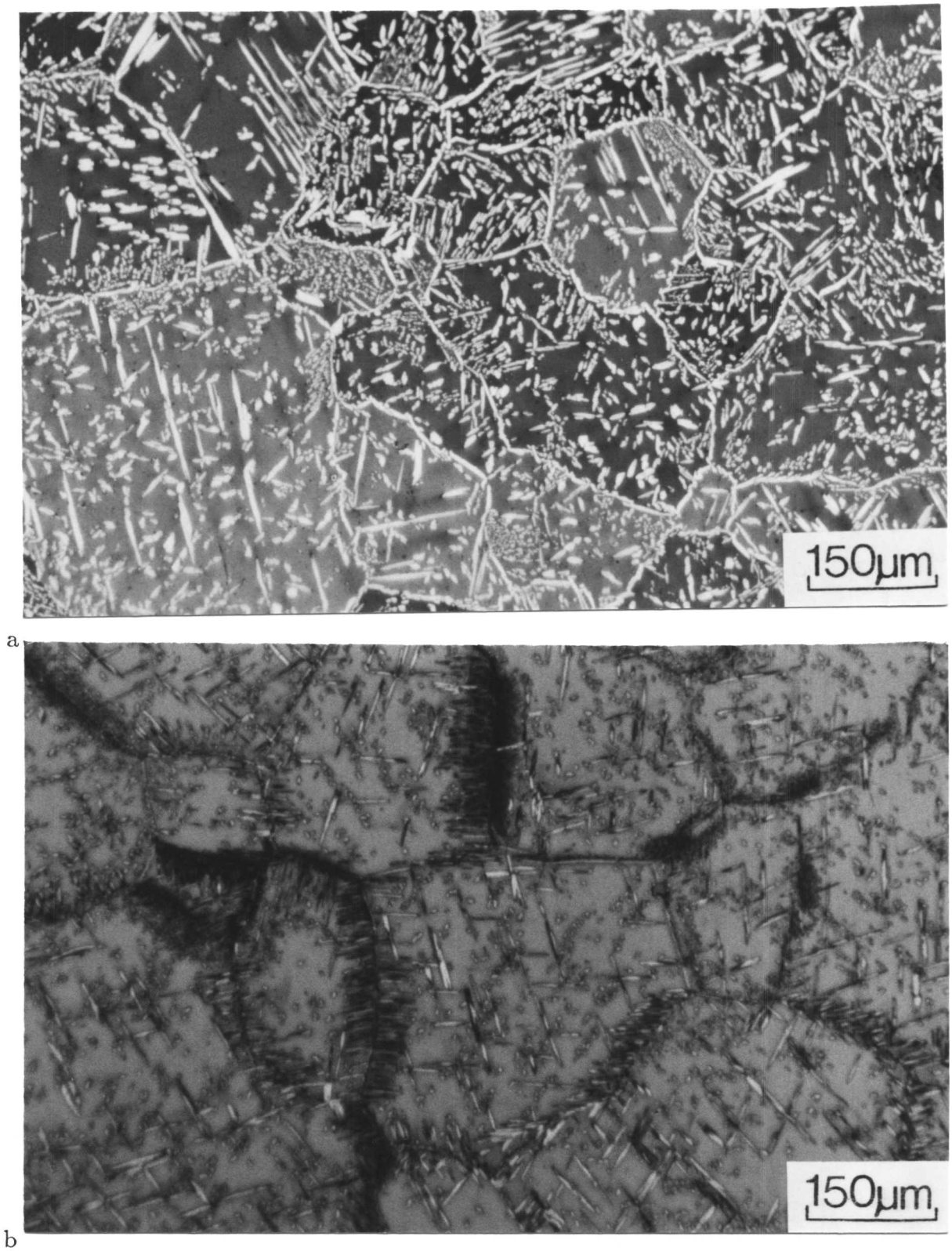

Fig. 6.23: Microstructure of isothermally transformed specimens of alloy SHP. (a) At 900°C and (b) at 800°C. The light etching phase is austenite.

6.2.7 Isothermal Transformation Diagrams for Alloy W111

Swaged samples of alloy W111 were, prior to isothermal transformation, homogenized at 1150°C for 48 hrs. The dilatometric specimens were ferritised at different temperatures (1240, 1260, 1290 and 1300°C) in an attempt to investigate the effect of T_δ and δ grain coarsening on the kinetics of the $\delta \rightarrow \gamma$ transformation at 1000, 900 and 800°C isothermal temperatures. The different ferritising temperatures were not found to have a large effect on δ-ferrite coarsening. The nonmetallic inclusions present were found to have a pinning effect which retarded grain growth. However, specimens treated 1300°C for 42 hrs were observed to have extremely large δ-ferrite grains. Nevertheless, it can be concluded that the δ coarsening process is comparatively slower in alloy W111 than in the wrought alloy SH of nearly similar composition except for oxygen content, which is much lower in alloy SH. The oxygen content is usually considered to be a measure of inclusion content in steels. The kinetics of the $\delta \rightarrow \gamma$ transformation was observed to be faster in weld alloy W111 when compared with the wrought steel SH Fig. 6.24. The $\delta \rightarrow \gamma$ transformation is completed at 1000°C after $\approx$ 50 seconds of reaction in weld alloy W111 where it takes $\approx$ 200 seconds for wrought alloy SH at the same isothermal temperature. This is believed to be a result of the higher carbon and nitrogen contents of the weld metal, and perhaps of the higher oxygen content which may provide an enhanced number density of intragranular nucleation sites. As expected the maximum volume fraction of austenite obtained after 300 s at 900°C was higher than that at 1000°C for the same time period. At 800°C the two stage reaction discussed earlier in this chapter was again noticed with this alloy, and the transformation was not observed to reach completion after 300 seconds of isothermal reaction time.

6.2.8 Metallography of Isothermally Transformed Weld Alloy W111

Transformation at 1000°C

At this temperature, the allotriomorphic austenite layers formed on the δ grain boundaries were observed to be thicker than those obtained with the wrought alloy SH. This is because of faster kinetics of the $\delta \rightarrow \gamma$ transformation due to higher carbon and nitrogen contents. The thickness of the γ allotriomorphs was observed to be irregular and the overall shape, nonuniform. In addition, discontinuities in the allotriomorphic layers were also observed. Widmanstätten austenite plates were observed at this temperature. Intragranular formation of acicular austenite on inclusions was also observed Fig. 6.25.

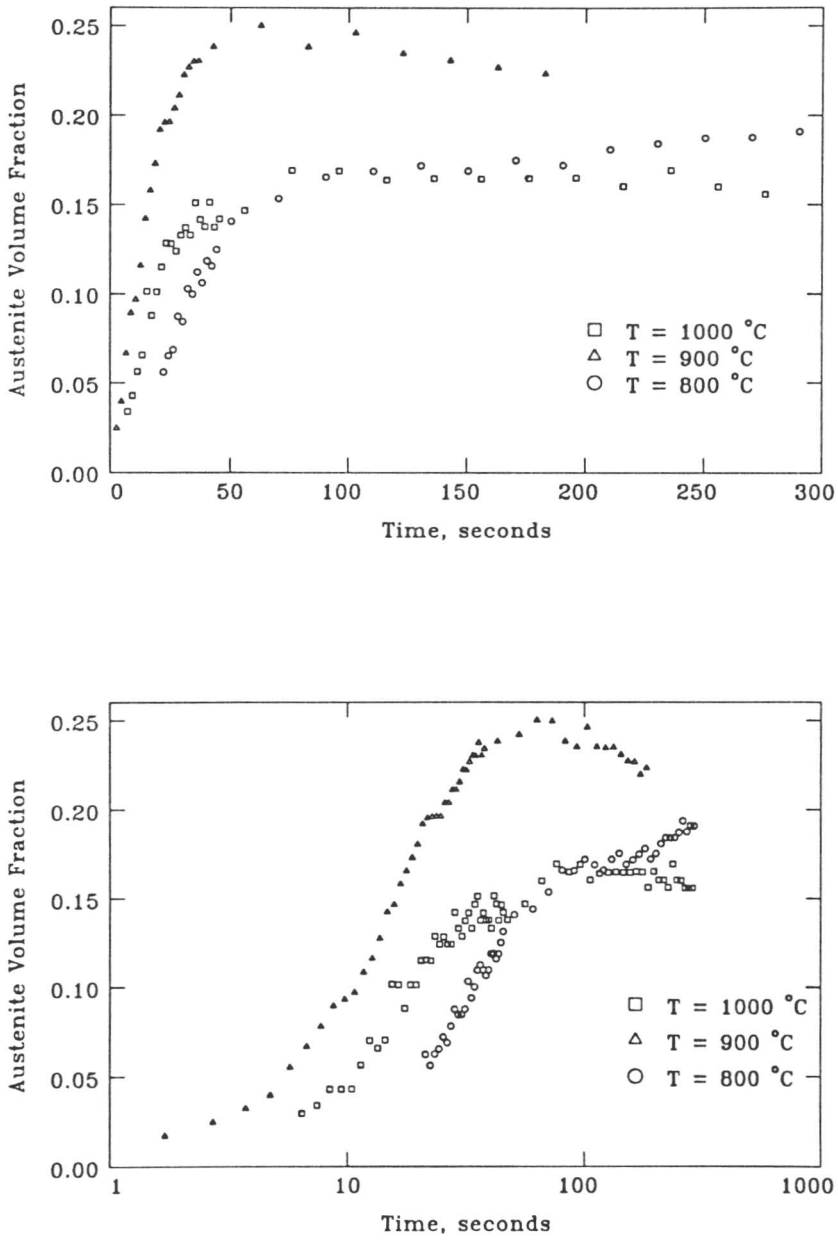

Fig. 6.24: Showing isothermal transformation diagrams of the volume fraction of austenite as calculated from the observed length changes, versus $\delta \rightarrow \gamma$ reaction time, for alloy W111. ($T_\delta = 1290°C$, ferritisation time = 2 mins).

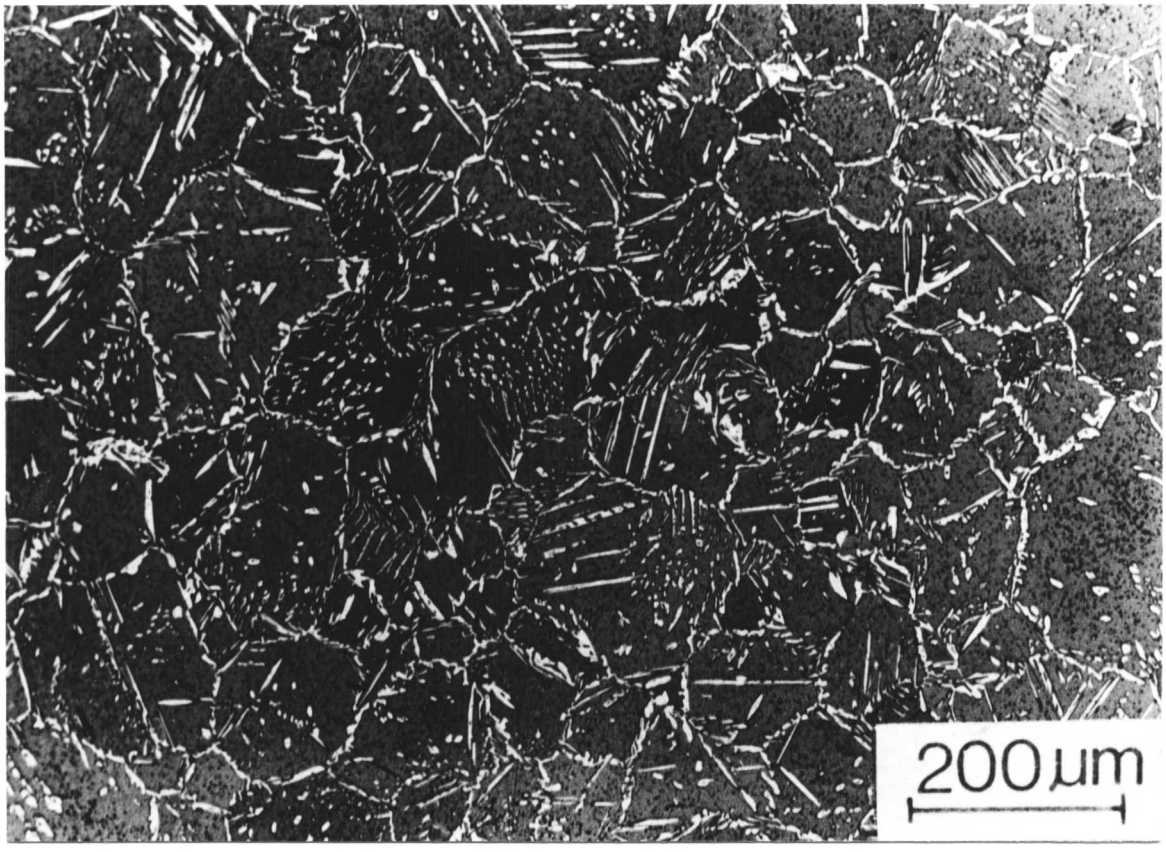

Fig. 6.25: Optical micrograph showing the microstructure of a sample of welded alloy W111 isothermally transformed at 1000°C.

Transformation at 900 and 800°C

The essential features of the microstructure were as described for transformation at 1000°C (Fig. 6.26). In addition, a cellular growth of austenite and $M_{23}C_6$ was observed to occur from the γ allotriomorphs, the growth exhibiting a leaf like shape in planar sections Fig. 6.27. This is believed to be a result of the relatively high carbon concentration of the alloy and possibly the presence of a higher level of silicon. Silicon is believed [2] to have the effect of increasing the activity of carbon in austenite. However, the role of silicon yet needs more investigation to be established.

Transmission electron microscopy (Fig. 6.27 b) and EDX microanalysis revealed the formation of $M_{23}C_6$ carbide at the δ/γ interface. The precipitation was associated with all austenite morphologies and it was also observed at Widmanstätten austenite plates tips (Fig. 6.27 c). The precipitation is believed to have happened as a result possibly of the redistribution of the substitutional alloying element as the austenite grew. The microanalysis test results of the phases after isothermal treatment at 800°C for 300 s are shown in Table 6.4.

Table 6.4: Compositions (wt.%) of phases in W111 specimen isothermally transformed at 800°C for 300 seconds measured using EDX microanalysis on transmission electron microscope. The analysis ignores the presence of interstitials.

Phase	Fe	Cr	Ni	Mo	Mn	Si
γ-allotriomorph	63.4 ±0.6	26.6 ±0.5	6.1 ±0.3	1.6 ±0.3	1.2 ±0.2	1.3 ±0.3
γ-Widmanstätten	64.3 ±0.6	25.4 ±0.5	6.8 ±0.3	1.1 ±0.3	1.3 ±0.2	1.1 ±0.2
γ-intragranular	62.1 ±0.6	26.7 ±0.5	7.1 ±0.3	1.6 ±0.3	0.95 ±0.2	1.6 ±0.3
δ-ferrite	63.1 ±0.6	26.6 ±0.5	6.0 ±0.3	1.4 ±0.3	1.4 ±0.2	1.5 ±0.3
$M_{23}C_6$	45.7 ±0.6	45.7 ±0.6	3.4 ±0.3	2.7 ±0.3	1.6 ±0.2	0.8 ±0.3

The microanalysis results showed no differences in composition between the thick (bulky) allotriomorphs of austenite and δ-ferrite which suggest, that this austenite is formed possibly by a massive transformation mechanism. The Widmanstätten austenite composition compared with that of δ shows partitioning in the substitutional solutes which suggest a reconstructive transformation. Partitioning of nickel is obvious in the intragranular austenite, but Cr and Mo showed no partitioning within the limits of experimental error. This could be explained by higher diffusion coefficient of nickel compared to chromium and molybdenum.

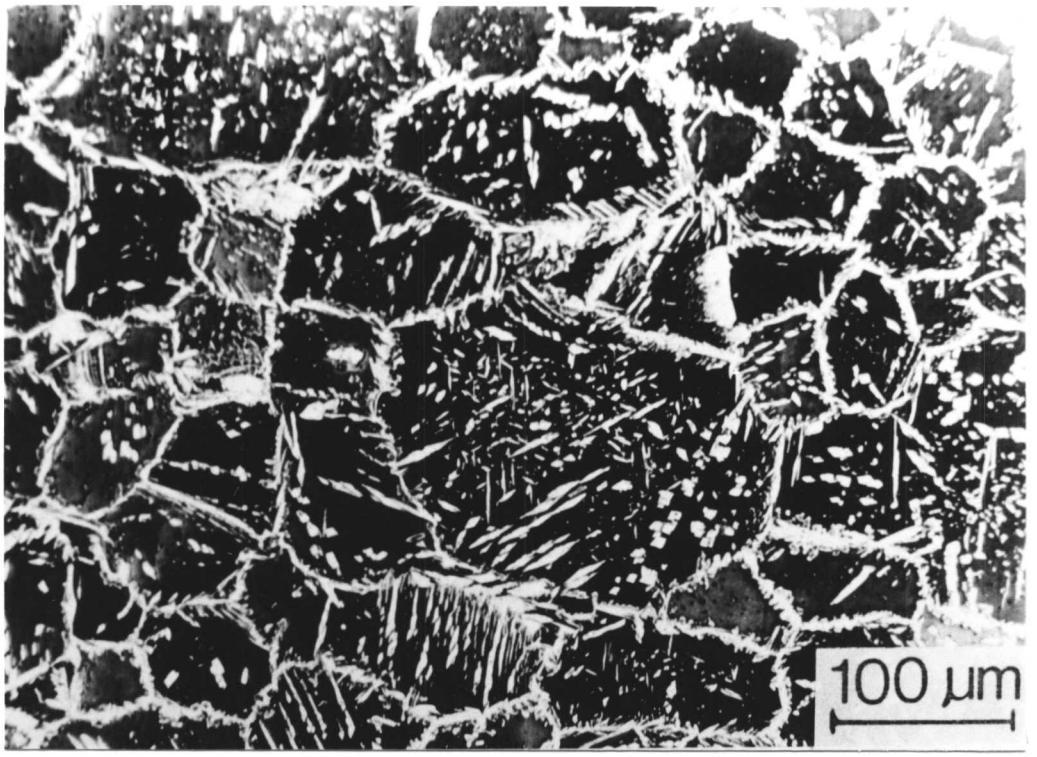

Fig. 6.26 a: Optical micrographs showing the microstructure of samples of welded alloy W111 after isothermal transformation at 800°C for 300 seconds. (T_δ = 1300°C, for 1 sec).

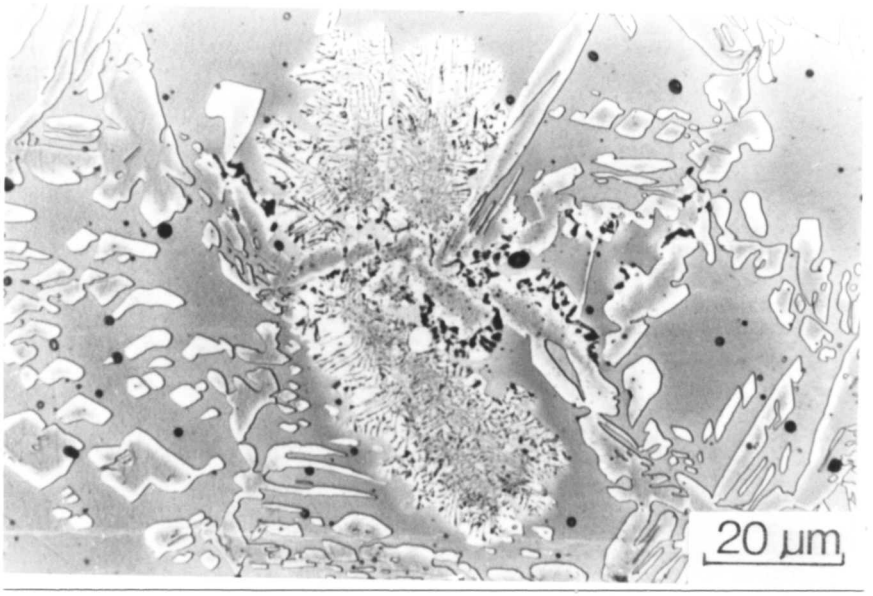

Fig. 6.26 b: Optical micrographs showing the microstructure of samples of welded alloy W111 after isothermal transformation at 900°C for 300 seconds. (T_δ = 1300°C, ferritisation time = 1 sec).

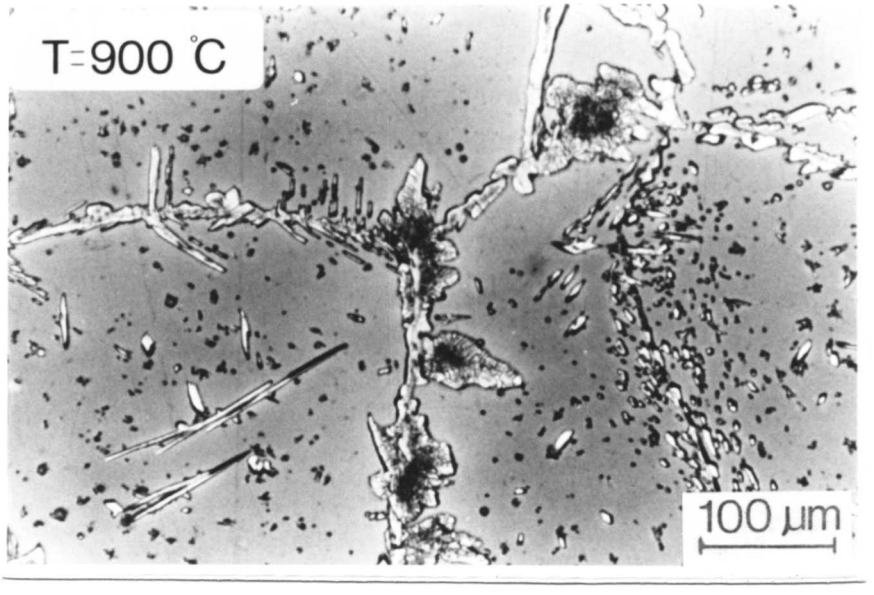

Fig. 6.27 a: "Leaf shape like" cellular growth of austenite and $M_{23}C_6$ observed in a sample of welded alloy W111 after isothermal transformation at 900°C for 300 seconds. (T_δ = 1300°C, ferritisation time = 1 sec).

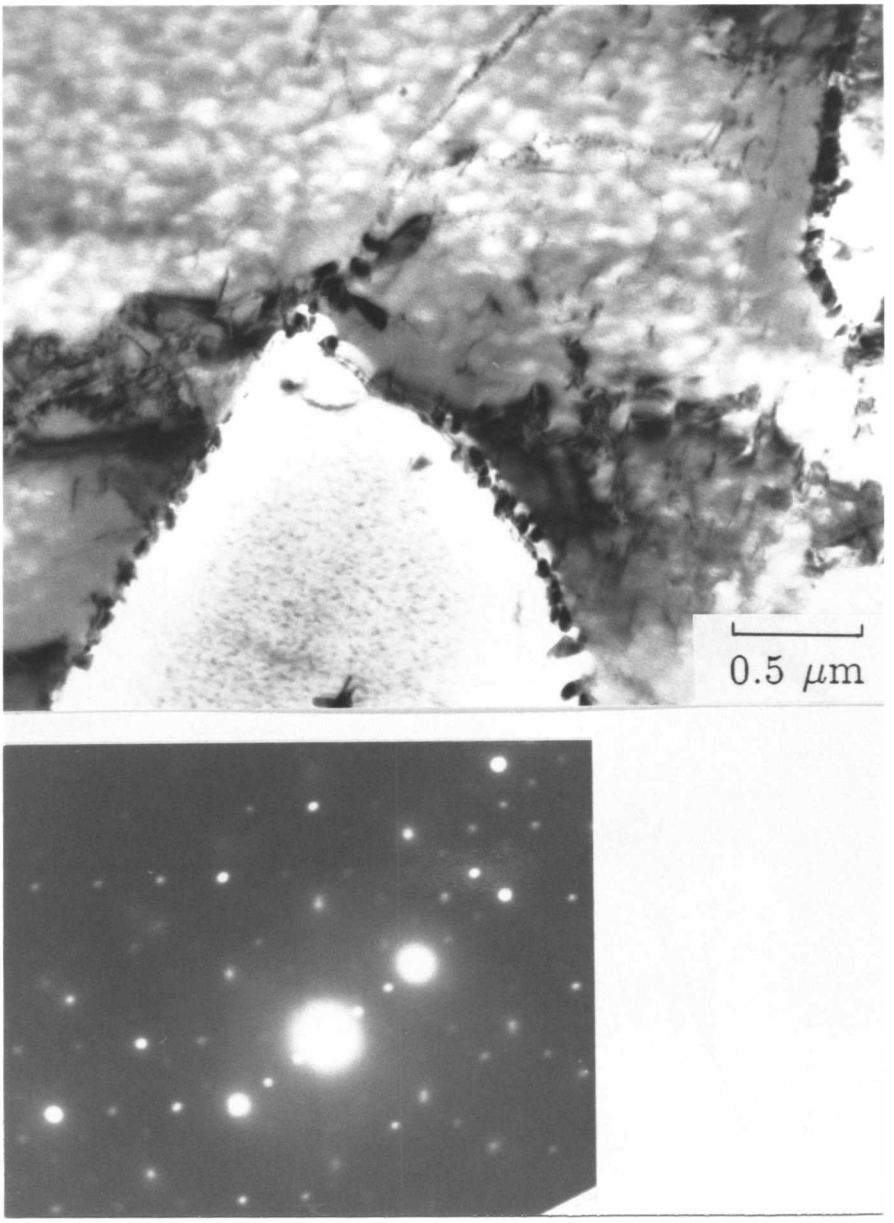

Fig. 6.27 b: TEM bright field image and selected area diffraction pattern (SADP) of $M_{23}C_6$ carbides formed on δ/γ boundaries in a sample of welded alloy W111 after isothermal transformation at 800°C for 300 seconds. SADP shows a cube-cube orientation relationship, zone axis [011].

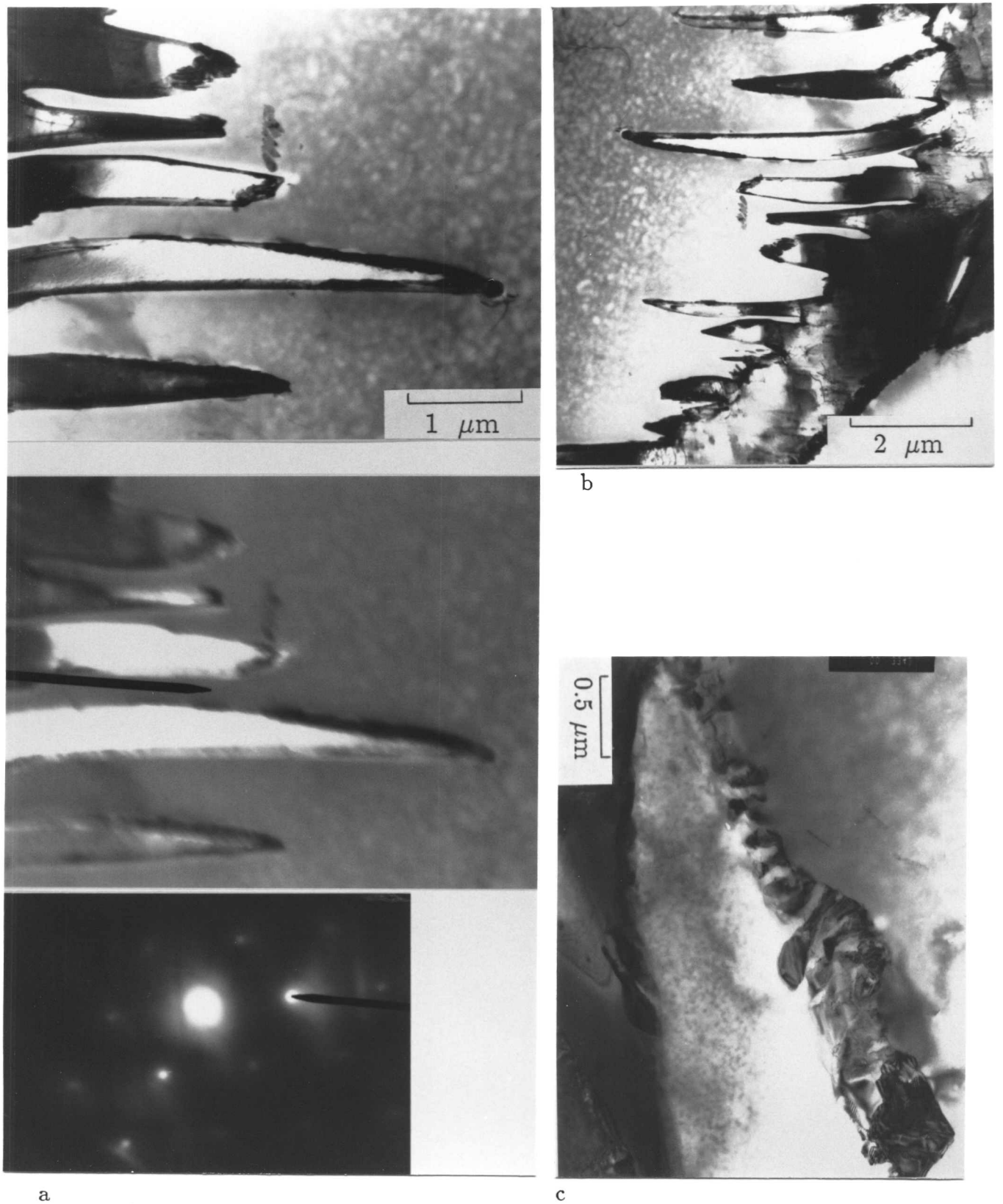

Fig. 6.27 c: TEM bright and dark field images of Widmanstätten austenite side plates (a) enimating from the austenite allotriomorph (b) in a sample of welded alloy W111 after isothermal transformation at 800°C for 300 seconds. Zone axis $[011]_\gamma$. (C) $M_{23}C_6$ formed at Widmanstätten austenite/δ-ferrite interfaces.

A remarkable effect of decarburization happening at the ferritisation temperature, on the overall austenite volume fraction obtained at the isothermal transformation temperature, was observed between the outer surface of the specimen and its core (Fig. 6.28). It is evident from Fig. 6.28 that the loss of carbon and nitrogen slowed down the kinetics of the $\delta \rightarrow \gamma$ transformation. Even when specimens were helium quenched $\delta \rightarrow \gamma$ transformation could not be suppressed except at the outer surfaces, which emphasizes the coupled effect of the loss of interstitials and the cooling rate. This matter was also pointed out by Solomon *et al.*, [3]. In their investigation they showed that the degree of decarburization can be rather large.

The pinning effect of nonmetallic inclusions on the grain coarsening of δ was observed in most of the transformed specimens Fig. 6.29. On the other hand no significant differences in the overall shape of the austenite particles were observed with changes in T_δ, as pointed out earlier.

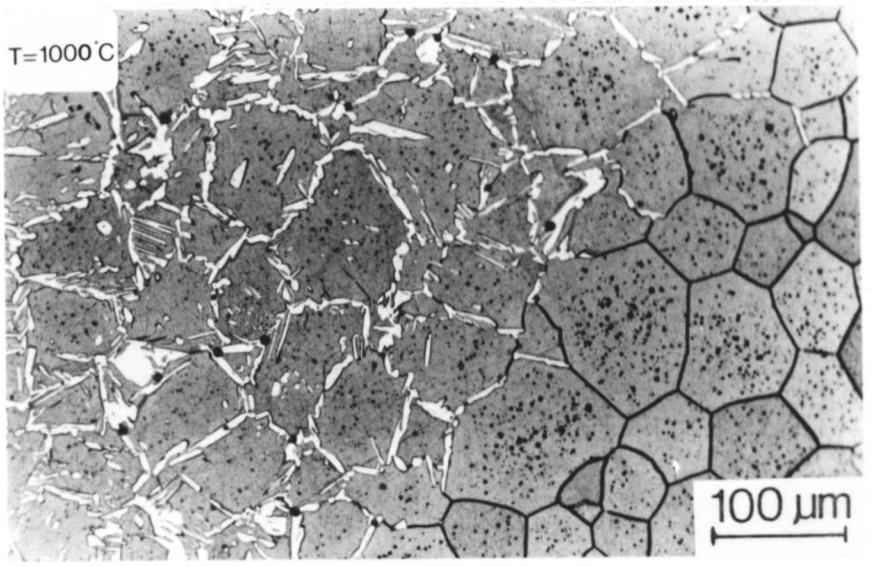

Fig. 6.28: Optical micrograph showing the decarburized region (free of austenite), observed at the outer surface of a sample of welded alloy W111 after isothermal treatment at 1000°C for 300 seconds. (T_δ = 1300°C, ferritisation time = 60 seconds).

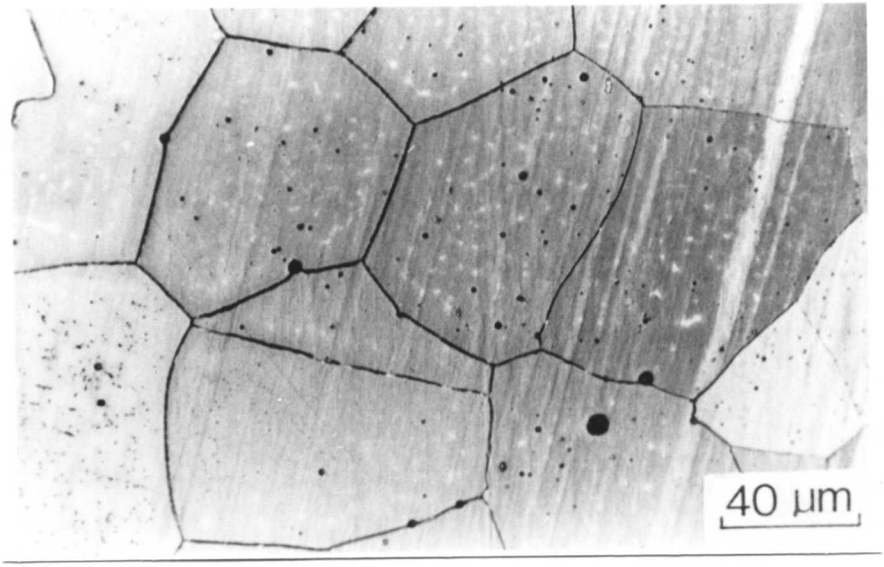

Fig. 6.29: Optical micrograph showing the pinning effect of non-metallic inclusions on the δ-ferrite grain boundaries in welded alloy W111.

6.3 Analysis of Isothermal Transformation Diagrams

Experimental determinations of dimensional changes as a function of time and temperature have been shown to enable the estimation of austenite formation kinetics during the $\delta \rightarrow \gamma$ transformation in duplex stainless steels. If the Avrami [4,5,6] equation is applicable, the data can be analysed by plotting curves of loglog$[1/(1-\zeta)]$ against log t where ζ is the normalised volume fraction (V/V_e), where V is the measured austenite volume fraction and V_e is the equilibrium volume fraction of austenite. Such curves can in principle reveal information about the mechanism of transformation.

6.3.1 The Johnson-Mehl [7] Avrami Equation

This equation was derived originally to describe the nucleation and growth of randomly nucleated spheres. It was assumed that nucleation and growth occur simultaneously throughout the course of transformation, and that the nucleation rate (I) is constant throughout the process. The growth rate G of the product phase was also assumed constant during transformation.

If the incubation time before the detectable nucleation of a sphere is τ, then at time t the period of growth will be $(t-\tau)$. The radius r of the sphere at time t is then given by $G(t-\tau)$, and hence the volume of sphere at time t by $\frac{4}{3}\pi G^3(t-\tau)^3$. The number of spheres nucleated in time $d\tau$ in a sample volume of V is equal to $VId\tau$, so that the volume of the product phase formed in the time interval $d\tau$ is :

$$VI\frac{4}{3}\pi G^3(t-\tau)^3 d\tau$$

Hence the total volume of the new phase, V_x, formed in time t is given by :

$$V_x = \int_{\tau=0}^{\tau=t} VI\frac{4}{3}\pi G^3(t-\tau)^3 d\tau \tag{6.7}$$

The volume fraction ζ is defined as $(\frac{V_x}{V})$ *i.e.*

$$d\zeta_x = \frac{4}{3}\pi IG^3(t-\tau)^3 d\tau \tag{6.8}$$

But $d\zeta_x$ is a change in the extended volume and not the real volume, since nucleation should not be occurring in the volume of material already transformed, and impingement between particles is also not accounted for. According to Avrami [4,5,6] the relationship between the extended volume fraction ζ_x and the real volume fraction ζ is as shown below :

$$d\zeta = (1 - \zeta)\, d\zeta_x \tag{6.9}$$

Therefore accounting for the extended volume fraction and impingement, the real volume fraction of the product phase will be given by the equation below :

$$\zeta = 1 - \exp\left(-\frac{1}{3}\pi I G^3 t^4\right) \tag{6.10}$$

which may be expressed more generally as

$$\zeta = 1 - \exp\left(-kt\right)^n \tag{6.11}$$

For the specific assumptions discussed above, the meanings of the terms k and n are clearly understood. However, in many cases, the equation in its general form can be used to deduce the nature of k and n by fitting to experimental data. The constants can then help in the interpretation of transformation behaviour.

6.3.2 Analysis of Isothermal Transformation Diagrams of Samples BW, WR4 and W111

Analysis of the isothermal transformation diagrams on the basis of Johnson-Mehl, Avrami type equation diagrams of samples BW, WR4 and W111 (Figs. 6.30, 6.31, 6.32), reveals that the $\delta \rightarrow \gamma$ transformation does not follow the general form of the equation when used empirically, the graphs do not show straight lines throughout the course of transformation. Some of the graphs show a transition from one slope to another. For instance, the curves for alloy SHP (Fig. 6.22) can be approximated into three regions with slopes from about 2.5 to 0.5 to 0.15. For alloy W111 a slope at the early stages of about 3 is observed, suggesting that the transformation at this stage is grain boundary controlled. The curves of BW and WR4 do not follow the same pattern for all temperatures and change slope with time for each specific temperature. More work is needed in this area to derive physically meaningful forms for the Avrami equation in the context of duplex stainless steel. In particular, it is necessary to establish the nucleation and growth data separately, so that the approximations inherent in eq. 6.10 can be justified or otherwise.

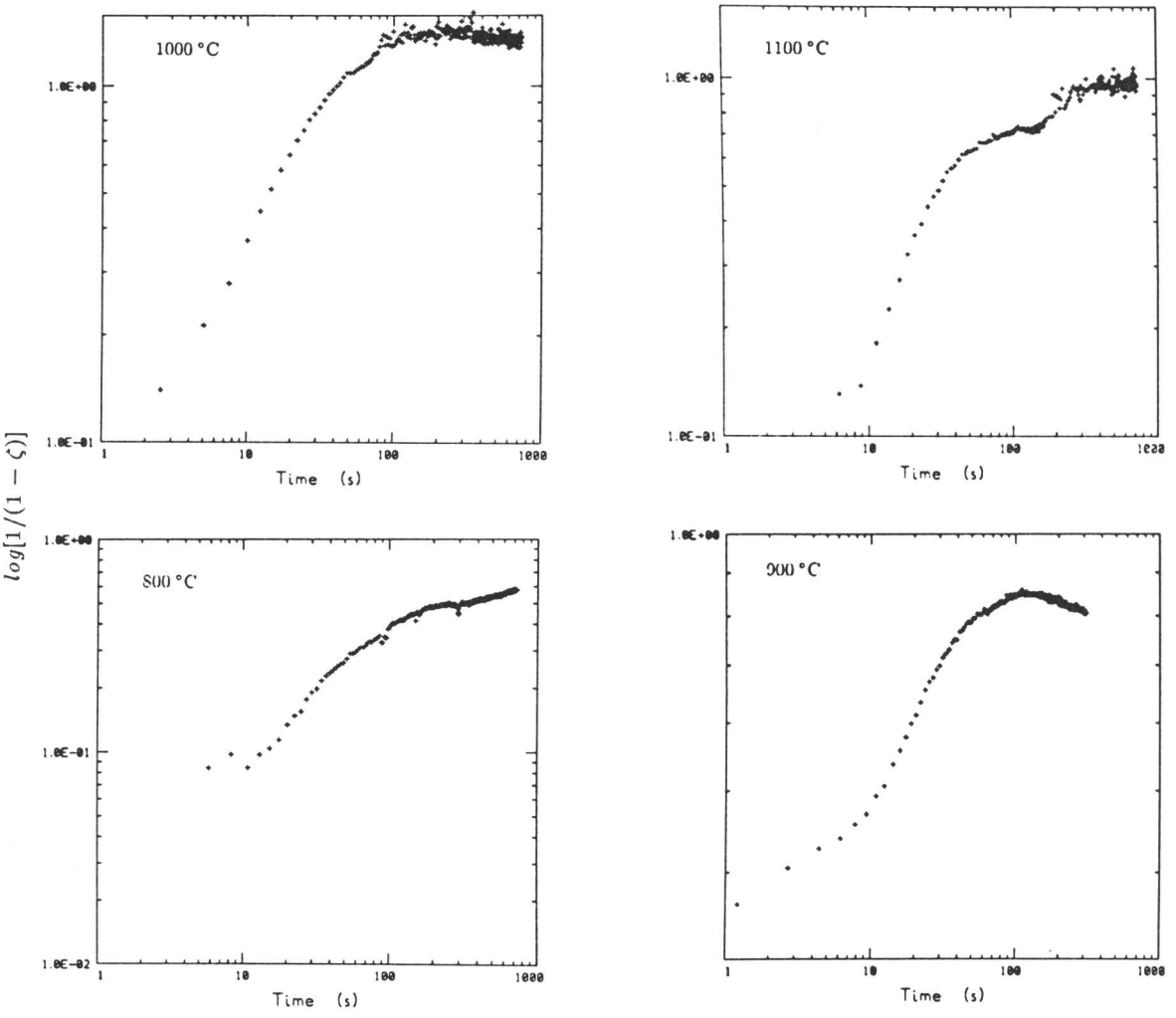

Fig. 6.30: Analysis of isothermal transformation diagrams of welded alloy BW in terms of a Johnson-Mehl Avrami type equation.

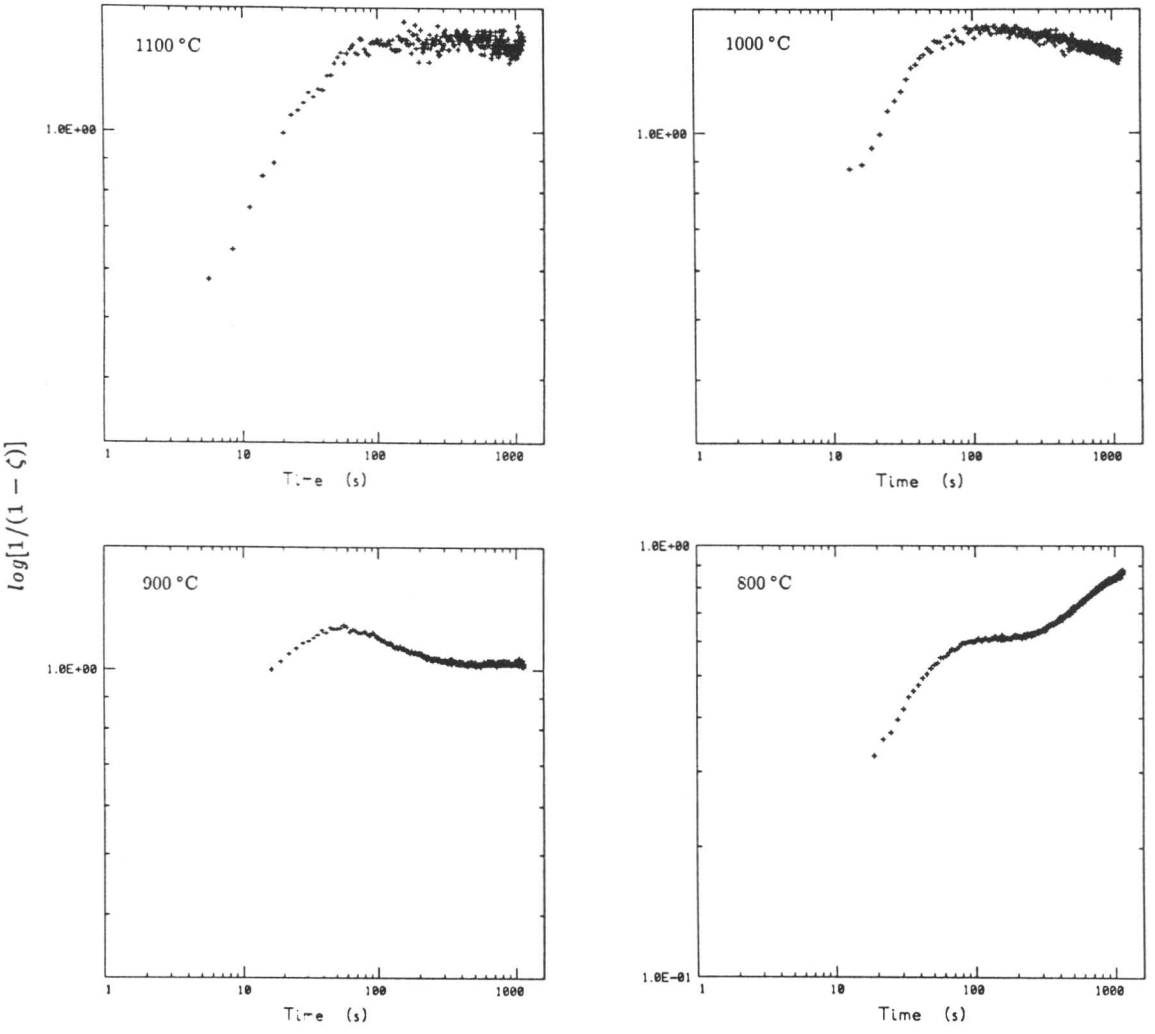

Fig. 6.31: Analysis of isothermal transformation diagrams of welded alloy WR4 in terms of a Johnson-Mehl Avrami type equation.

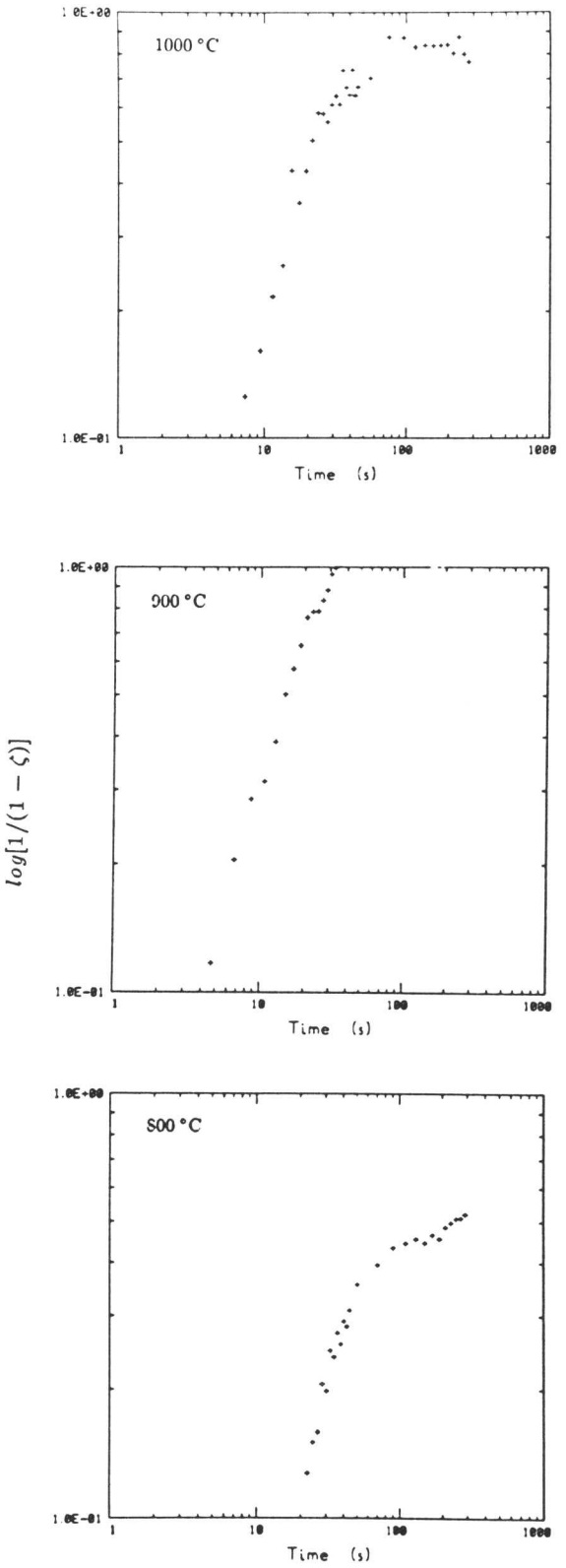

Fig. 6.32: Analysis of isothermal transformation diagrams of welded alloy W111 in terms of a Johnson-Mehl Avrami type equation.

6.4 The Effect of δ Grain Size on $\delta \rightarrow \gamma$ Transformation Kinetics

Grain growth phenomena are important in determining the microstructure and the related mechanical and corrosion properties in steels and weld metals, and particularly, in the heat affected zones produced during weld fabrication processes. An understanding of grain growth theory may enable a better approach towards the prediction of the HAZ microstructure. It has already been pointed out in (Chapter 5) that duplex stainless steel welds possess a narrow HAZ with austenite volume fractions less than the desired level required for optimum mechanical and corrosion properties.

In this section, the results of an investigation on the effect of the δ-ferrite grain size in duplex stainless steel wrought and weld metal are presented and discussed.

6.4.1 Grain Growth Theory

In a recrystallised metal, the driving force for grain growth is the surface energy associated with the grain boundaries. As the grains grow in size and their number density decreases, the grain boundary area per unit volume diminishes and the total surface energy is lowered accordingly. The grains of a metal are three dimensional in character. Five basic mechanisms by which the geometrical properties of the three dimensional grains can change have been discussed by Rhines [8]. A brief summary of these mechanisms is shown in Fig. 6.33.

Grain boundary movement in metals is, in many respects, analogous to the movement of cell walls in soap froths. In both cases, the boundaries in general move towards their centers of curvature, and the rate of this movement varies with the amount of curvature. On the other hand, while it is known that the growth of soap cells can be explained in terms of the simple diffusion of gas molecules through the walls of the soap film, less is known about the mechanism by which atoms on one side of a grain boundary cross the boundary and join the crystal on the other side.

Assuming that metallic grain growth occurs as a result of surface energy considerations and the diffusion of atoms across the grain boundary [9], then the grain growth

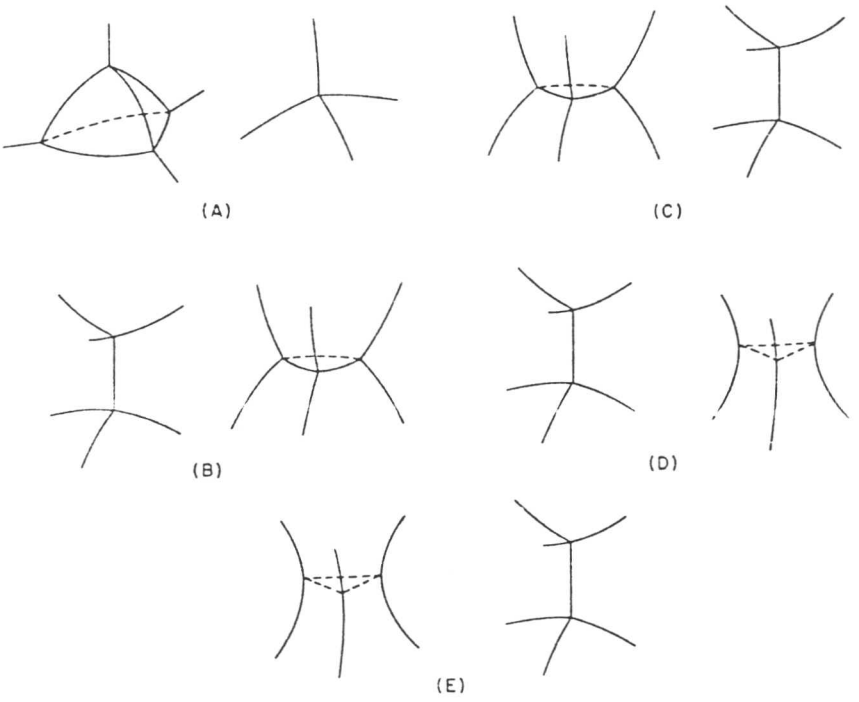

Fig. 6.33: Basic mechanisms by which the change in the geometrical properties of three dimensional grains can occur [9].

at any given temperature might be represented by equation 12 below:

$$D^2 - D_\circ^2 = Kt \tag{6.12}$$

where

D is the average grain size in an aggregate of grains after time t

$D_\circ$ is the initial average grain size at the start of the observations ($t = 0$)

K is a constant of proportionality

If the diffusion of atoms across the grain boundary is considered to be a thermally activated process then,

$$K = K_\circ e^{-Q/RT} \tag{6.13}$$

where

Q = empirical heat of activation

T = temperature in degrees Kelvin

R = universal gas constant

so that equation (6.12) can be rewritten as follows:

$$D^2 - D_\circ{}^2 = K_\circ t e^{-Q/RT} \tag{6.14}$$

Most published experimental results do not conform well to this grain growth law, nor to the often used approximation

$$D = kt^{\frac{1}{2}}$$

where

$$k = \sqrt{K} = \sqrt{K_\circ e^{-Q/RT}}$$

probably because the temperature dependence of grain growth does not usually give constant values for Q in the expression

$$k = k_\circ e^{-Q/2RT}$$

where $k_\circ = \sqrt{K_\circ}$ or because other factors, such as inclusions, interfere with the motion of grain boundaries in a manner inconsistent with the model. On the other hand many of the experimental data correspond to empirical formulae of the form $D = kt^n$, where

the exponent n is usually smaller than $1/2$ and is not constant for a given metal or alloy [9].

Foreign atoms in solid solution may migrate to the neighbourhood of the grain boundary to reduce the strain energy due to the difference in size relevant to the solvent atoms, as the grain boundary is a region of misfit. This segregation can then hinder the subsequent movement of the grain boundary.

Particles in the form of inclusions (oxides, sulphides) or a second phase particles can inhibit grain growth in metals. An approximate theory for the interaction between inclusions and grain boundaries was presented by Zener (1948) [10]. He proposed that the drag of a particle on a boundary is equal to the pull of the boundary on the particle and is given by

$$f = 2\pi r\sigma cos\theta sin\theta \tag{6.15}$$

where;

σ indicatesthe direction and magnitude of surface-tension stress at the circular line of contact (in three dimensions) between the grain boundary and the surface of the inclusion,

θ is the angle between the equilibrium position of the boundary and the vector σ,

r is the radius of the spherical particle,

it follows that f is maximum when $\theta = 45°$ so that the maximum force on the boundary is equal to $\pi r\sigma$ (Fig. 6.34).

At high temperatures the inclusions and second phase particles may dissolve or coalesce and in both ways their effect of retarding grain growth will be reduced. Holes or pores can have the same effect on grain growth as inclusions.

The effect of thermal grooving as characterised by Mullins (1958) [11] on grain growth is shown in Fig. 6.35. Grain boundary grooves tend to anchor the ends of the boundaries where they meet the surface, and must form with a dihedral angle ψ that satisfies the relation:

$$\gamma_b = 2\gamma_{fs}\dot{cos}\frac{\psi}{2} \tag{6.16}$$

where γ_b is the surface tension of the boundary and γ_{fs} is that of the two free surfaces.

Finally preferred orientation of the crystal structure of metals has generally been observed to reduce the grain growth rates [9].

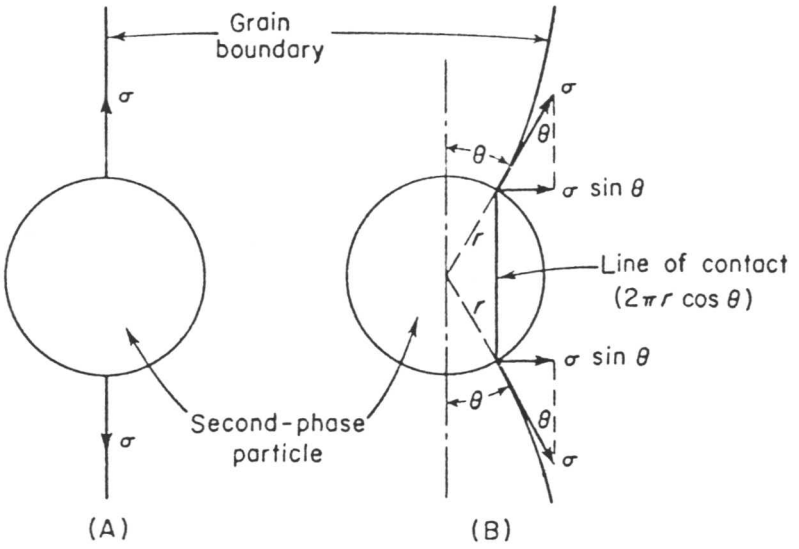

Fig. 6.34: The interaction between an inclusion and a grain boundary [10].

(A) Sperical inclusion location in a grain boundary represented as a straight line.

(B) Inclusion and boundary in a position of mechanical equilibrium.

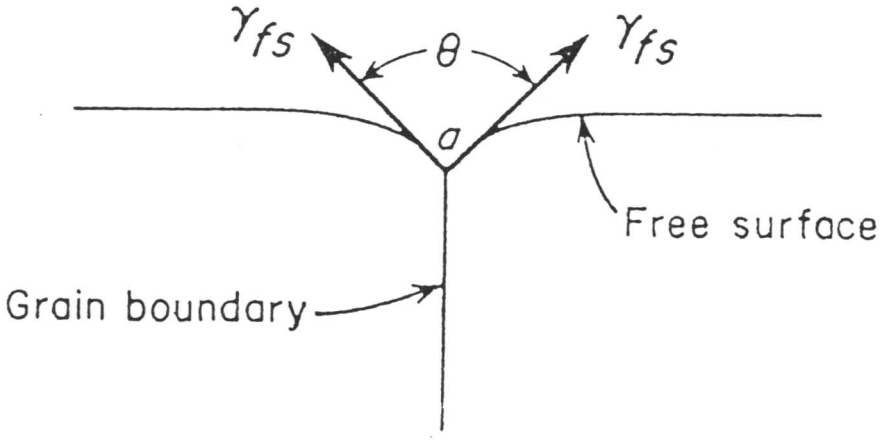

Fig. 6.35: The effect of thermal grooving on grain growth [11].

6.4.2 Prediction of the HAZ Grain Size

Most investigations in this area have been based on the assumption of a thermally activated grain growth process controlled by the diffusion of the atoms across the interface. Alberry *et al.* [12] used experimental grain size measurements made on specimens of (Fe-0.5Cr-Mo-V wt%) steel subjected to simulated weld thermal cycles, in conjunction with the grain growth equation due to Burke and Turnbull [13] and heat flow equations due to Rosenthal [14], in an attempt to predict quantitatively the austenite grain size in the region of the heat affected zone adjacent to the fusion boundary in real welds, as a function of welding process heat input. For the weld thermal cycle applied, they found that the austenite was stable to 950°C on heating, and 550°C on cooling. Assuming that the weld thermal cycle $T(t)$ would be represented as a series of discontinuous isothermal steps, where the hold time is small and constant and equal to Δt, they expressed the austenite mean grain size D (mm) by summation of the weld thermal cycle over the time period $\Delta t_{(950-550°C)}$ (s) as follows:

$$D^{2.73} = \sum_{t950}^{t550} (5.4 \pm 0.6) \times 10^{12} \exp\left(\frac{(-460,000 \pm 33,000)}{RT(t)}\right) \Delta t \qquad (6.17)$$

The idea of integrating the weld thermal cycle has been suggested by a number of investigators. Ashby and Easterling [15] produced diagrams based on an elementary kinetic model for grain growth and carbide dissolution, integrated over the weld cycle. Considering that the temperature dependence of the grain boundary mobility term is adequately described by an Arhenius type of relationship. They derive the following expression for the total grain size change during the heating cycle:

$$D_t^{\,n} - D_\circ^{\,n} = K \int_0^\infty \exp\left(\frac{-Q}{RT(t)}\right) dt \qquad (6.18)$$

The left hand side of the above equation depends only on the initial and final grain size, and for a fixed change in the grain size is constant, (H) and is equal to

$$H = \int_0^\infty \exp\left(\frac{-Q}{RT(t)}\right) dt \qquad (6.19)$$

Ion [16] refers to H as the "kinetic strength" since it reflects the total number of diffusive jumps which take place during the thermal cycle and respectively represent the extent of microstructural changes within the HAZ induced by the heat cycle T(t), and assuming that the peak temperature of the thermal cycle is the one responsible for the kinetic changes following the hypothesis that the grain growth process is diffusion

controlled, he approximated the peak temperature cycle to a parabola to obtain the expression

$$H = \left(\frac{2\pi RT_p}{Q}\right)^{\frac{1}{2}} t_p \exp\left(\frac{-Q}{RT_p}\right) dt \tag{6.20}$$

for a thick plate and

$$H = 2\left(\frac{\pi RT_p}{Q}\right)^{\frac{1}{2}} t_p \exp\left(\frac{-Q}{RT_p}\right) dt \tag{6.21}$$

for a thin plate.

The prediction of HAZ grain size in duplex stainless steel weld metals so far followed the above discussed approaches. Honeycombe and Gooch [17] followed the approach used by Alberry *et al.* [12] and Ikawa *et al.* [18] to describe the grain growth under isothermal conditions assuming a thermally activated diffusional process:

$$D_f^n - D_\circ{}^n = A[\exp(-Q_1/RT)](t_1 - t_2) \tag{6.22}$$

where

D_f and $D_\circ$ are the grain sizes after holding time at temperature T for times t_1 and t_2 respectively.

n is a grain growth exponent.

Q_1 is an appropriate activation energy.

R is the gas constant and

A is a material constant.

They did not obtain good agreement between the predicted and the measured grain sizes for the thermal cycles used. This discrepancy was attributed to the effect of variables such as cold work, boundary pinning by impurity elements or second-phase particles, and to the difficulty of measuring the initial grain size for some of the weld metals. Their results have shown that ≈90% of the grain growth occurs around the peak temperature of 1200°C (±50°C). It was only at this temperature that their results showed reasonable agreement between the measured and predicted grain size. Much of the grain coarsening was found to occur at temperatures above 1200°C, and no significant increase in the grain size was apparent from their experiments at temperatures below 1200°C. This is probably a consequence of the lack of grain growth of δ-ferrite as long as some austenite particles remain undissolved. On cooling the formation of austenite will tend to pin down the δ grain boundaries.

6.4.3 Experimental

As mentioned earlier, the δ grain size was found to exert a large effect on the overall austenite content of the isothermally transformed SH specimens. To be able to evaluate the sensitivity of wrought and welded duplex alloys to δ-ferrite grain size, controlled isothermal transformation experiments were carried out. Swaged rods of 3 mm outer diameter of wrought alloys SH, SHP, and weld alloy W111 were homogenized at 1100°C for 48 hours followed by quenching to ambient temperature. Homogenizing was performed in a tube furnace and the specimens were sealed in quartz capsules under a partial pressure of pure argon to prevent oxidation, decarburization and denitridisation. The isothermal treatments were performed using the Theta Industries high speed dilatometer described in chapter 4. They were then heated under vacuum either to the same T_δ for different time intervals or to different ferritisation temperatures to obtain different δ grain sizes. The specimens were then cooled to the same isothermal temperature by introducing a controlled jet of helium gas and were left there for the same period of time then quenched to the ambient temperature. The above described isothermal heat treatment was performed on the other specimens listed in Table 6.5 from the as-received condition.

The volume fraction of austenite was measured optically, as described in chapter four, directly or via a micrograph, using the Seescan image analyzer. The δ grain size was determined by two methods; lineal intercept method where $D^*_\delta = L/N$, where N is the number of grains counted in a defined length L, and the other by using the Seescan analyzer by means of a "ferret diameter" defined as the average of the averages of 36 diameters measured within each grain.

6.4.4 Experimental Results

The isothermal heat treatments details, the results of austenite volume fractions and δ-ferrite grain size measurements are shown in Table 6.5:

Table 6.5

Specimen -	T_δ $^\circ C$	t_{T_δ} s	T_{iso} $^\circ C$	$t_{T_{iso}}$ s	D^*_δ L.I. μm	D^*_δ S.S μm	V_γ DIL.	V_γ S.S	V_γ $Calc.$
SH1-Wr	1320	120	1000	1000	608	-	0.23	0.25 $\pm$ .04	0.29
SH2-Wr	1320	190	1000	1000	640	-	0.19	0.2 $\pm$ .037	0.29
SH3-Wr	1320	300	1000	1000	680	-	0.16	0.15 $\pm$ .02	0.29
SHP1-Wr	1180	120	900	3500	177	183	0.19	0.21 $\pm$ .03	0.247
SHP2-Wr	1200	25	900	3500	212	208	0.17	0.18 $\pm$ .03	0.247
SHP3-Wr	1230	50	900	3500	236	215	0.15	0.16 $\pm$ .02	0.247
SP1-Wr	1325	100	1000	300	489	547	-	0.36 $\pm$ .04	0.599
SP2-Wr	1310	100	1000	300	349	451	-	0.46 $\pm$ .042	0.599
SP3-Wr	1285	100	1000	300	286	343	-	0.51 $\pm$ .05	0.599
IC373A-Wr	1280	40	1000	570	184	204	-	0.4 $\pm$ .038	0.374
IC373B-Wr	1290	40	1000	570	234	269	-	0.37 $\pm$ .04	0.374
IC373C-Wr	1320	40	1000	570	442	499	-	0.3 $\pm$ .032	0.374
W111A	1240	10	1000	300	64	55	0.14	0.185 $\pm$ .03	-
W111B	1300	1	1000	300	82	80	0.17	0.17 $\pm$ .022	-
W111C	1300	60	1000	300	92	107	0.16	0.15 $\pm$ .02	-
BW1	1340	40	1000	230	237	438**	0.45	0.56 $\pm$ .04	0.641
BW2	1345	180	1000	230	273	433**	0.45	0.58 $\pm$ .04	0.641
BW3	1338	80	1000	230	268	484**	0.47	0.60 $\pm$ .045	0.641

where

D* = average grain size

L.I. = lineal intercept

S.S = Seescan image analysis

Dil. = measured dilatometric

$Calc.$ = calculated using equilibrium thermodynamics (chapter 7)

** = grain size measured on transverse cross section of the weld

Wr = wrought alloy.

Good agreement is obtained between the dilatometric and optically measured austenite volume fractions. The general trend that can be deduced is that the volume fraction of austenite decreases with the increase in δ grain size. The effect being more pronounced in wrought alloys possibly due to the lack of nucleation sites once the boundary sites are saturated.

Isothermal transformation curves of the volume fraction of austenite as a function of time, were determined for samples with different δ-ferrite grain sizes at 1000°C for wrought alloy SH and weld metal W111 (Figs. 6.36, 6.37). The isothermal transformation diagrams were derived from the dilatometric measurements of the relative length change following the approach described previously in section 6.1.1. The isothermal diagrams reveal two important results. Firstly the austenite formation kinetics in weld metal W111 are relatively insensitive to the δ-ferrite grain size. This is believed to be a consequence of the effect of non-metallic inclusions in providing intragranular heterogeneous nucleation sites for the austenite. The presence of intragranular oxide particles provides a reservoir of heterogeneous nucleation sites which does not vary with the δ-ferrite grain size. The wrought alloy on the other hand, has a lower oxygen concentration and is obviously more sensitive to δ-ferrite grain size variations (Fig. 6.38) since the δ/δ grain boundaries are the main nucleation sites for austenite.

These interpretations are confirmed by the fact that the overall transformation kinetics are clearly faster for the weld metal, which contains both δ/δ grain boundaries and inclusions as nucleation sites. Secondly, an additional effect of the inclusions is clearly to resist δ-ferrite grain growth in the referritised weld (Fig. 6.39), since, for the same ferritising conditions, the grain size obtained in alloy SH is much coarser.

The case with the wrought metal is in fact a simulation to that happening in the grain growth region of the heat affected zone in weld metal. It highlights the problems met with this region of the welded joint and explains the deficiencies in the volume fraction of austenite which lead, as a consequence, to inferior mechanical and corrosion properties, as reported in literature. The results obtained suggest that a solution for the heat affected zone problem may be possible by using oxide dispersed duplex stainless steel base plates.

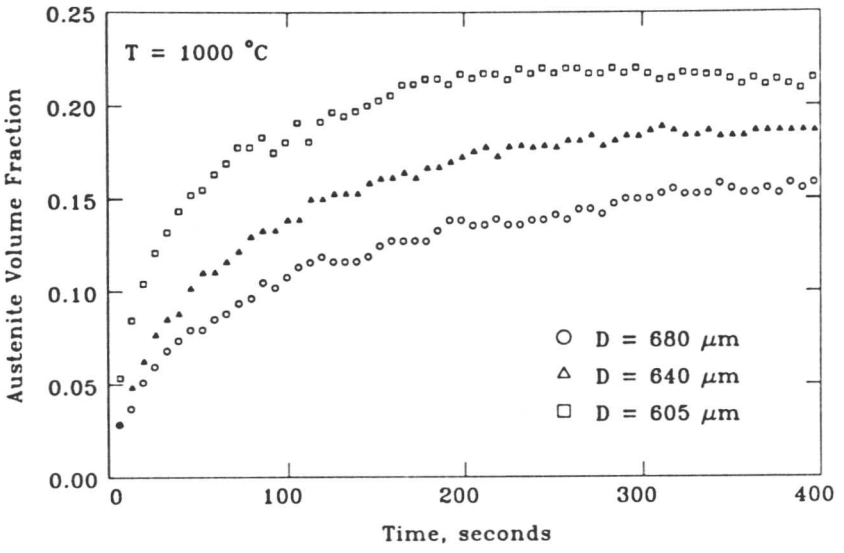

Fig. 6.36: Isothermal transformation data as a function of δ-ferrite grain size (D^*_δ) for wrought alloy SH.

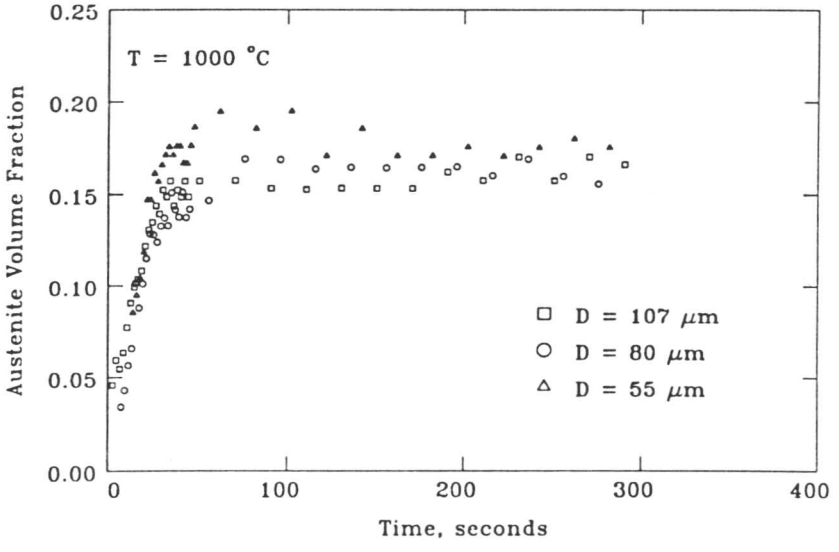

Fig. 6.37: Isothermal transformation data as a function of δ-ferrite grain size (D^*_δ) for weld alloy W111.

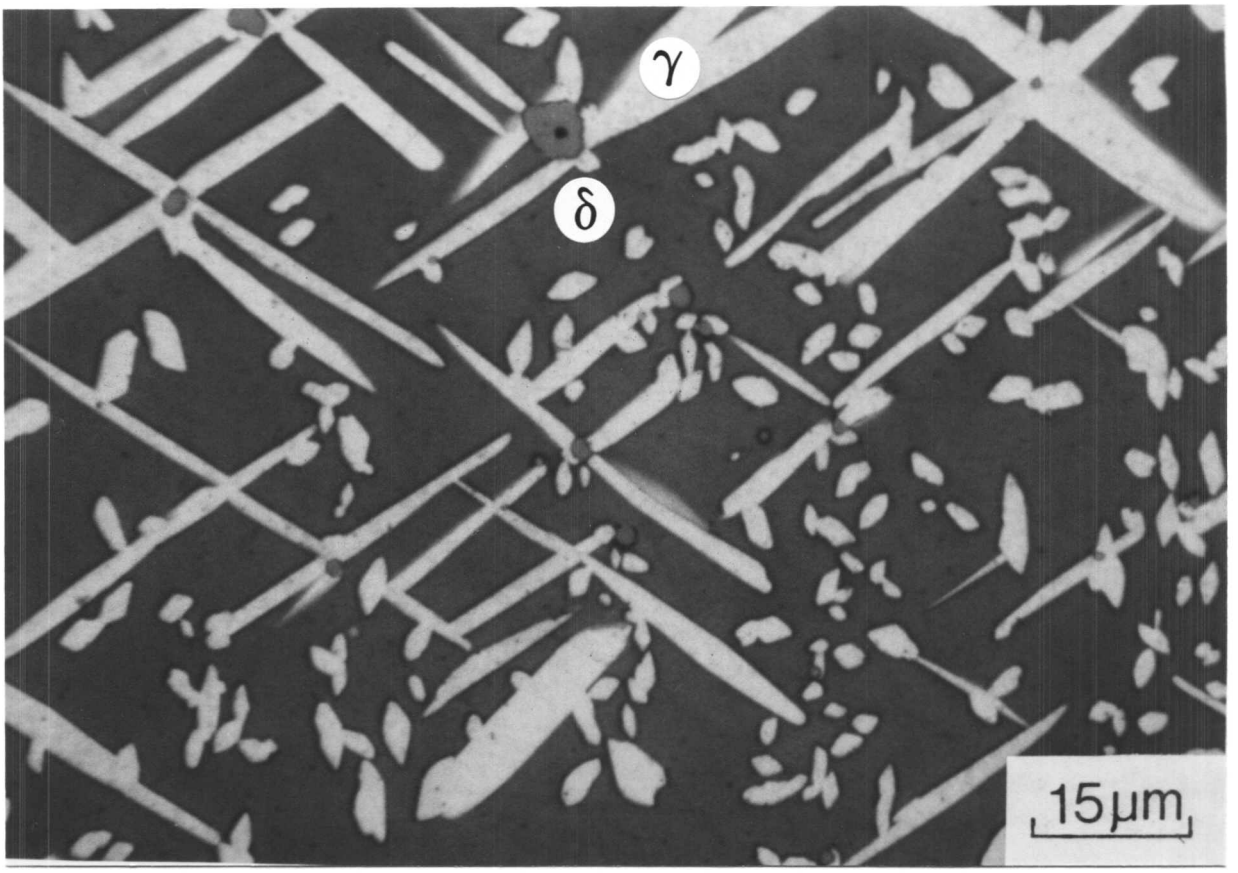

Fig. 6.38: Colour optical micrograph showing the formation of austenite on inclusions in the isothermally transformed weld alloy W111. The light etching phase is austenite. The specimen was etched by Beraha's colour etchant.

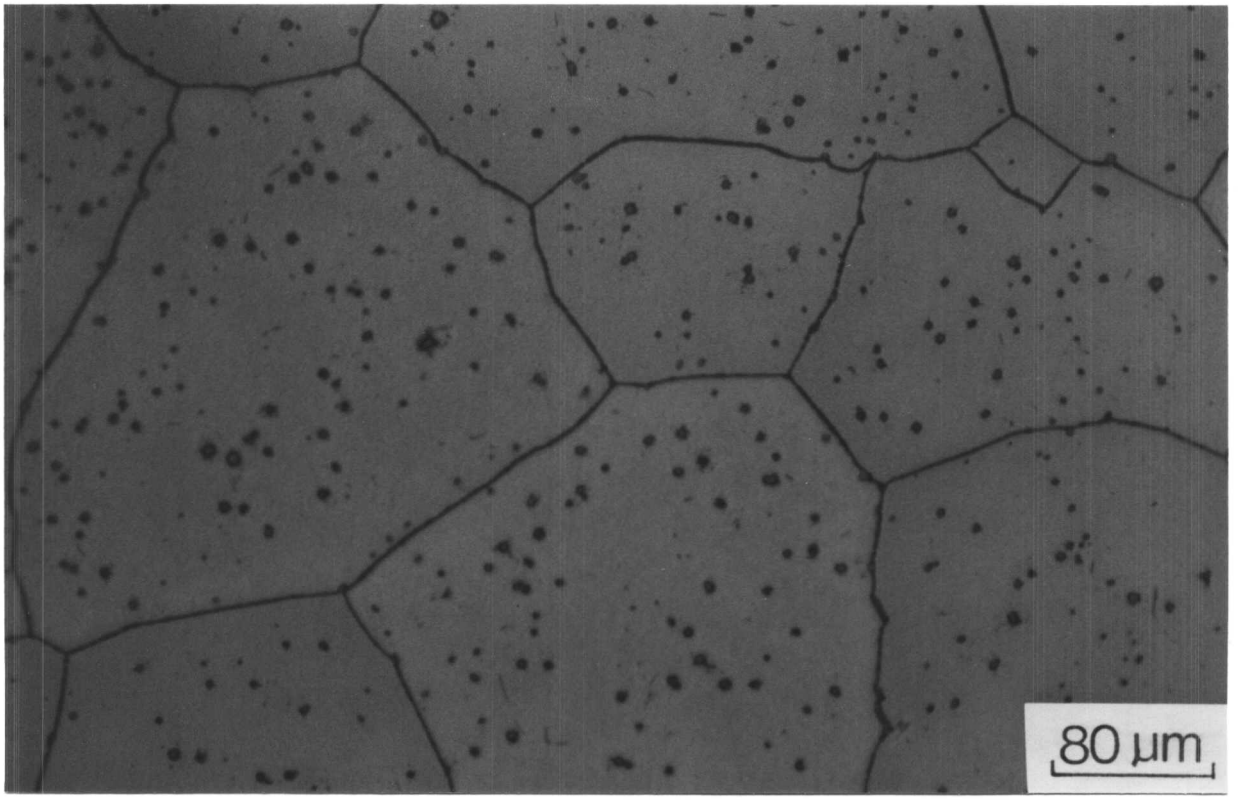

Fig. 6.39: The pinning effect of non-metallic inclusions on δ-ferrite grain boundaries in weld alloy (W111). The effect is evident from the cusps on the boundaries.

6.5 The Ageing Behaviour of Wrought and Welded Duplex Stainless Alloys

6.5.1 Introduction

When supersaturated retained δ is isothermally aged the microstructure obtained consists of finely dispersed austenite in a δ matrix [3]. The ageing may also lead to the precipitation of harmful phases like the chi and sigma phase. Post weld heat treatment of duplex stainless steel weld metals is expected to degrade the corrosion properties as a consequence of the precipitation of chromium carbides and nitrides *i.e.* sensitisation [19], although it may also be beneficial by increasing the volume fraction of austenite phase in the as-deposited regions in weld metals which are usually lower in austenite content compared with the reheated zones, as was shown in chapter 5. In this section, the results from an investigation of the ageing behaviour of wrought duplex stainless steel from the supersaturated δ condition in wrought alloy (SH) and from the as-received welded condition of weld metal (BW) are reported. The results were obtained using optical microscopy, electron microscopy and hardness measurements.

6.5.2 Ageing of Wrought Alloy SH

The as-swaged specimens of alloy SH were solution treated at 1320°C in a tube furnace as described in chapter 4, for 2 minutes and then quenched in iced brine to obtain a fully ferritic sample. However a single phase microstructure was not obtainable, and some austenite was always observed at the δ/δ grain boundaries. The estimated δ percentage after quenching is $\approx$ 98%. Specimens of this microstructure were rapidly heated to 900°C and aged for time periods 10, 25, 100, 1000, and 10000 seconds followed by quenching in iced-brine. The measured volume fractions of austenite after each time interval, as determined using the lineal intercept and image analysis methods are shown in (Table 6.6).

The microstructure revealed by optical microscopy after 10 and 25 seconds of $\delta \rightarrow \gamma$ reaction time was characterized by the formation of more or less continuous layers of allotriomorphic austenite at the δ/δ grain boundaries. The γ allotriomorphs were observed to grow on both sides of the δ boundaries, consistent with a reconstructive mechanism of transformation. Widmanstätten austenite plates and side plates were observed, their lengthening was found to be approximately constant for the time intervals investigated. Two intragranular austenite morphologies were observed within the δ grains. Relatively long acicular austenite plates which seemed to exhibit well defined crystallographic orientations, and a very fine austenite of a rod-like morphology. As the

Table 6.6. The volume fraction of austenite of SH specimens aged at 900°C, beginning with a microstructure of retained δ-ferrite and a very small volume fraction of austenite.

T_{ageing}(°C)	$t_{T_{ageing}}$(s)	V_γ (L.I.)	V_γ (S.S)
900	10	0.088	0.1
900	25	0.14	0.14
900	100	0.27	0.28
900	1000	0.38	0.34
900	3120	0.44	0.40
900	10000	0.47	0.45

where L.I. = lineal intercept and S.S = image analysis using "Seescan"

ageing time increased, it became more difficult to distinguish between the two intragranular morphologies as they grew in size. After 100 seconds of $\delta \rightarrow \gamma$ reaction time, precipitation were observed to occur in the vicinity of δ/allotriomorphic γ boundaries. After longer ageing time precipitation increased and extended to occur in addition to δ/allotriomorphic γ boundaries, at δ/γ boundaries of the mature intragranular austenite particles. Relatively thin austenite precipitates free zones could also be observed adjacent to the austenite allotriomorphs (Figs 6.40, 6.41, 6.42).

6.5.3 Effect of Retained δ Grain Size on The Ageing Behaviour of SH

To study the effect of δ-ferrite grain size on the ageing behaviour of wrought alloy SH, swaged rod specimens were ferritised at 1300°C, for 10, 60, 120, 240, and 540 seconds followed by quenching in iced brine to the ambient temperature, the rapid quench enabling the retention of most of the δ-ferrite to ambient temperature. These experiments enabled the study of the grain growth process of the δ-ferrite, its effect on the $\delta \rightarrow \gamma$ transformation, as well as the precipitation reactions occurring during subsequent ageing treatments. The δ grain size as a function of ferritising time is shown in Fig. 6.43. The mean grain size was measured on optical micrographs, using the lineal intercept method. The relation obtained is as described by equation below:

$$D_\delta^* = 151.3885\ t^{0.2011} \tag{6.23}$$

Where D_δ^* is the δ grain size (μm) and t is the ferritisation time in seconds. The correlation coefficient observed from fitting the equation 6.23 to the experimental data

was 0.93. The exponent n value obtained (≈ 0.2) suggest that the grain growth is normal.

The effect of δ grain size on the ageing behaviour of SH was studied by annealing the retained δ at 1000 and 800°C. The transformation of supersaturated δ of three different grain sizes (399, 433, and 630 μm) to austenite during ageing was investigated.

Ageing at 1000°C

The main features of the microstructure after ageing for 1000 seconds at 1000°C were as discussed earlier for samples aged at 900°C. It was observed that the size of the dominant intragranular austenite decreases with increasing δ-ferrite grain size and on the other hand the number of the observed Widmanstätten austenite plates increases with decreasing δ grain size. Some δ boundaries were observed to be free of γ allotriomorphs, although rods of intragranular austenite crossed these boundaries without deviation (Fig 6.44); this is strong evidence that these rods grow by a reconstructive transformation mechanism, since the coordinated atomic movements necessary for displacive reactions cannot be sustained across grain boundaries. Zones depleted from austenite were also observed adjacent to the δ/δ grain boundaries (Fig 6.45). This could be either a precipitation effect or a sectioning effect.

Ageing at 800°C

The specimens were aged for 1 hour at this temperature. The length of intragranular austenite plates was shorter compared with that observed at the 1000°C ageing temperature. Cellular growth of austenite and some unidentified precipitates was observed growing from the γ allotriomorphs (Fig. 6.46). Otherwise the results were like those obtained at 1000°C ageing temperature.

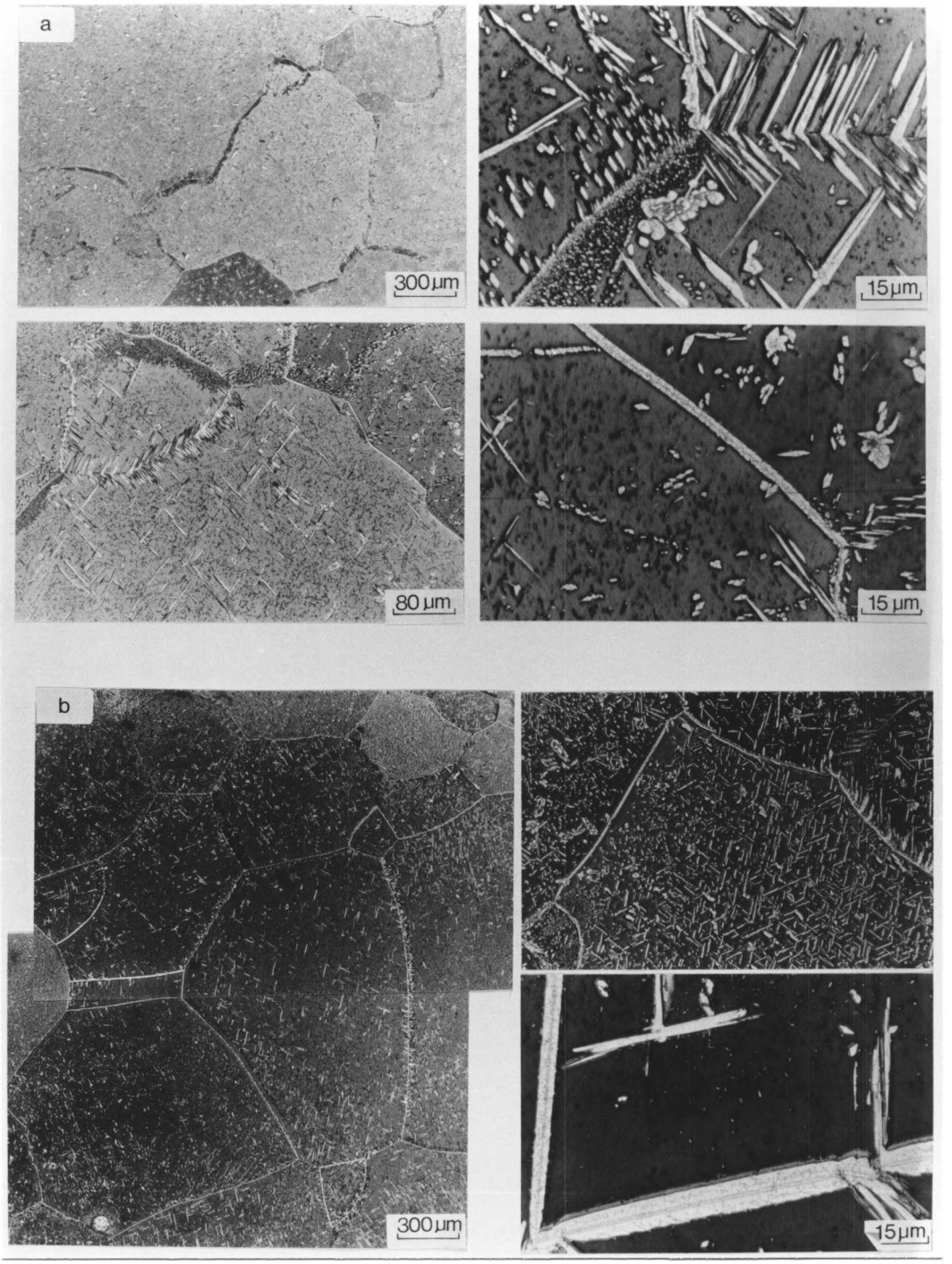

Fig. 6.40: The microstructure of wrought alloy SH after ageing from supersaturated δ-ferrite at 900°C for: (a) 10 seconds and (b) 25 seconds.

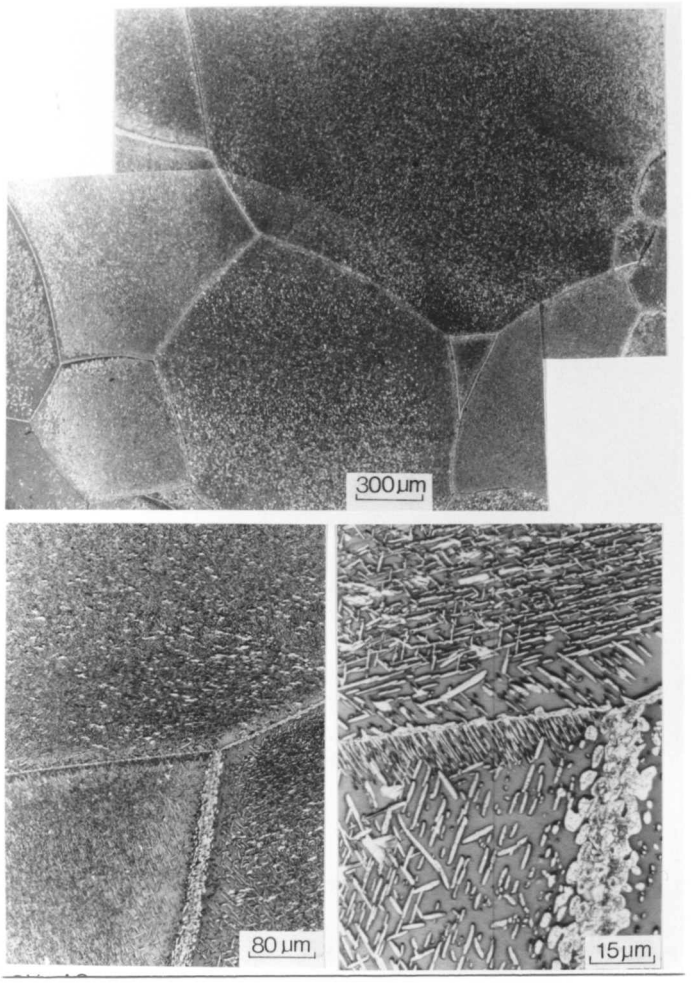

Fig 6.41: The microstructure of wrought alloy SH after ageing the supersaturated δ-ferrite at 900°C for 100 seconds.

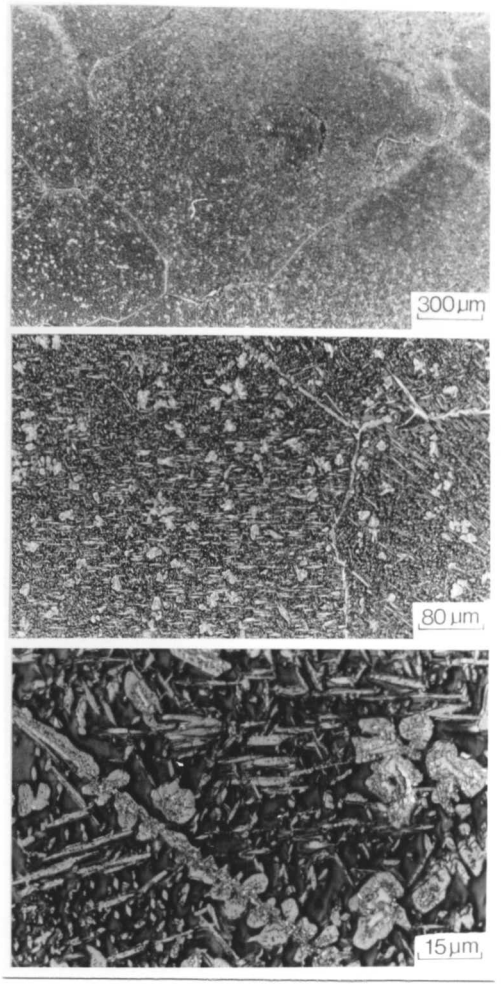

Fig 6.42: The microstructure of wrought alloy SH after ageing the supersaturated δ-ferrite at 900°C for 52 minutes.

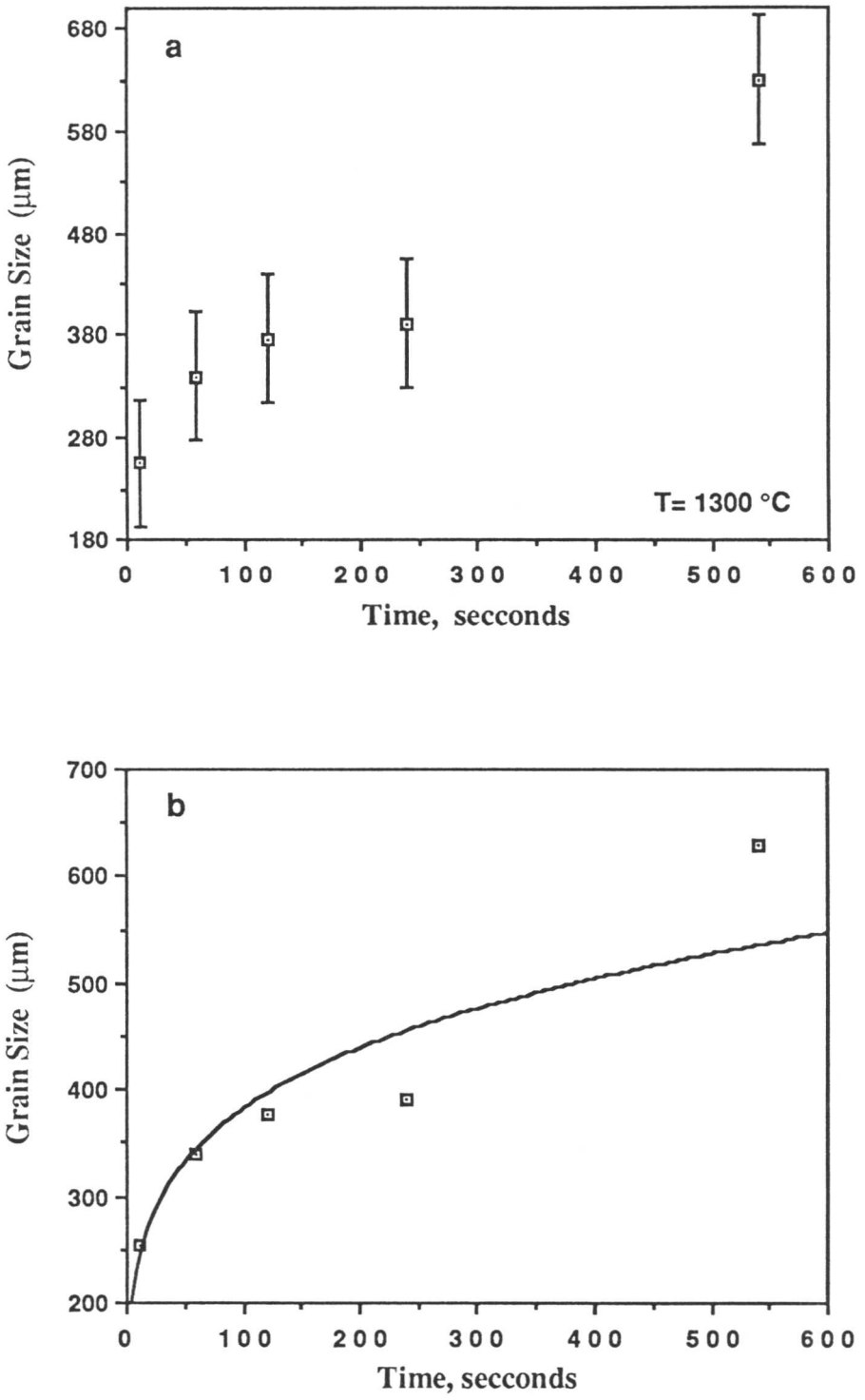

Fig. 6.43: (a) The δ-ferrite grain size as a function of ferritising time at 1300°C. (b) Fitted curve showing the growth rate exponent (n) to be about 0.2.

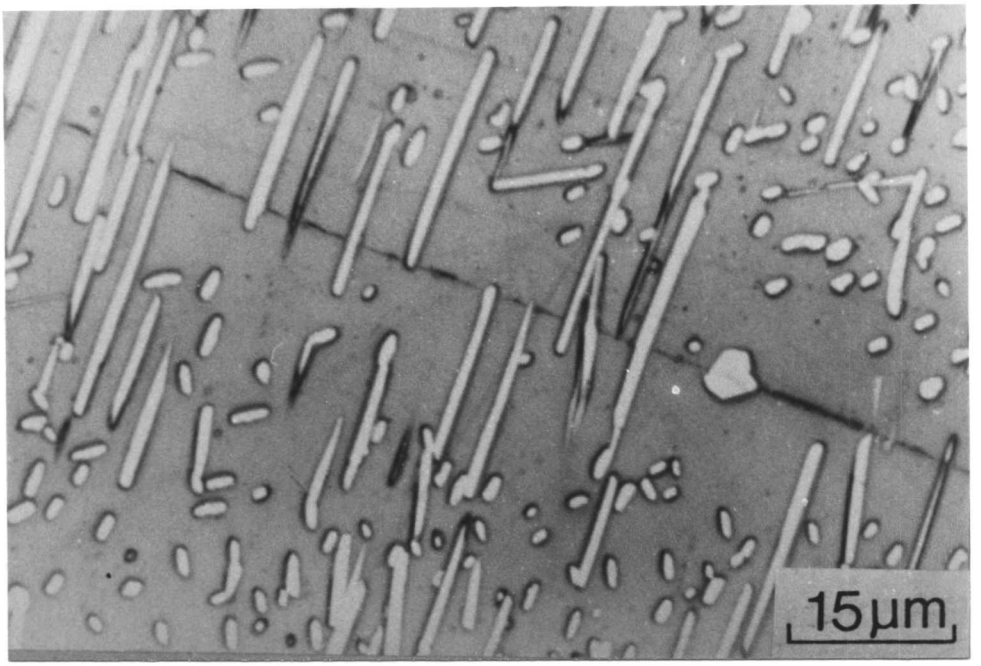

Fig. 6.44: Austenite of rod shape morphology crossing a δ-ferrite grain boundary, in alloy SH. The specimen is aged at 1000°C for 1000 seconds.

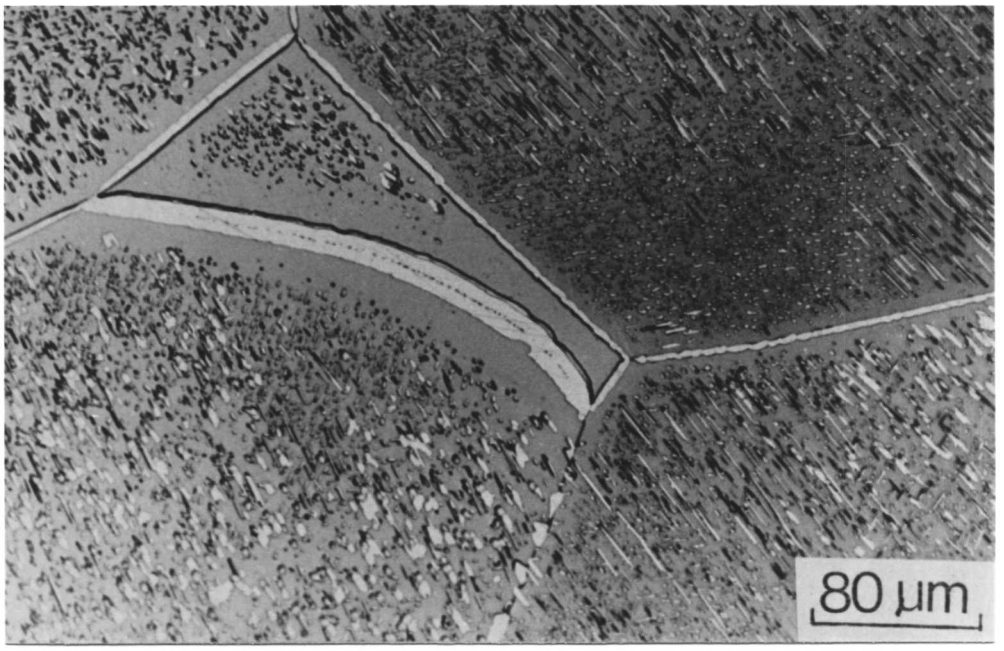

Fig. 6.45: Austenite depleted zones adjacent to δ-ferrite boundaries, in alloy SH aged at 1000°C for 1000 seconds.

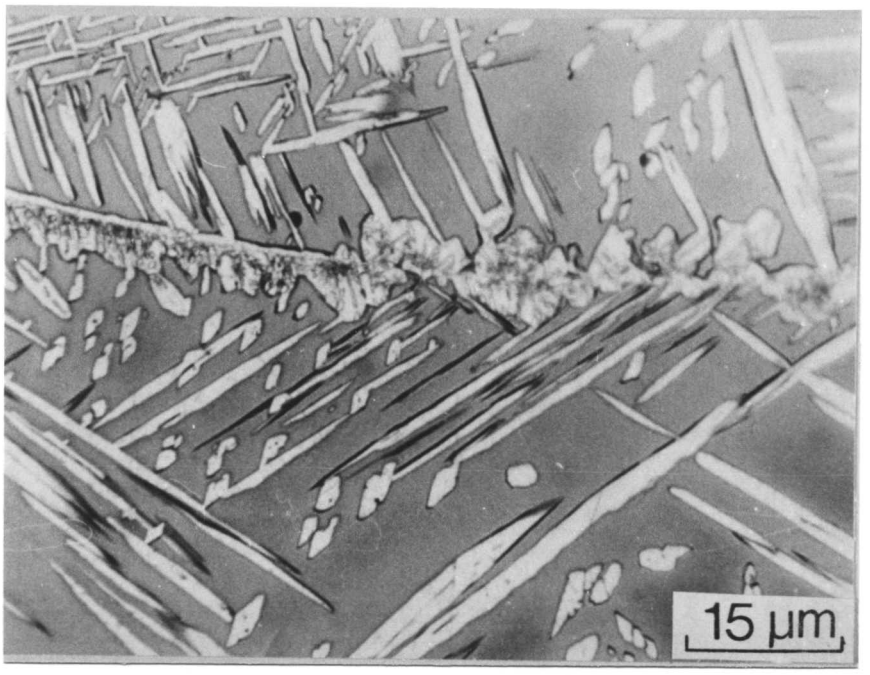

Fig. 6.46: Optical micrograph showing cellular precipitation in wrought alloy SH aged at 800°C for one hour.

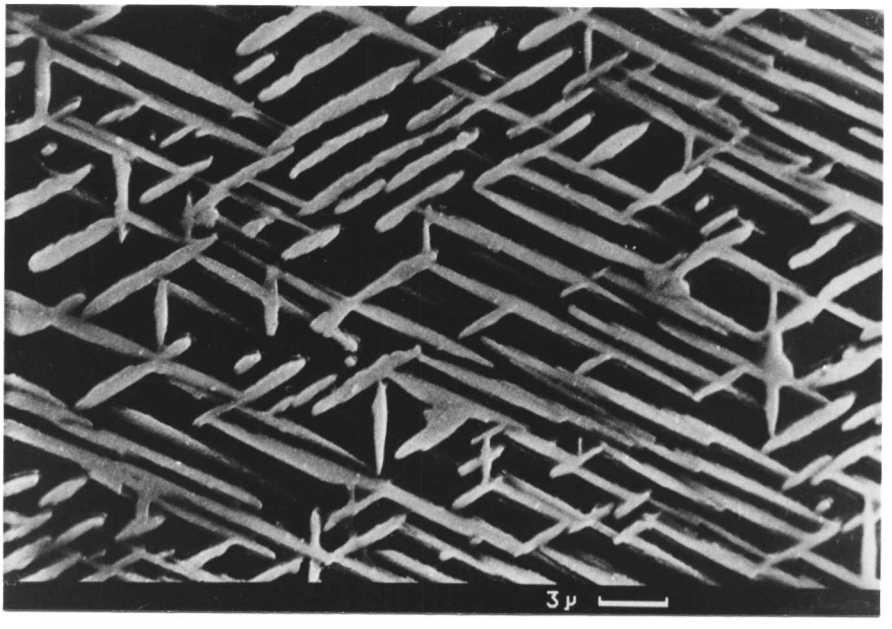

Fig. 6.47: Scanning electron image for wrought alloy SH specimen aged at 700°C for two hours. The micrograph shows the interlocking microstructure of the intragranularly nucleated acicular austenite, exhibiting well defined crystallographic orientations.

Ageing at 700 °C

The ageing behaviour at this temperature was studied for only the 630 μm δ grain size. The specimen was aged for 2 hours. The microstructure obtained is shown in Fig. 6.47. Due to the coarse δ grains, the main phase observed was fine intragranular austenite plates exhibiting a unique interlocking acicular microstructure in well defined crystallographic orientations. The length of the plates was found to vary from 3 to $\approx$ 40 μm . No precipitates were observed up to 2 hours of ageing time.

6.5.4 The Ageing Behaviour of BW Weld Metal

Samples of the as-deposited weld metal were aged at 600, 800, 1000, 1200°C for 10, 100, 1000,and 10000 seconds ageing time periods. The hardness measurements as carried out on the aged microstructures are plotted against time in Fig. 6.48. They show that at 600°C, a slight increase in hardness occurs after ageing for 10000 seconds, but otherwise the hardness remained constant with time at the ageing temperature. This was confirmed by the microstructure, which did not show substantial changes in austenite content Fig. 6.49. The reason for the increase of hardness is not clear.

At 800°C a slight increase in hardness was observed for the specimen aged for 10 seconds, with subsequent decrease with prolonged annealing. The slight increase is believed to be an effect of very fine precipitation of austenite occurring at the early stages of aging. The subsequent gradual decrease of hardness with ageing time is associated with the growth of the relatively softer γ phase (Fig. 6.50).

At 1000°C and as a result of the expected faster growth rate of austenite compared with that at 800°C, a sudden decrease in hardness was observed for the 10 second ageing time Fig. 6.51. With increasing ageing time a steep increase in hardness was observed which is believed to have happened as a consequence of the precipitation of the hard σ phase (Fig. 6.52).

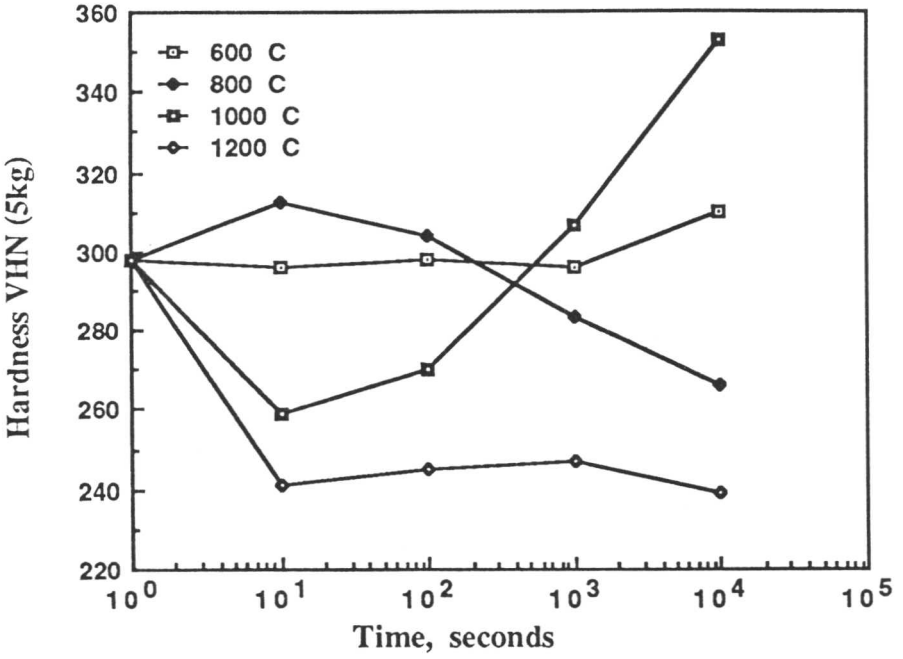

Fig. 6.48: Hardness profiles at different ageing temperatures as a function of ageing time, as measured in the as-deposited region (top bead) of weld BW.

Ageing at 1200°C, for 10 seconds, was associated with a sudden decrease of hardness which is believed to occur as a result of the fast growth of austenite towards its equilibrium volume fraction Fig. 6.53. The hardness was more or less constant for longer ageing times.

The hardness data as a function of aging time and temperature for alloy BW, aged from the as-received welded condition are shown in Fig. 6.54. At 600°C, a decrease in the average hardness values was observed after 10 seconds which stayed constant up to 1000 seconds and then slightly increased at 10000 seconds ageing time. This may be a result of the faster formation of austenite in the reheated zones when compared with the as-deposited samples since no nucleation is required. At 1000°C, the increase in hardness after 100 seconds ageing time was steeper when compared with the as-deposited regions. This could be a consequence of the availability of more nucleation sites for σ phase formation in the reheated zone, as it is believed that the preferred nucleation sites for σ are the δ/γ boundaries.

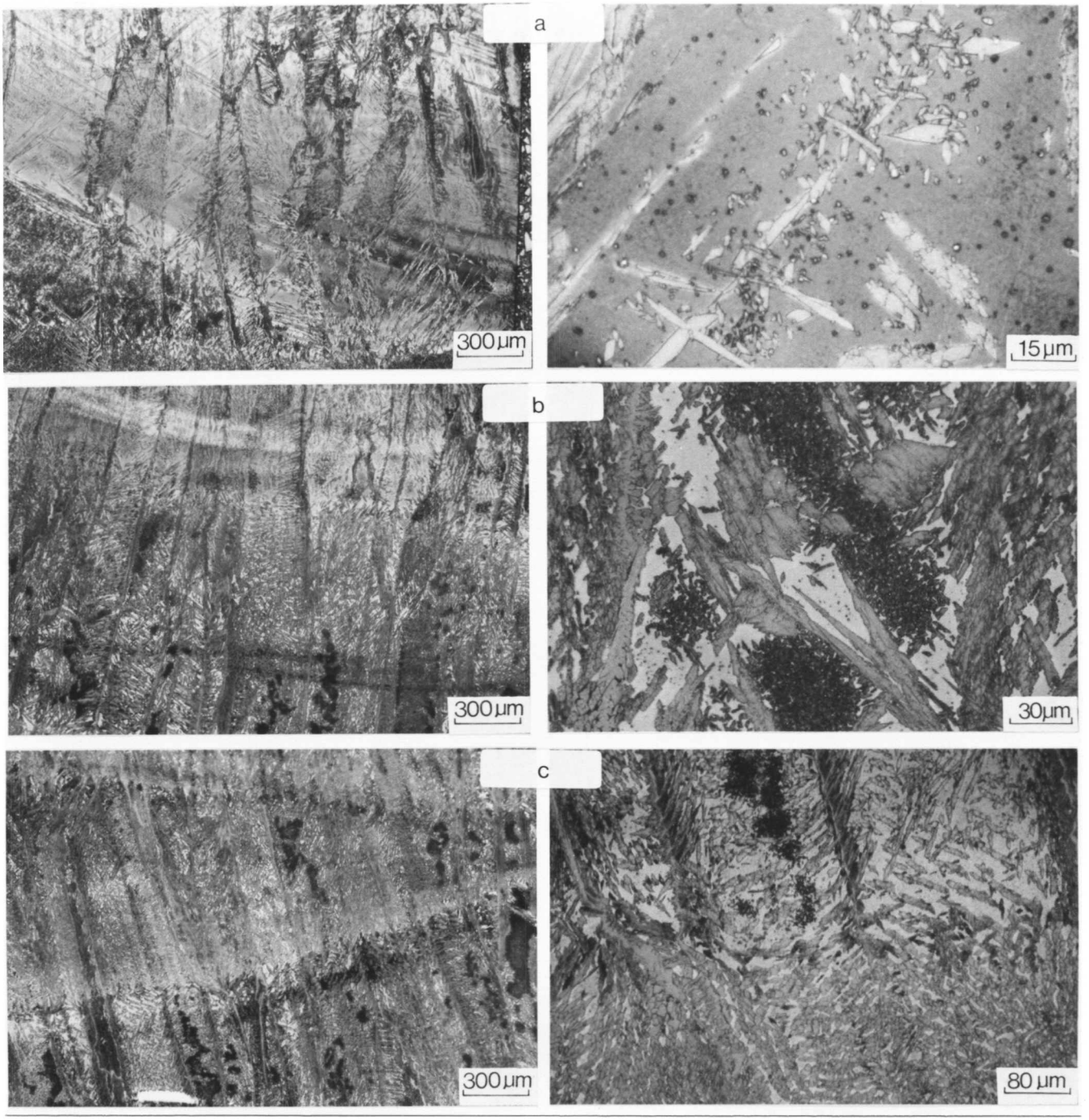

Fig. 6.49: Optical micrographs showing the microstructure of weld alloy BW aged from the as-received weld condition at 600°C:

(a) As-received, (b) aged for 10 seconds, (c) aged for 100 seconds.

(continued overleaf)

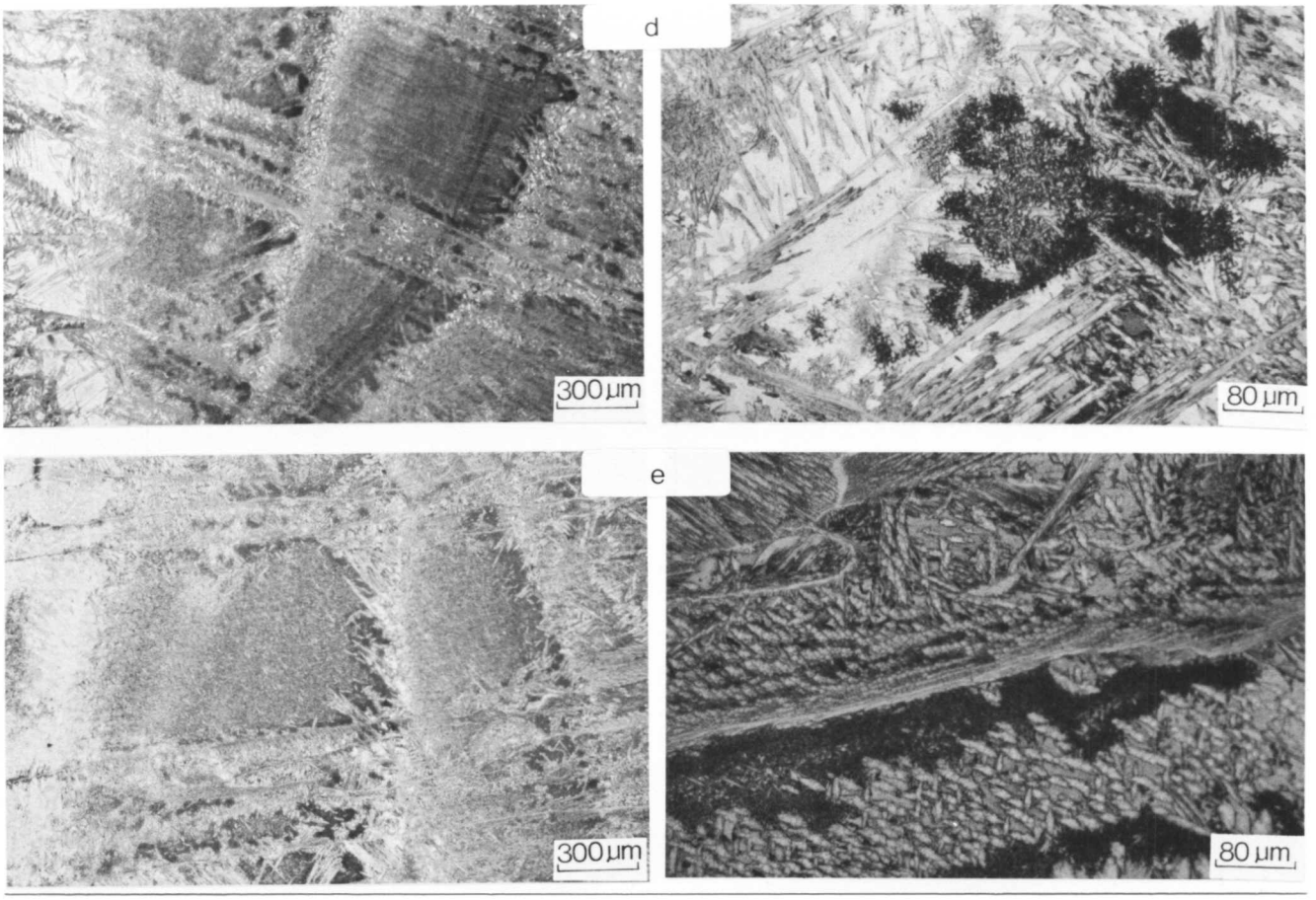

Fig. 6.49: continued:

(d) Aged for 1000 seconds, (e) aged for 10000 seconds.

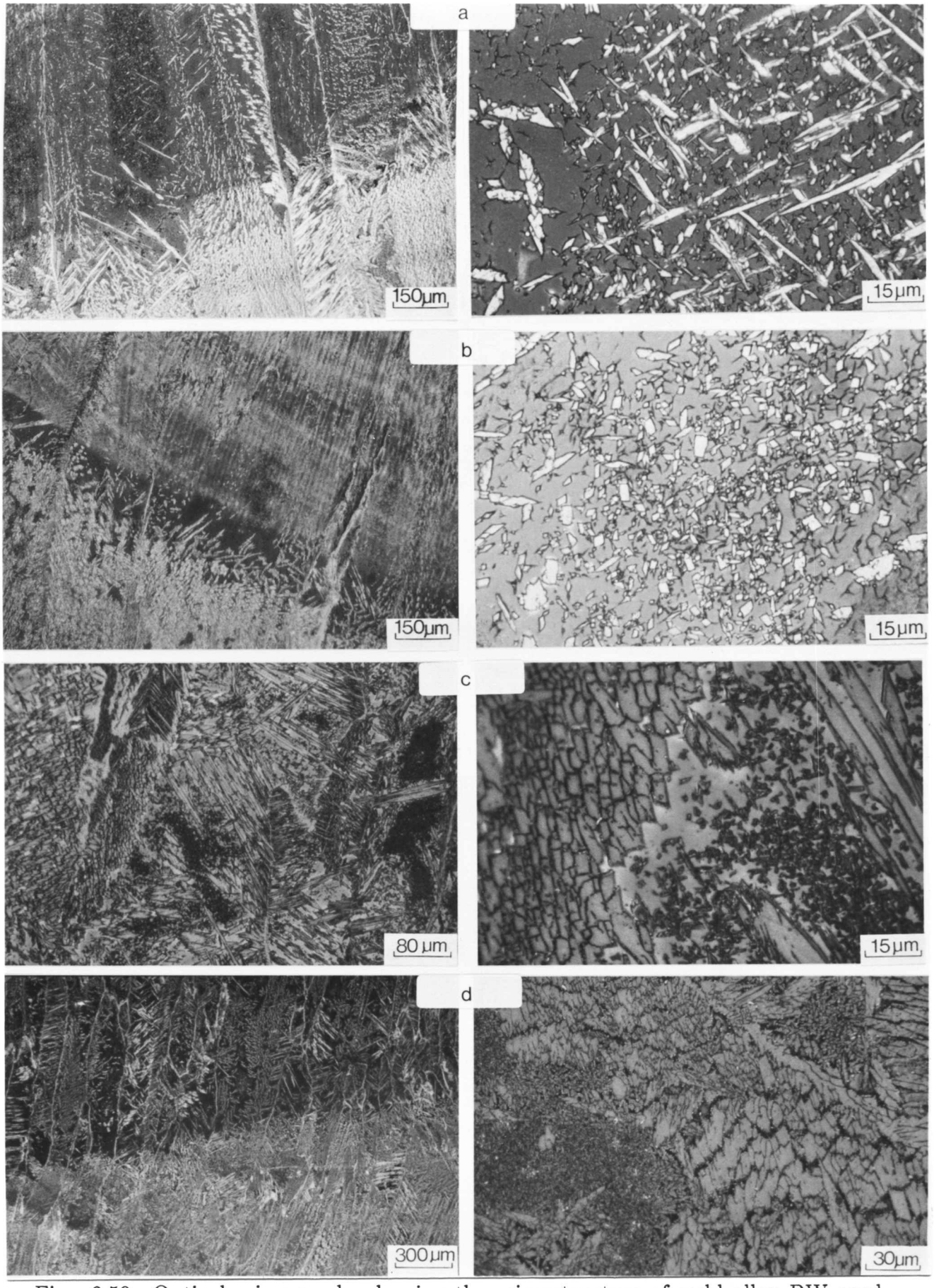

Fig. 6.50: Optical micrographs showing the microstructure of weld alloy BW aged from the as-received weld condition at 800°C: (a) Aged for 10 seconds, (b) aged for 100 seconds, (c) aged for 1000 seconds and (d) aged for 10000 seconds. In a, b and d the light etching phase is austenite. In c the yellowish phase is δ. In d δ is blue and the very fine white particles are σ.

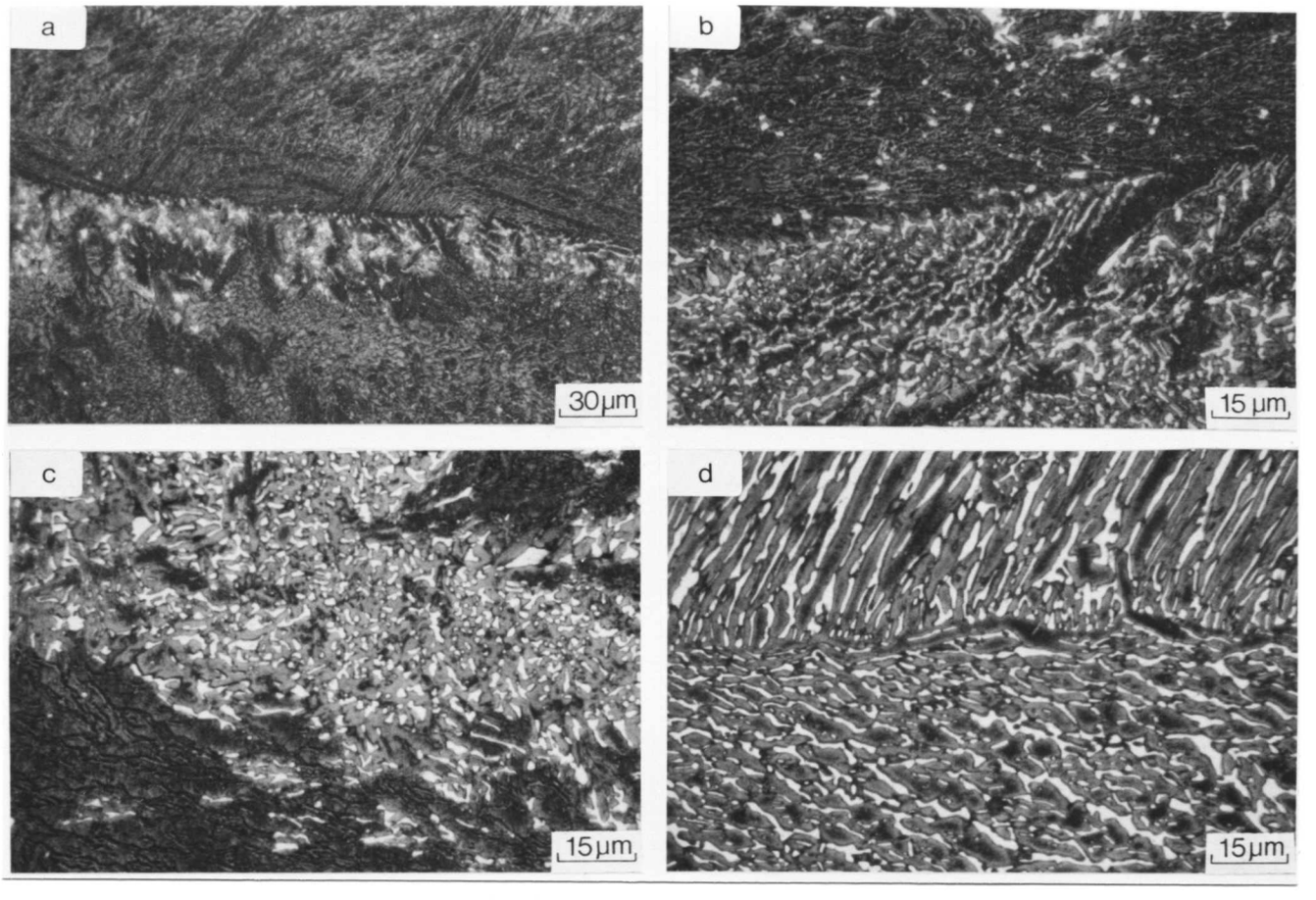

Fig. 6.51: Optical micrographs showing the microstructure of weld alloy BW aged from the as-received weld condition at 1000°C: (a) Aged for 10 seconds, (b) aged for 100 second, (c) aged for 1000 seconds, and (d) aged for 10000 seconds. The blue phase is austenite and the white phase is σ.

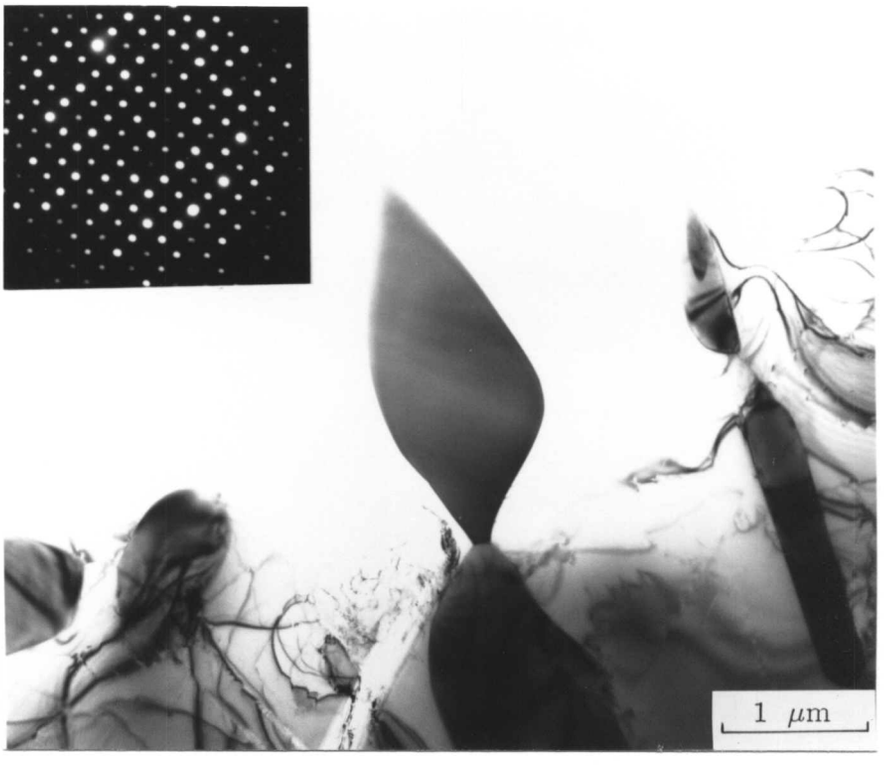

Fig. 6.52: TEM bright field image for weld metal BW aged from the as-received weld condition at 1000°C for 1000 seconds. The micrograph shows a sigma phase particle and its corresponding electron diffraction pattern. Zone axis $[001]_\sigma$.

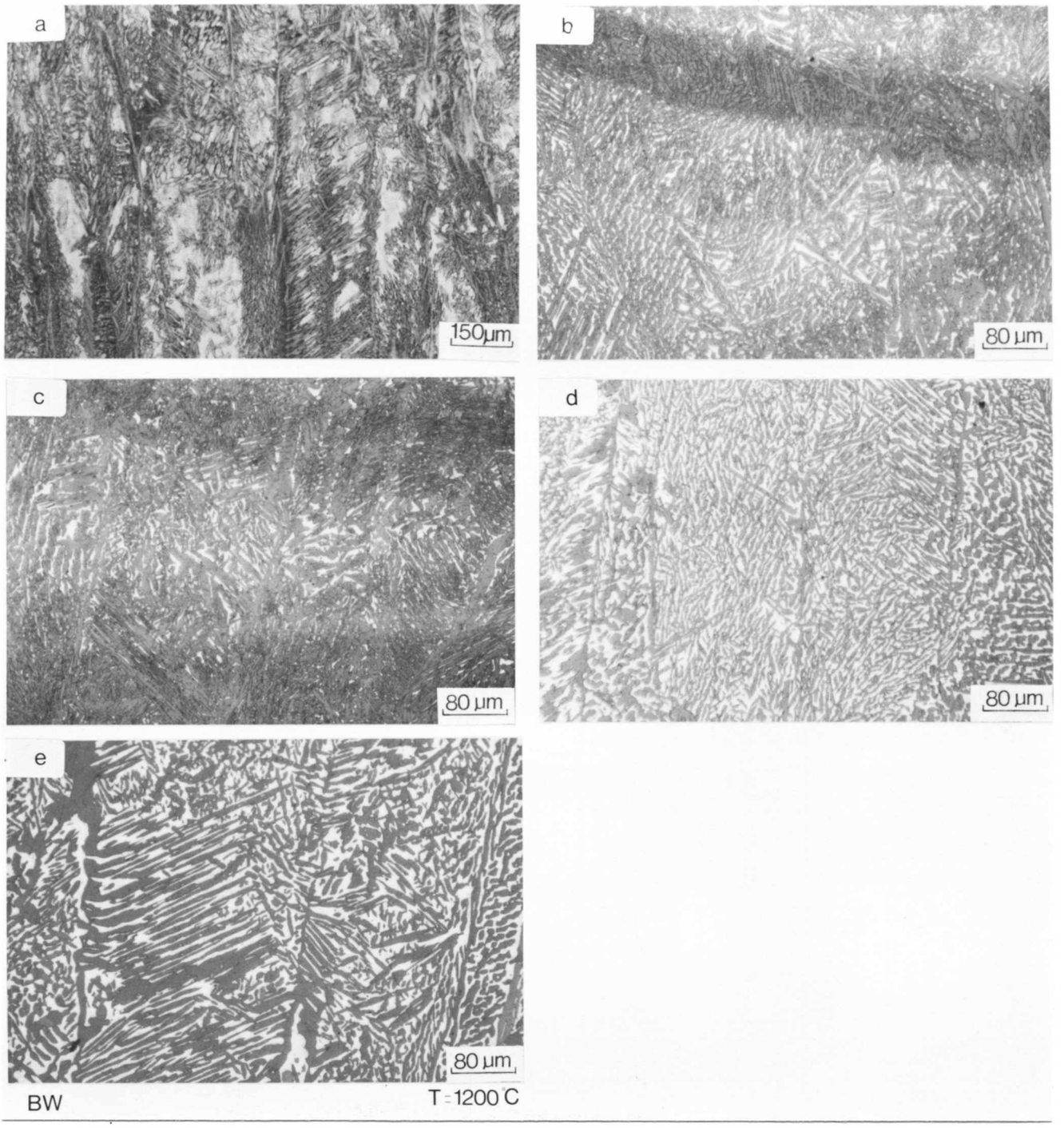

Fig. 6.53: Optical micrographs showing the microstructure of weld alloy BW aged from the as-received weld condition at 1200°C: (a) As-welded, (b) aged for 10 seconds, (c) aged for 100 seconds, (d) aged for 1000 seconds, and (e) aged for 10000 seconds. δ-ferrite is the bluish etching phase in (a) while it is the light etching phase in b, c, d, and e.

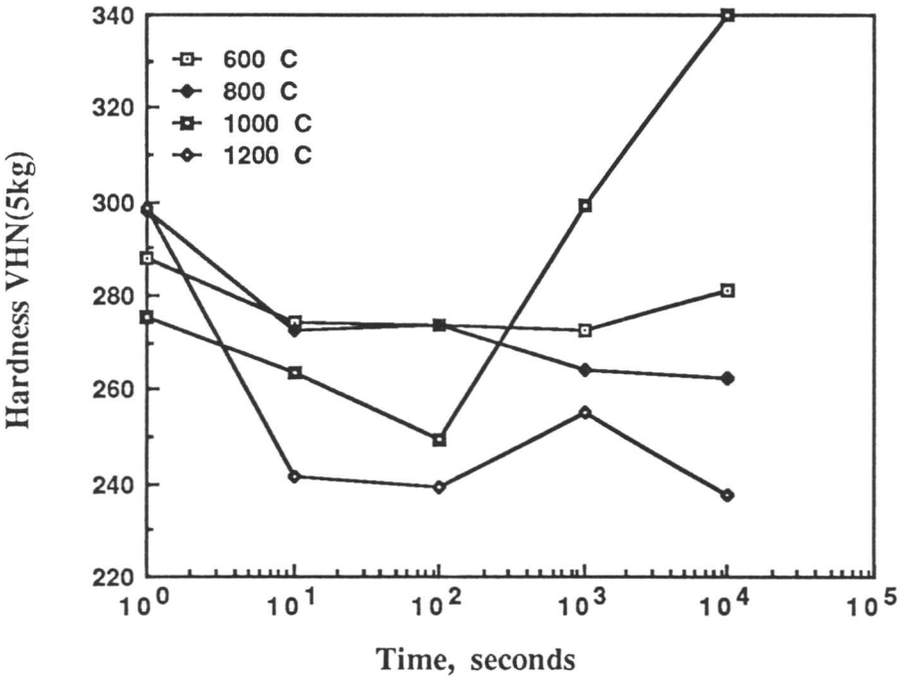

Fig. 6.54: Profiles of the average measured hardness for different ageing temperatures as a function of ageing time recorded for weld metal BW aged from the as-received weld condition.

6.6 Direct Isothermal Transformation of Alloy SH

Ferritised samples were cooled rapidly to the isothermal transformation temperature, which contrast with the reaction of retained δ by reheating to the isothermal transformation temperature. The experiments were conducted using resistance furnaces, the aim being to compare with the dilatometric technique. Experimental details and the results of austenite volume fraction determinations, using the linear intercept method, image analysis and X-ray method are shown in Table 6.7:

Table 6.7.a: Direct isothermal transformation of wrought alloy SH; experimental data and measured volume fraction of austenite V_γ.

$t_{T_{iso}}$ (min)	1	1	10	10	30	30	60	60
T_{iso}(°C)	V_γ^{LI}	V_γ^{SS}	V_γ^{LI}	V_γ^{SS}	V_γ^{LI}	V_γ^{SS}	V_γ^{LI}	V_γ^{SS}
700	0.06	0.08	0.07	0.12	0.13	0.14	0.15	0.18
800	0.09	0.11	0.11	0.15	0.22	0.26	0.27	0.34
900	0.15	0.16	0.25	0.32	0.32	0.37	0.35	0.39
1000	0.17	0.2	0.27	0.35	0.27	0.33	0.29	0.35

$T_\delta = 1320°C$, LI = lineal intercept and SS = Seescan image analysis.

Table 6.7.b: Measurements of austenite volume fraction at 900°C by X-ray diffraction [20].

Time (min)	1	10	30
$V_\gamma^{Diffraction}$	0.14	0.23	0.3
V_γ^{LI}	0.15	0.25	0.32

Table 6.7.c: δ-ferrite grain size (D_δ^*)as measured by lineal intercept method in μm.

Time at T_{iso} (min)	1	10	30	60
700°C	620	620	650	796
800°C	515	435	623	510
900°C	620	420	518	542
1000°C	460	691	625	625

The equilibrium volume fraction of austenite was achieved (Table 6.7) after transformation at 900°C and 1000° somewhere between 1 - 10 minutes. The early stages of the δ-ferrite to austenite transformation could not be detected. This shows the limitations of the conventional techniques as a result of the rapid kinetics of $\delta \rightarrow \gamma$ transformation and it could also be the case that some transformation occurred during cooling from the ferritisation temperature to the isothermal temperature, because of the effect of the quartz capsule in reducing the rate of heat dissipation. For the isothermal temperatures 700 and 800°C equilibrium volume fractions of austenite were not achieved after one hour at temperature.

The microstructures of the isothermally transformed alloy SH at 900 and 1000°C are shown in Figs. 6.55 & 6.56. The δ-ferrite boundaries were rapidly decorated by continuous layers of allotriomorphic austenite. Secondary Widmanstätten plates grew from the allotriomorphs, and some austenite plates nucleated intragranularly on inclusions. With increasing reaction time, the latter morphology became more prominent although the austenite allotriomorphs continued to thicken. The measured apparent maximum length of the Widmanstätten austenite plates and the rather longer intragranularly nucleated austenite plates as a function of reaction time are presented in Table 6.9. The plate lengths were found to decrease with temperature although the increase with time at each isothermal temperature was small. These data (Table 6.9) indicate that the plates initially grow rather rapidly, and the growth rate slowing down at the latter stages of growth, presumably because the austenite volume fraction approaches the equilibrium value.

Similar transformation behaviour was found at 800 and 700°C, (Figs. 6.57 & 6.58). At 700°C, the allotriomorphic austenite layers were relatively thinner and the Widmanstätten plates shorter in length compared with transformation at 800°C (Fig. 6.58).

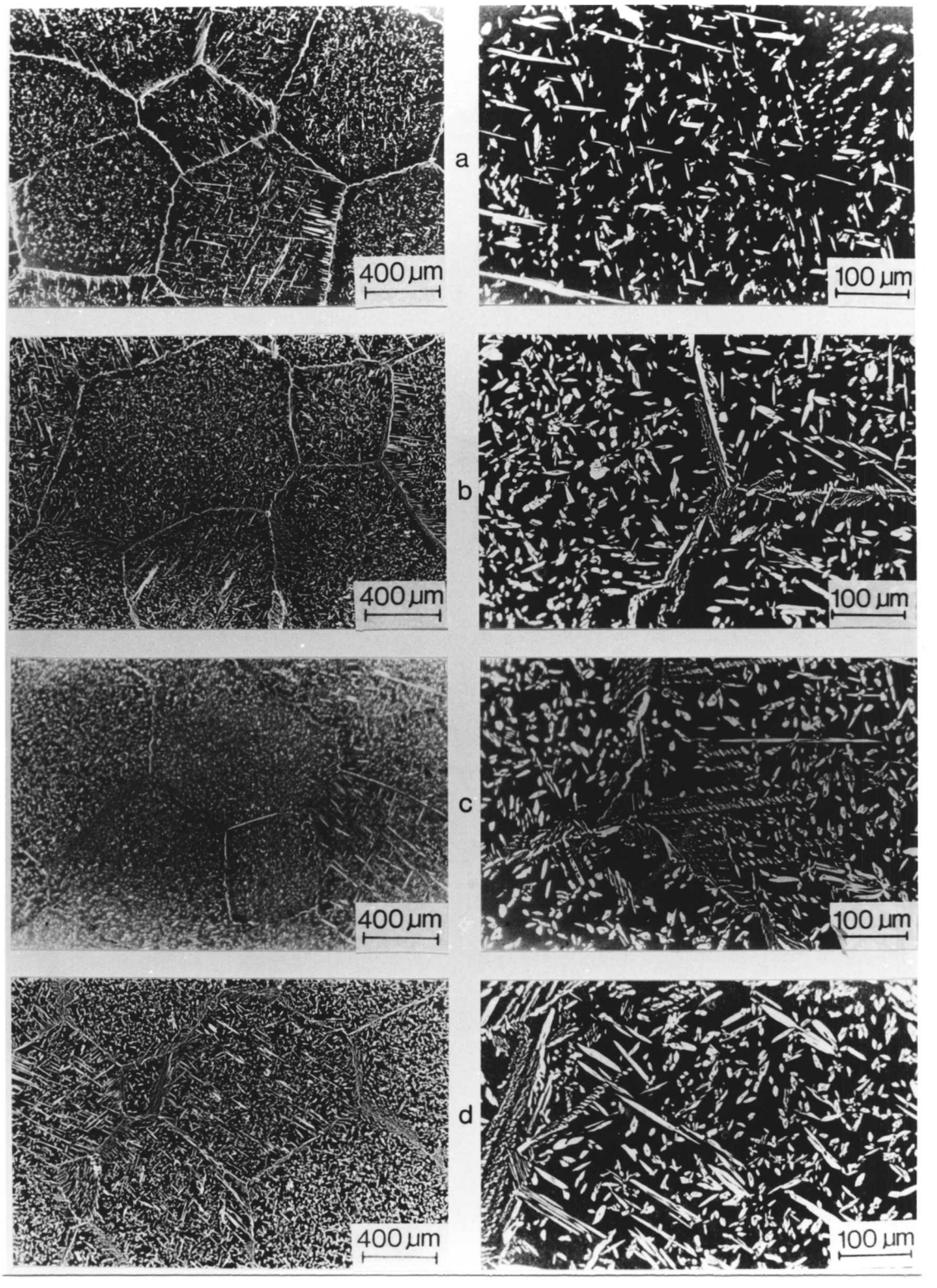

Fig. 6.55: A set of optical micrographs showing the microstructure of the directly isothermally transformed wrought alloy SH specimens at 1000°C: (*a*) For 1 minute, (*b*) for 10 minutes, (*c*) for 30 minutes, (*d*) for 60 minutes. The light etching phase is austenite.

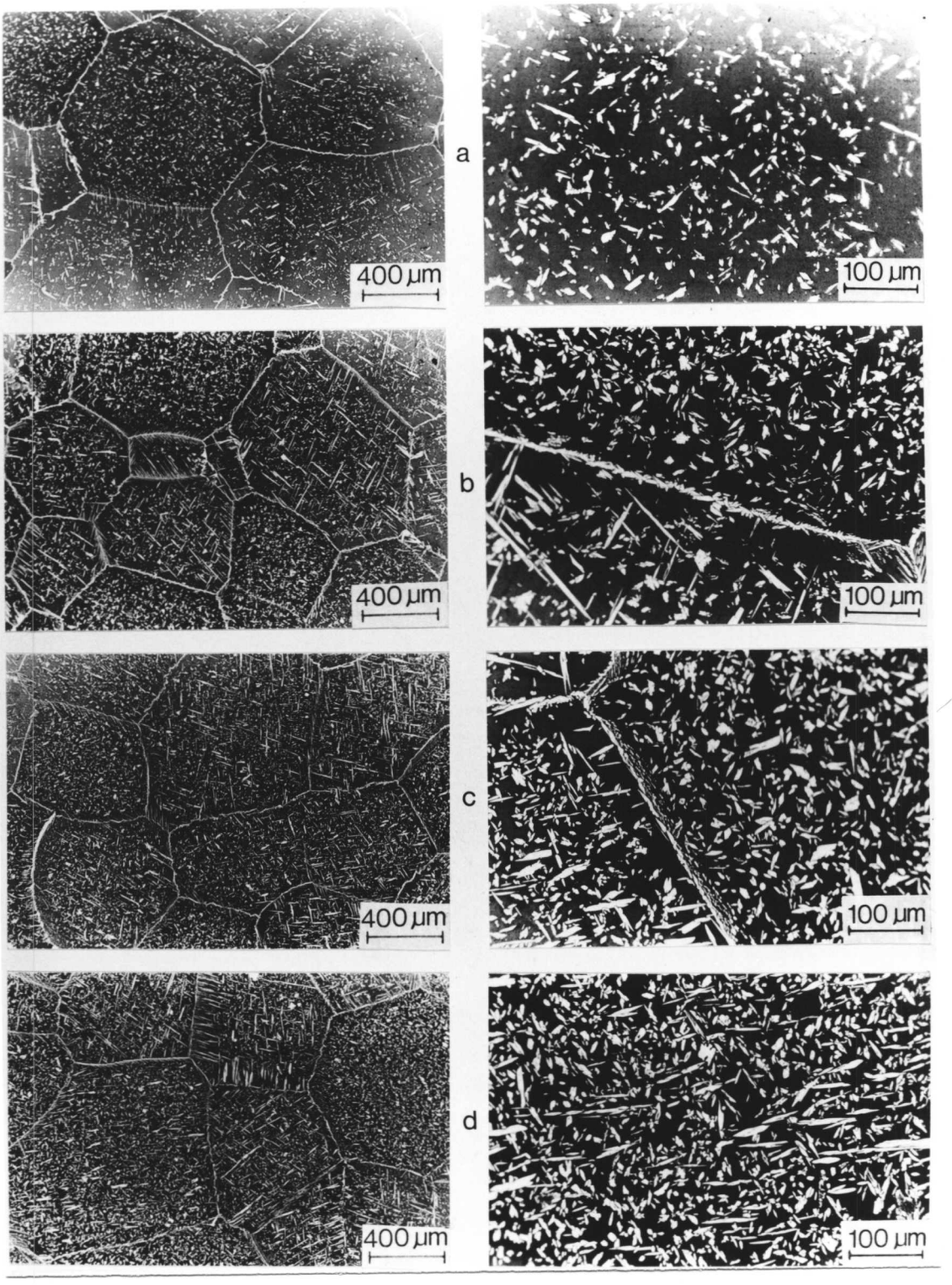

Fig. 6.56: A set of optical micrographs showing the microstructure of the directly isothermally transformed wrought alloy SH specimens at 900°C: (*a*) For 1 minute, (*b*) for 10 minutes, (*c*) for 30 minutes, (*d*) for 60 minutes. The light etching phase is austenite.

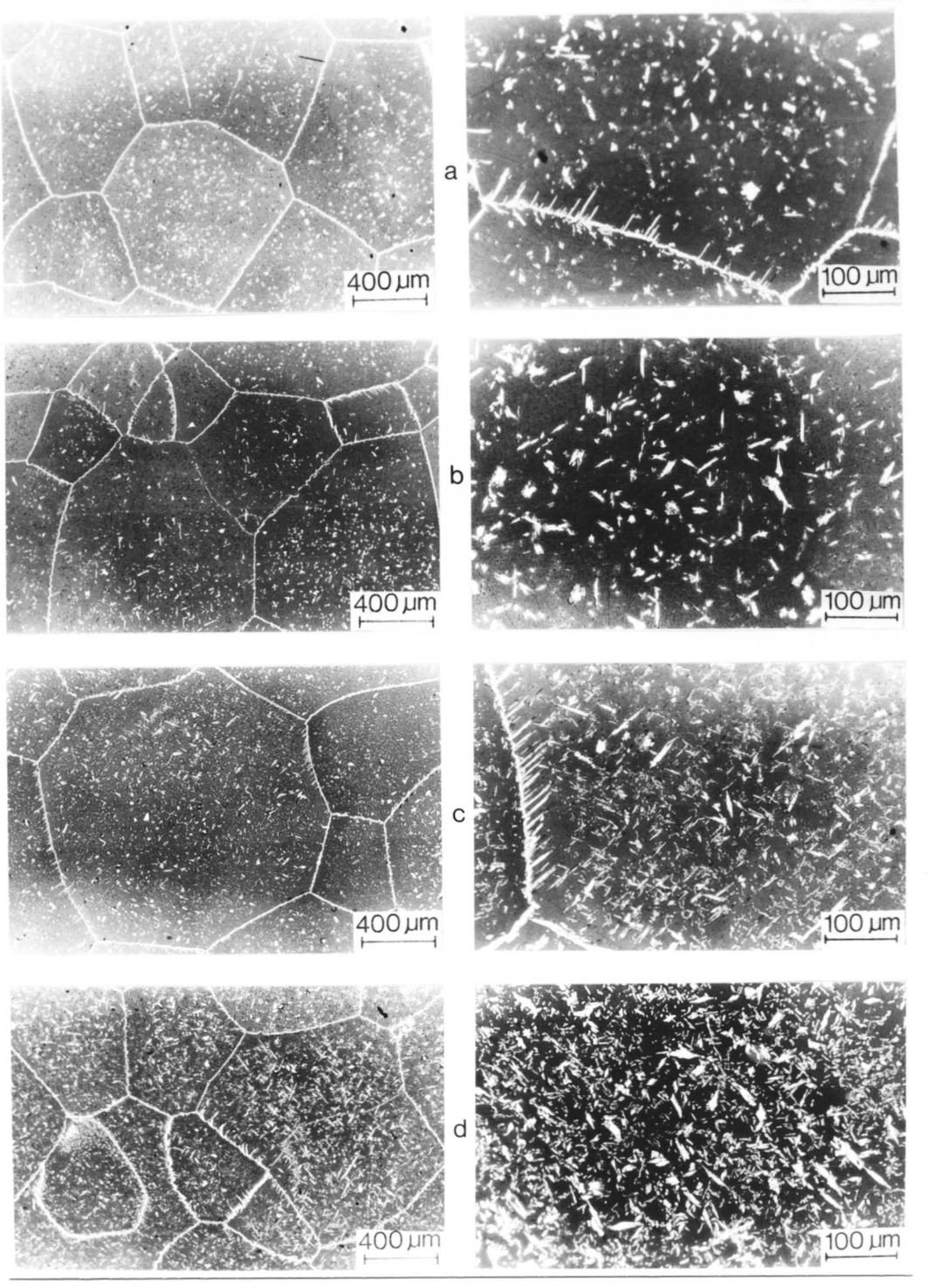

Fig. 6.57: A set of optical micrographs showing the microstructure of the directly isothermally transformed wrought alloy SH specimens at 800°C: (*a*) For 1 minute, (*b*) for 10 minutes, (*c*) for 30 minutes, (*d*) for 60 minutes. The light etching phase is austenite.

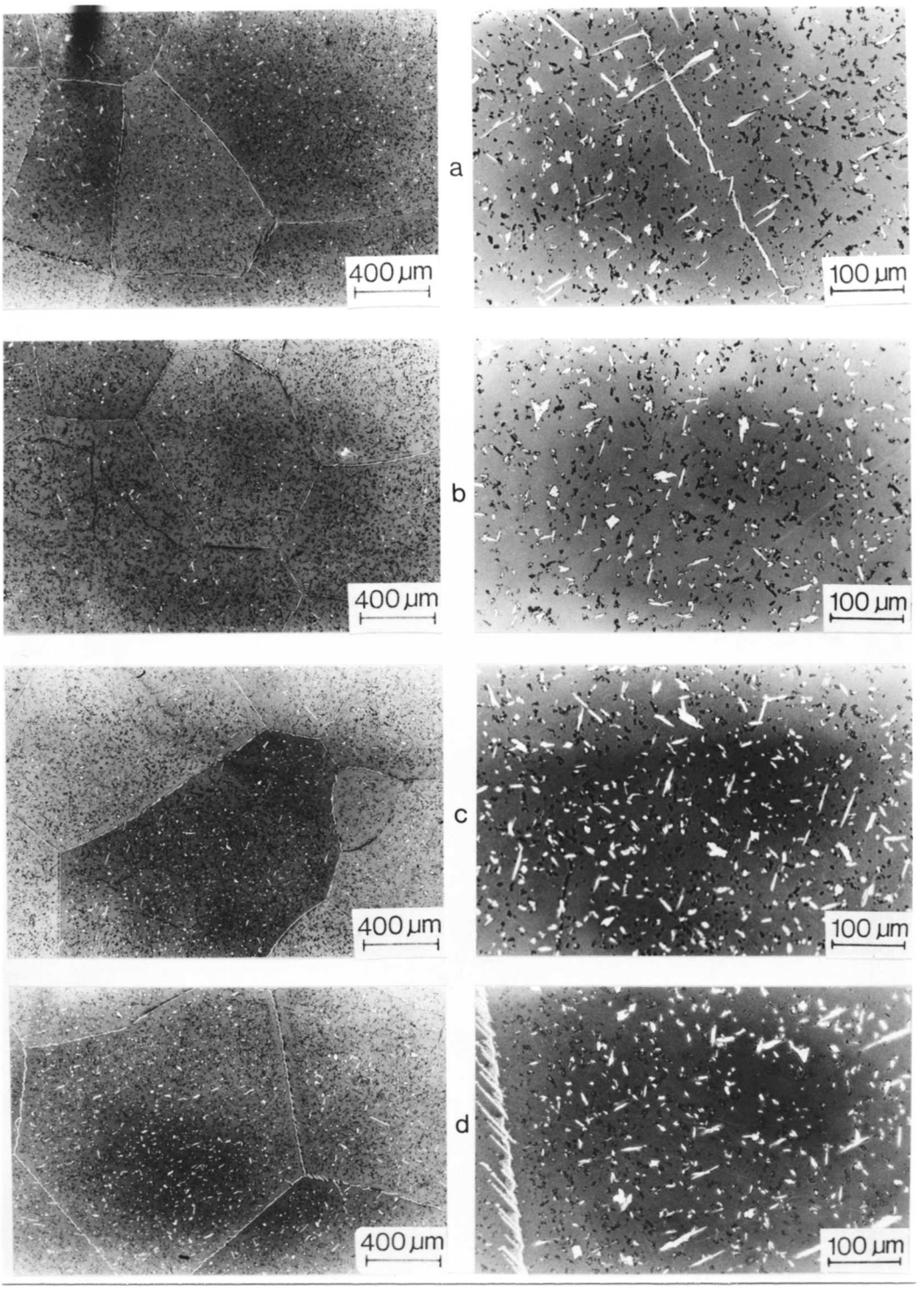

Fig. 6.58: A set of optical micrographs showing the microstructure of the directly isothermally transformed wrought alloy SH specimens at 700°C: (*a*) For 1 minute, (*b*) for 10 minutes, (*c*) for 30 minutes, (*d*) for 60 minutes. The light etching phase is austenite.

Table 6.9: Measured maximum length of secondary Widmanstätten austenite plates γ_w and intragranularly nucleated austenite γ_{intra} plates as a function of $\delta \rightarrow \gamma$ reaction time in wrought alloy SH.

Temperature (°C)	Time (s)	L_{γ_w} (μm)	$L_{\gamma_{intra}}$ (μm)
1000	60	156	195
1000	600	180	170
1000	1800	–	208
1000	3600	188	210
900	60	93	188
900	600	180	218
900	1800	92	184
900	3600	156	218
800	60	45	78
800	600	62	78
800	1800	53	94
800	3600	78	140
700	60	–	–
700	600	26	30
700	1800	31	47
700	3600	38	75

6.7 Ferritisation

6.7.1 Ferritisation Temperature

To study the transformation of $\delta \rightarrow \gamma$ starting from a fully ferritic sample, requires the knowledge of the ferritisation temperature (T_δ), referred to in the literature as the A_4 temperature. To determine the ferritisation temperatures, homogenized specimens of each alloy were sealed in quartz tubes as discussed earlier. Samples were heated at 1200, 1250, 1300, 1350°C for 5 and 15 minutes, after which the quartz tubes were quickly broken, and the specimens plunged into iced-brine. The ferritisation temperatures were found to be, for alloy SH $\approx$ 1270°C and $\approx$ 1320°C for alloys R2P and R4P. The microstructure of the as-quenched specimens is shown in (Fig. 6.59). Even after solution treatment at 1350°C for 15 minutes, small amounts of austenite persisted, but

in general $\approx$ 99 % of the microstructure was found to be ferritic.

6.7.2 Kinetics of Ferritisation

To study the ferritisation kinetics, swaged specimens of alloy SH were ferritised at 1250, 1300, 1350 and 1400°C using the dilatometer. Specimens were heated to the ferritisation temperature with the maximum heating rate achieved by the dilatometer ($500°\,C\,s^{-1}$) and quenched to the ambient temperature using a helium jet.

As expected the time required for ferritisation was found to decrease with increasing temperature Fig. 6.60. The times required for complete ferritisation at 1250, 1300 and 1335°C were respectively about 100, 70 and 40 seconds. Due to creep problems it was not possible to detect the time required to complete ferritisation at 1400°C. The time would be expected to be less than that for 1335°C, *i.e.* less than 40 seconds. The ferritisation times are approximate, since some transformation was found to occur (Fig. 6.61) during heating to T_δ even at the highest heating rate used.

6.7.3 The Effect of the Retained Austenite

Experiments on the effect of the austenite retained when the solution treatment (ferritisation) is carried out in the two phase field ($\delta+\gamma$), on the subsequent isothermal transformation of δ to γ are reported here.

The previously solution treated specimens (1150°C for 62 hrs) were heated in the ($\delta+\gamma$) phase field for 5 mins at about 1250°C and brought down to the required isothermal temperature using a dilatometer. After 15 minutes at temperature, the specimens were helium quenched to ambient temperature. Austenite was found to grow from the retained austenite on the δ/δ boundaries Fig. 6.62, in addition to Widmanstätten side plates and intragranular austenite of irregular morphology, σ phase precipitates were observed on the δ/γ boundaries of both retained and mature intragranular austenite. This implies that the formation of σ starts after the $\delta \rightarrow \gamma$ transformation has progressed substantially.

Since the need to nucleate austenite is removed, the kinetics of austenite formation were relatively rapid, as indicated by the lack of incubation periods during isothermal reactions Fig. 6.63.

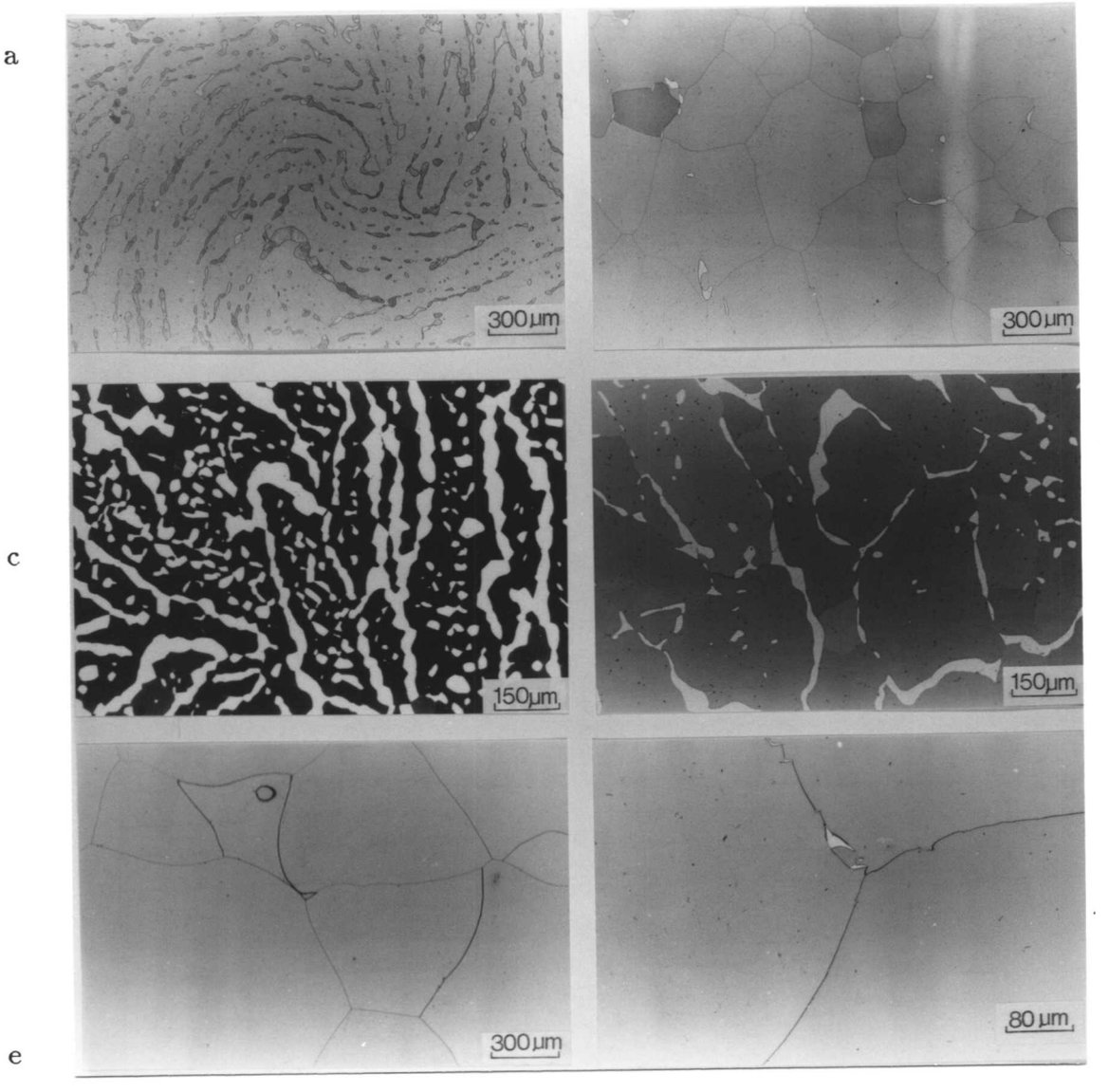

Fig. 6.59: Optical micrographs showing the microstructure of wrought alloys SH, R2P, and R4P after quenching from the ferritisation temperatures into iced-brine: (a) R2P solution treated (ST) at 1250°C for 10 min, (b) R2P ST at 1300°C for 5 min, (c) R4P ST at 1200°C for 10 min, (d) R4P ST at 1300°C for 5 min and (e) SH ST at 1300°C for 10 min.

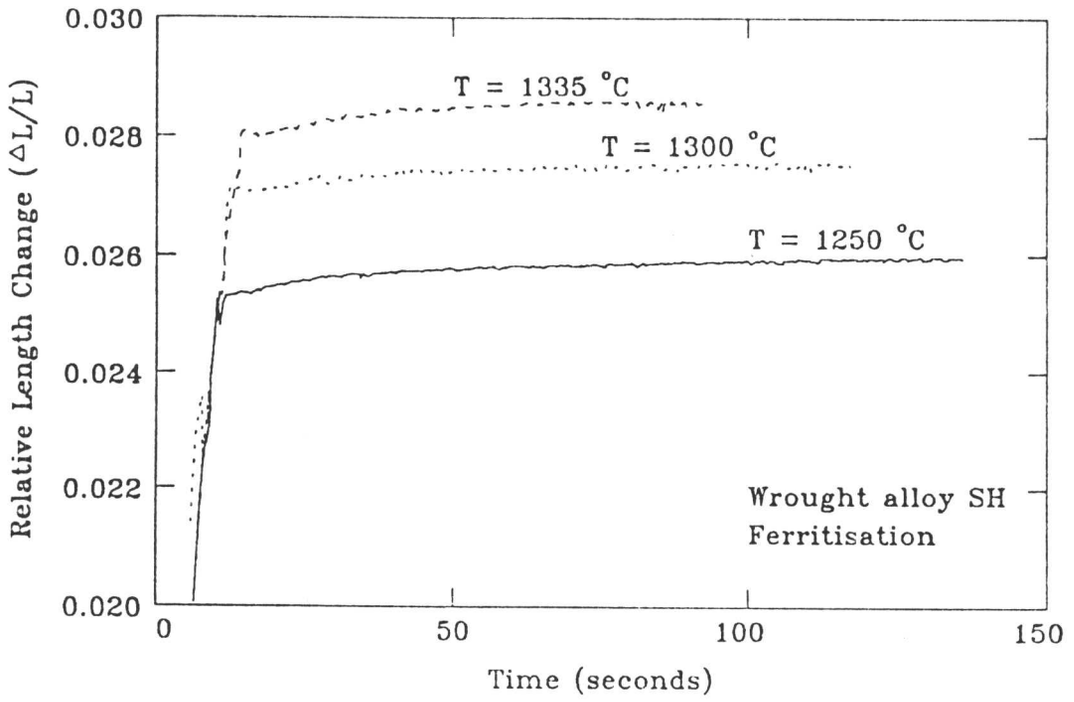

Fig. 6.60: Relative length versus time profiles recorded for wrought alloy SH specimens during isothermal ferritisation.

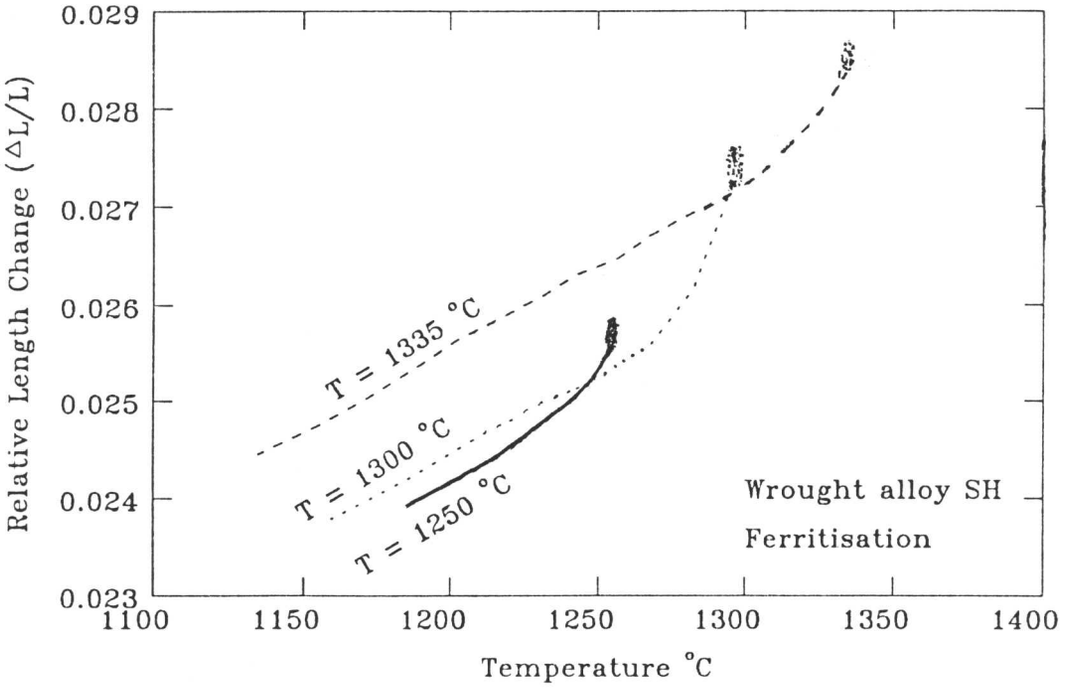

Fig 6.61: Relative length versus temperature profiles recorded for wrought alloy SH specimens during isothermal ferritisation.

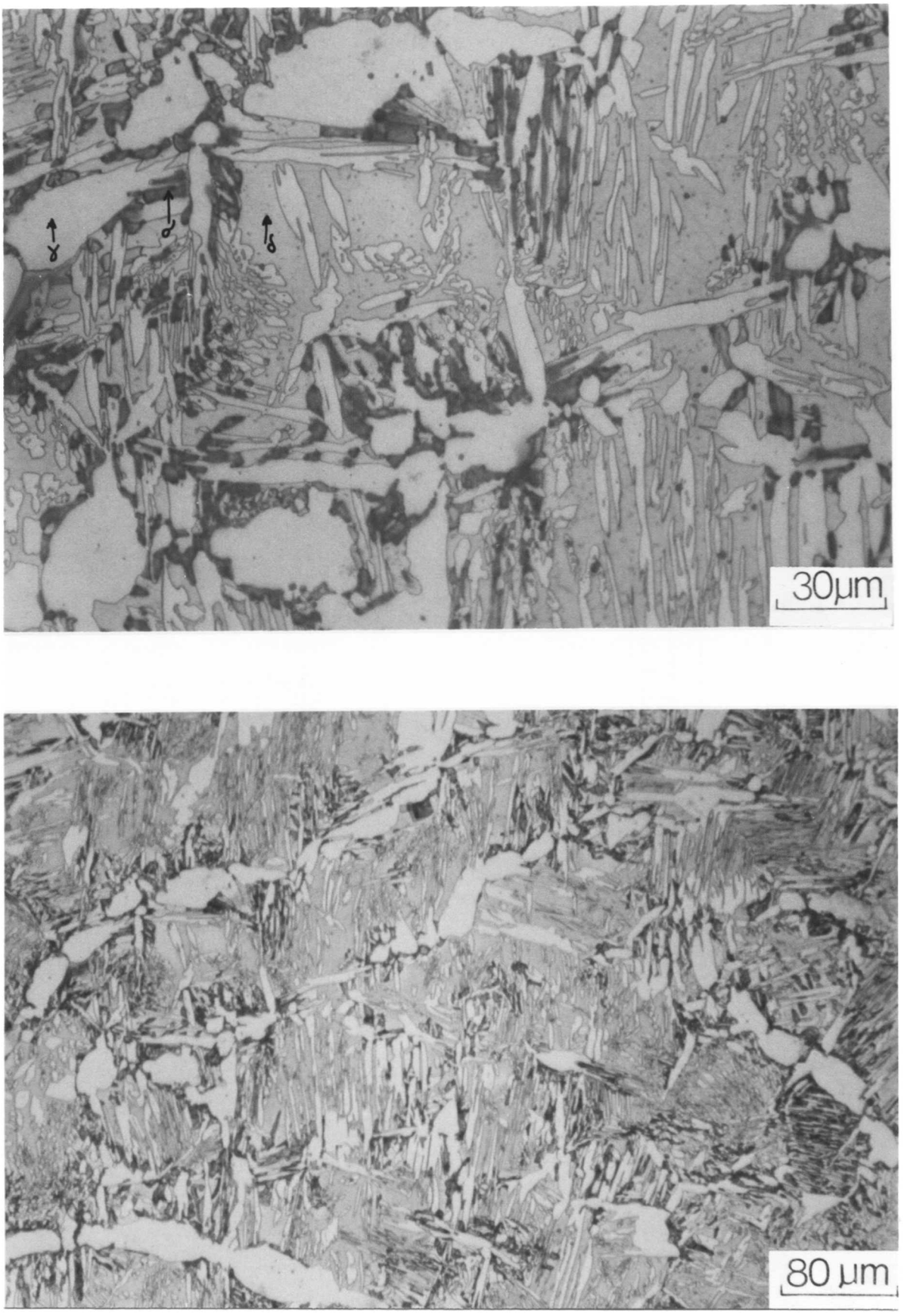

Fig. 6.62: Microstructure of a sample of alloy R4P, after direct isothermal transformation from the $\delta + \gamma$ phase field at 900°C for 15 minutes.

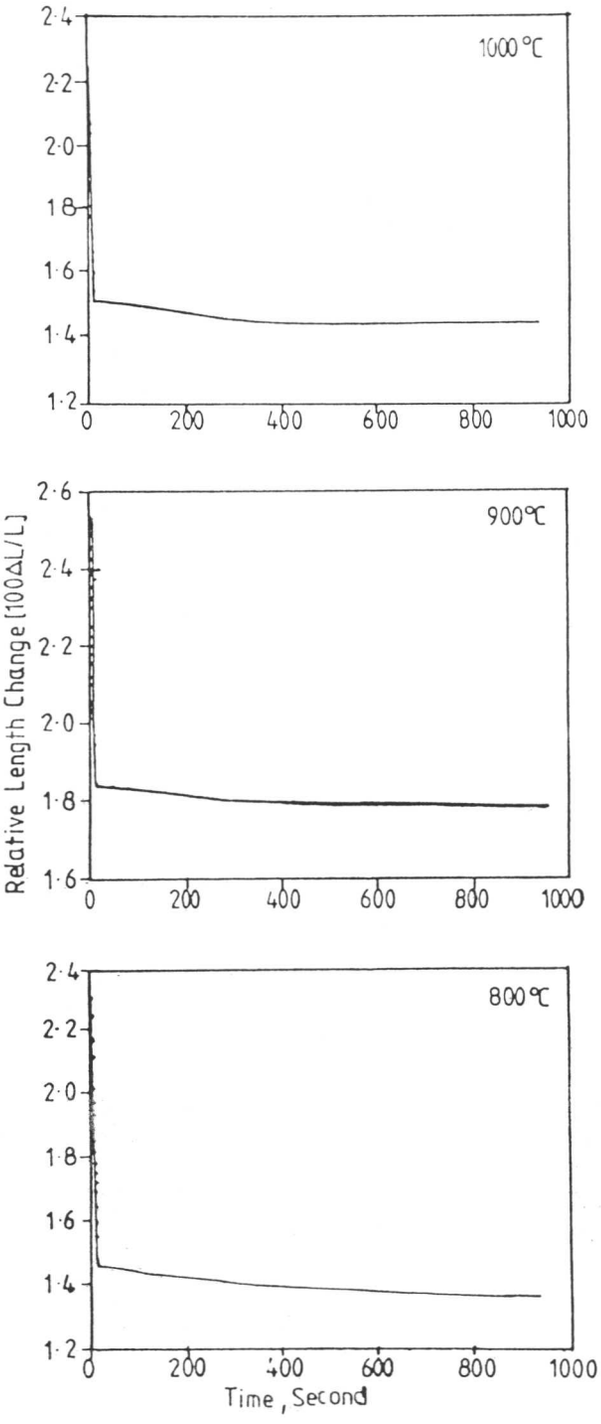

Fig 6.63: Relative length versus time profiles recorded for wrought alloy R4P isothermally transformed at 1000, 900 and 800°C. The specimens were solution treated in the $\delta + \gamma$ phase field to study the effect of the austenite retained at the solution treatment temperature on the subsequent $\delta \rightarrow \gamma$ transformation.

6.8 The Mechanism of $\delta \rightarrow \gamma$ Transformation

The mechanism of $\delta \rightarrow \gamma$ solid state transformation is as yet in dispute. While some authors believed that it is reconstructive, others suggest a displacive transformation mechanism for particular morphologies. It has been suggested [21,22] that in welding, as a consequence of the cooling rates involved, the transformation is better classified as a diffusionless massive transformation. The microsegregation observed at room temperature is explained to be due to the liquid to solid transformation. On the other hand, investigations in alloys with a ferritic solidification mode, using an electron microprobe to analyse the solute concentrations in samples quenched from different temperatures below the solidus line, suggest [23] a reconstructive transformation mechanism based on the austenite being enriched in nickel and depleted in chromium and molybdenum, and vice-versa with the δ-ferrite. Similar results, obtained using STEM microanalysis, were also reported [24] in weld metal. Using optical and transmission electron microscopy, Southwick 1979 [25], suggested a mechanism for the austenite plates forming at high temperatures, to be intermediate between a ledge and volume diffusion controlled growth mode in wrought duplex stainless steel SH. Recently, Solyu 1988 [26], who investigated duplex alloys with higher chromium and copper contents, suggested a reconstructive transformation mechanism for all the morphologies of austenite which form above 700°C, based on the observation of ledges on some of the δ/γ planar interfaces. These planar interfaces were observed to be approximately parallel to $(111)_\gamma//(110)_\alpha$ and without any resolvable dislocation arrays. Some investigators believe [27] that the transformation is consistent with that controlled by the diffusion rate of nitrogen in the δ-ferrite.

In the lower transformation temperature range, there is general agreement that the austenite grows from the δ-ferrite by a displacive mechanism, and that no compositional differences are observed between the parent and the product phases, the orientation relationship observed with the ferrite being close to Nishayama-Wasserman (N-W). According to Solyu [24], the precipitation of copper and Cr_2N particles in a deformed ferritic microstructure is effective in suppressing the subsequent formation of the austenite by a displacive mechanism.

Microanalysis results of samples taken from the as-welded region of the weld deposits have not, in the present work, been found to show significant partitioning of the substitutional solutes (chapter 5), and consistent with a displacive mechanism which could allow the diffusion of interstitials. The surface relief experiments did not estab-

lish an IPS surface relief on all of the austenite particles observed (Fig. 6.64.). In the isothermally transformed alloy R4P specimen, microanalysis surveys across the acicular and Widmanstätten austenite plates, revealed some gradient in Ni, Cr, and Mo with the distant from the tip of the plate (Fig. 6.65). In alloy W111, the thick allotriomorphs of austenite were found to have similar composition to the δ, which could be consistent with paraequilibrium or massive reaction, while the Widmanstätten and acicular austenite were associated with partitioning of the substitutional alloying elements, suggesting a reconstructive mechanism of transformation. Another result supporting this is that the nickel and iron concentrations in austenite were found to increase with reaction time in the isothermally transformed alloy SH (Fig. 6.66). During ageing of alloy SH the austenite of rod morphology was observed to cross the grain boundaries, providing strong evidence of a reconstructive transformation mechanism.

The difficulties in establishing a clear understanding of the mechanisms by which austenite forms in weld metals may be summarised as follows:

(i) The overlap between the segregation occurring during solidification and partitioning of alloying elements in the subsequent solid state transformation makes the interpretation of microanalysis data problematic.

(ii) The existence of more than one austenite morphology, the overlap in the temperature range at which these morphologies occur also confuses the interpretation.

(a)

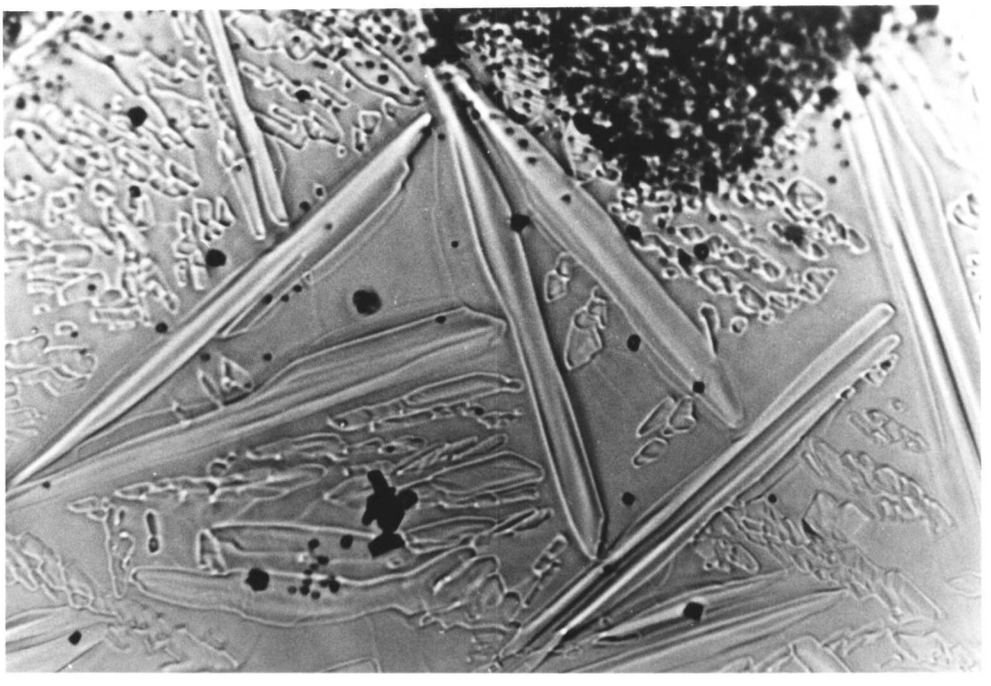

(b)

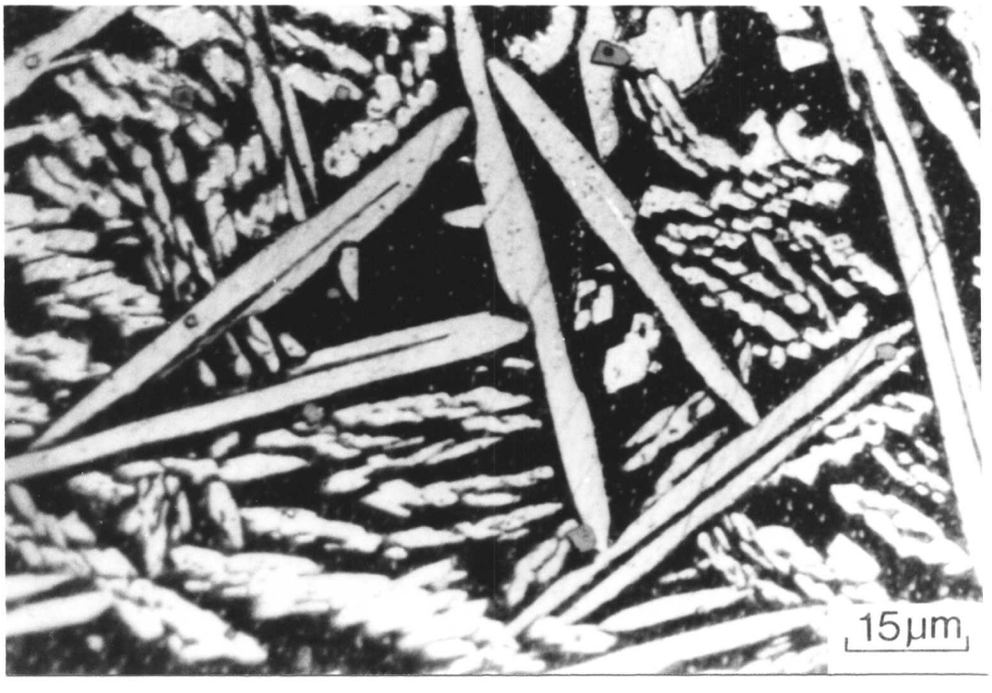

Fig. 6.64: Surface relief associated with sample of alloy R4P after isothermal transformation at 1000°C (a) and its corresponding microstructure after polishing and etching (b).

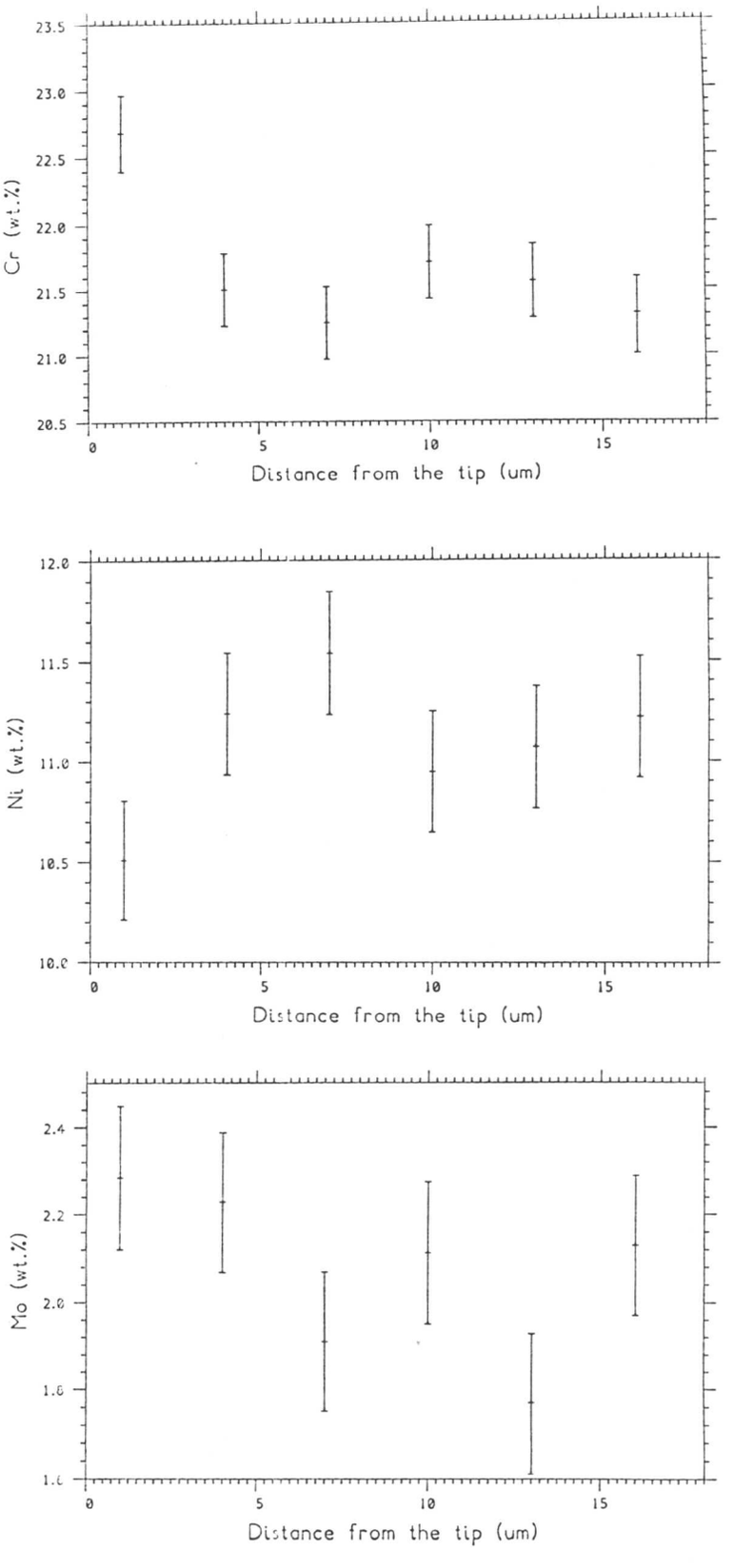

Fig. 6.65 a: EDX microanalysis survey across a Widmanstätten austenite plate in isothermally transformed sample of alloy R4P at 1000°C.

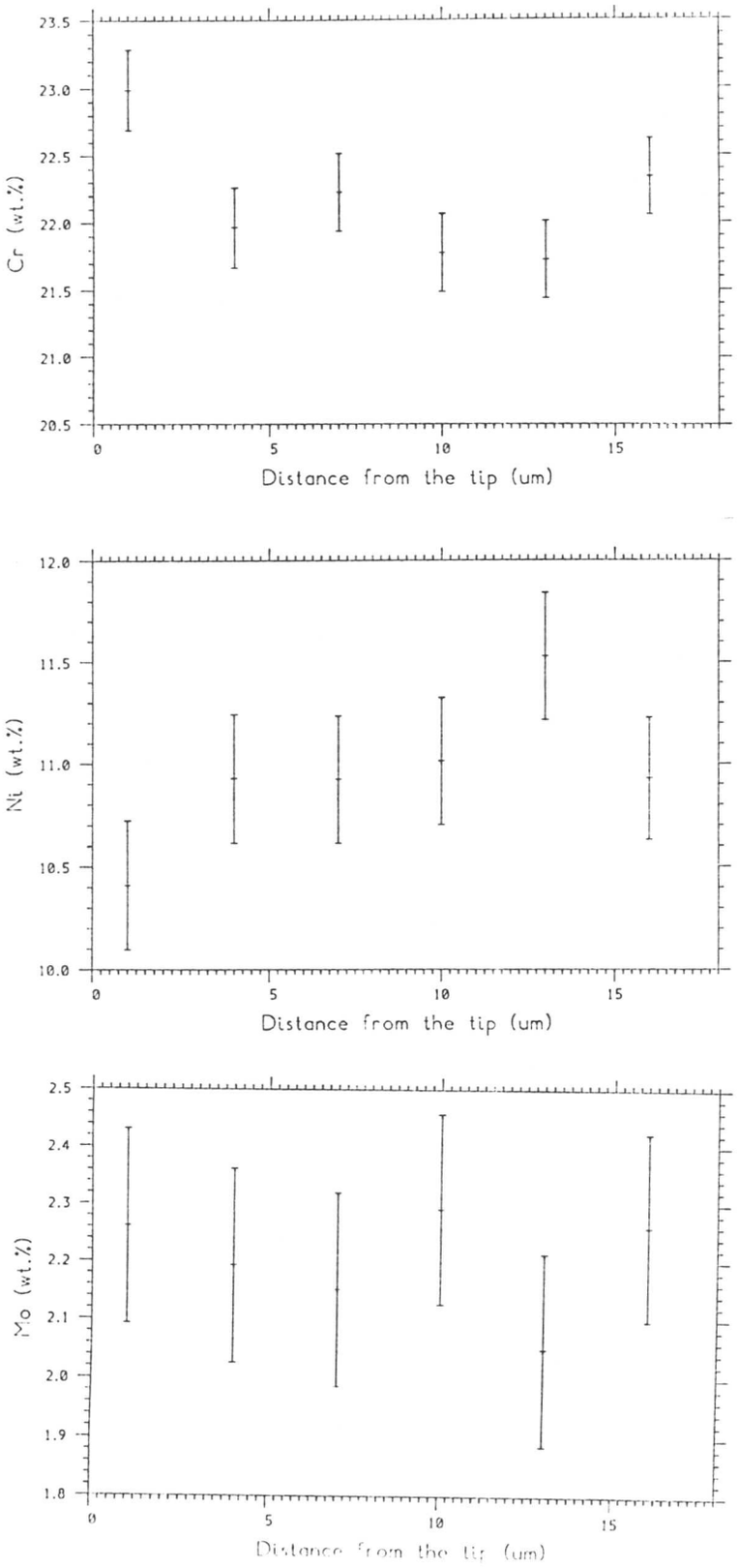

Fig. 6.65 b: EDX microanalysis survey across intragranularly nucleated austenite plate in isothermally transformed sample of alloy R4P at 1000°C.

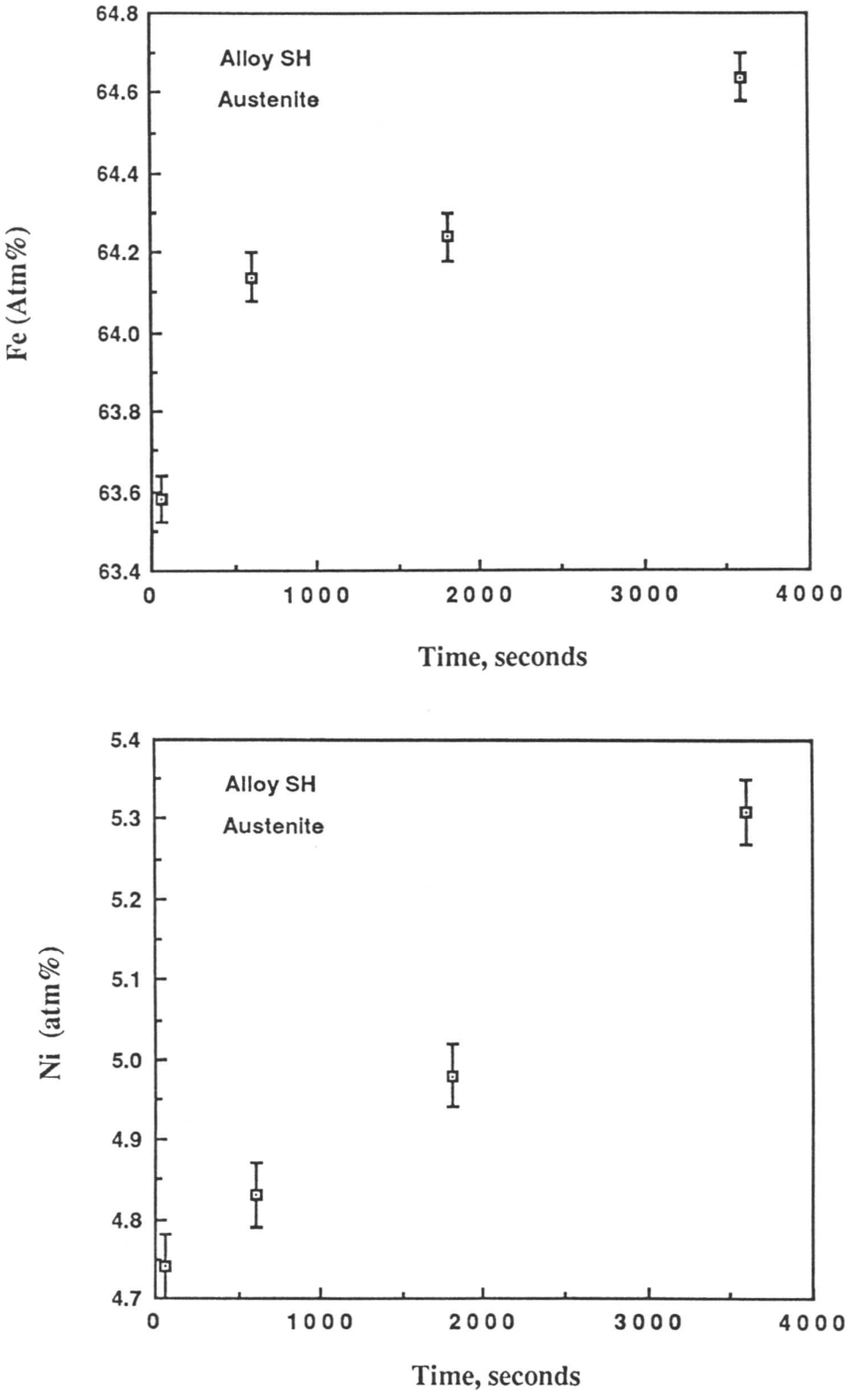

Fig. 6.66: Variation of iron and nickel concentrations with $\delta \rightarrow \gamma$ reaction time as measured using EDX on SEM in isothermally transformed SH specimens at 900°C.

6.9 Conclusions

(a) The kinetics of the $\delta \rightarrow \gamma$ solid state transformation under isothermal transformation conditions are found to be very rapid in all of the welded and wrought alloys investigated in the present work. In some cases this prevented the detection of an incubation period, and on occasions, transformation could not be prevented from happening during the quench to the isothermal transformation temperature. Higher nickel, nitrogen, carbon and oxygen concentrations in the welded alloys all yielded higher volume fractions of austenite and faster transformation kinetics after the isothermal heat treatment.

The dilatometric technique was verified to be a powerful method for detecting the $\delta \rightarrow \gamma$ transformation in duplex stainless steels enabling the course of the transformation to be charted as it happened. The dilatometric data was found to be similar to those obtained metallographically. The two techniques compliment each other, since the interpretation of dimensional changes relies on a knowledge of the phases that exist during reaction.

$\delta \rightarrow \gamma$ transformation is found to exhibit C-curve overall transformation kinetics at isothermal reaction temperatures higher than 800°C. Below that temperature, and in agreement with the investigations by Kuo [30], the reaction is believed to occur in two stages separated by a temporary lull, associated with a delayed separate C-curve for the formation of the "acicular" austenite.

An analysis of the overall transformation kinetics data using the Johnson-Mehl Avrami type equation suggest that it can not be used empirically without further data of the way in which the nucleation and growth rates vary with time and temperature. Further work is also needed to separate the kinetics of the different types of austenite that form.

(b) The decomposition of δ-ferrite is characterised by the formation of allotriomorphic austenite on the δ/δ boundaries, followed by the precipitation of Widmanstätten arrays of austenite, both from the δ-ferrite grain boundaries and from the allotriomorphic austenite/δ-ferrite interfaces. Intragranular austenite with a morphology between that of a rod and plate was also observed to form at the latter stages of reaction. Although the morphologies observed during the $\delta \rightarrow \gamma$ reaction are similar in many ways to the $\gamma \rightarrow \alpha$ transformation in low-alloy steels, unlike their counterparts in low-alloy steels, Widmanstätten and acicular austenite do not

seem to grow by a displacive transformation mechanism. Because of the higher temperatures involved there appears to be some partitioning of the substitutional solute atoms during the growth of both of these phases. Studies of the associated surface relief indicate the lack of an invariant plane strain shape deformation during growth. Another result supporting this is that the solute concentration in austenite is found to increase with increasing isothermal reaction time. Some austenite rods were observed to cross the parent phase grain boundaries without deviation, suggesting again a reconstructive mode of phase transformation.

(c) Widmanstätten austenite was generally observed to form at isothermal temperatures between 1100 and 900°C in the fine grained specimens. For coarse grained samples (600 μm) this temperature range was more limited to 1000 − 900°C. For welded alloys, the Widmanstätten austenite tended to grow as secondary plates from already existing austenite allotriomorphs. At lower temperatures the formation of acicular austenite is preferred to that of Widmanstätten austenite. A larger δ-ferrite grain size promoted the formation of the acicular austenite since more space is then available for intragranular nucleation and growth, reactions which are otherwise stifled by events originating at the δ grain boundaries.

(d) Higher concentrations of carbon, nitrogen and silicon (*e.g.* alloy W111) led to faster transformation kinetics, and thicker layers of allotriomorphic austenite. The layers were found to eventually continue transformation by co-operative growth of austenite and $M_{23}C_6$ (Cellular growth).

(e) The effect of δ-ferrite grain size on the $\delta \rightarrow \gamma$ transformation, in welded and wrought alloys of nearly the same chemical composition, revealed that the weld metal is much less sensitive to the δ-ferrite grain size. Nonmetallic inclusions in the weld provide numerous intragranular nucleation sites for the austenite thereby diminishing the role of the parent δ grain boundaries. The inclusions were also found to restrict δ-ferrite grain growth at elevated temperatures in a Zener pinning mechanism.

(f) Sigma phase formation seems rather rapid in welded alloys. The phase nucleates primarily at the δ/γ boundaries during the late stages of γ growth. More specifically, it prefers to precipitate at the allotriomorphic austenite/δ-ferrite boundaries *i.e.* presumably because of the higher degree of Cr/Mo partitioning relative to

other types of austenite. The larger equilibrium volume fractions of austenite and associated faster kinetics of $\delta \rightarrow \gamma$ transformation in the weld metals which have larger Ni_{eq}/Cr_{eq} (compared to the wrought alloys), play a role in accelerating σ formation by increasing the chromium concentration in the residual δ. There may also exist a role of the interstitials in this respect, which acquires further investigation.

(g) The ferritisation process is kinetically a rapid process at elevated temperatures. The rate increase monotonically with temperature since both the driving force and diffusion rates increase with temperature. The microstructure also coarsens rapidly once the austenite phase is completely dissolved. However, for welds metals, the grain-growth process is limited by the presence of inclusions, and the kinetics of δ formation are relatively slow due to their larger Ni_{eq}/Cr_{eq} ratio.

(h) In microstructures which are incompletely ferritised, the rate of subsequent transformation to austenite is accelerated since any residual austenite simply grows, and the need for nucleation is thereby removed. During air cooling, a partially ferritic microstructure† tends to decompose to specifically Widmanstätten austenite, presumably because the one-dimensional growth of allotriomorphic austenite is relatively slow, and because intragranular nucleation is also relatively sluggish. The presence of residual austenite is also found to stimulate σ phase formation at δ/γ boundaries.

† Appendix 3.

References

1. Ledbetter, H.M. and Austin, M.W. (1987) Mat. Sci. and Tech.,**3**, p. 101.
2. Horn, E. M. and Kugler, A. (1977) Werkst.-Techn., **8**, p. 362.
3. 1986 Solomon, D. and Devine, T. M., Conf. Proc., "Duplex Stainless Steels", St. Louis, USA (1982) Publ. by ASM (1983), p. 693.
4. Avrami, M. (1939), J. Chem. Phys., vol. **7**, p. 1103.
5. Avrami, M. (1940), J. Chem. Phys., vol. **8**, p. 212.
6. Avrami, M. (1939), J. Chem. Phys., vol. **9**, p. 177.
7. Johnson, W. A. and Mehl , R. F. (1939), Trans AIME, **135** pp. 416-442
8. Rhines, F. N. (1971) Met. Trans., **1**, p. 1105.
9. Reed-Hill R. E. (1974) 'Physical Metallurgy Principles' East-West Press, New Delhi.
10. As quoted by Smith, C. S. (1948) Trans. AIME, **175**, p. 15.
11. Mullins, W. W. (1958) Acta. Met., **6**, p. 414.
12. Alberry P. J., Chew, B. and Jones, W. K. C. (1977) Metals Tech. Vol. 1, **6**, p. 317.
13. Burke, J. E. and Turnbull, D. (1952) Prog. Metal Phys., **3**, p. 220.
14. Rosenthal, D. (1941) Weld. J., **20**, p. 220s.
15. Ashby, M. F. and Easterling, K. E. (1982) Acta Metall. **30**, p. 1969.
16. Ion, J. C., Easterling, K. E. and Ashby, M. F. (1984) Acta Metall. **32**, No. 11, p. 1949.
17. Honeycombe, J. and Gooch, T. G. (1985) The Weld. Inst. Report 286/ 1985.
18. Ikawa, H. *et al.* september (1973) Trans. Jap. Weld. Soc., Vol.4 No.2, p. 35.
19. Hochoertler, G. and Kriszt, K. 'Duplex Stainless Steel', Conf. Proc., Oct. 1986, The Hague, Publ. by Nederlands Instituut Voor Lastechniek, p. 114.
20. Averbach, B. L. and Cohen, M. February (1948), Metals Tech., TP 2342.
21. Lippold, J. C. and Savage, W. F. (1979) Weld. J., **58**, Res. Suppl., p. 362s.
22. Lippold, J. C. and Savage, W. F. (1979) Weld. J., **58**, Res. Suppl., p. 362s.
23. Leone, G. L. and Kerr, H. W. (1982) Weld. J., **61**, p. 13.

24. Cieslak, M. J., Ritter. A.M. and Savage, W. F. (1982) Weld. J., **61**, Res. Suppl., p. 1s.

25. Southwick, P. D. (1978) Ph.D. Thesis, University of Cambridge.

26. Solyu, B. (1988) Ph.D. Thesis, University of Cambridge

27. Hertzmann, S. et al. 'Duplex Stainless Steel', Conf. Proc., Oct. 1986, The Hague, Publ. by Nederlands Instituut Voor Lastechniek, p. 257.

28. Bhadeshia, H. K. D. H. (1981) Acta Metall., **29**, p. 1117.

29. Yang, J. R. and Bhadeshia, H. K. D. H. (1987) 'Advances in Welding Science and Technology', Conf. Proc. Ed. David, S. A. ASM, Ohio, p. 187.

30. Strangwood, M. and Bhadeshia, H. K. D. H. (1987) 'Advances in Welding Science and Technology', Conf. Proc. Ed. David, S. A. ASM, Ohio, p. 209.

31. Kuo, K., (1955) JISI, **181**, p. 134.